



universität
wien

DISSERTATION / DOCTORAL THESIS

Titel der Dissertation /Title of the Doctoral Thesis

Sub-10 nm aerosol nanoparticle characterization:
From mobility standards to ambient new particle formation

verfasst von / submitted by

Sophia Brilke, M.Sc.

angestrebter akademischer Grad / in partial fulfilment of the requirements for the degree of
Doktorin der Naturwissenschaften (Dr. rer. nat.)

Wien, 2020 / Vienna, 2020

Studienkennzahl lt. Studienblatt /
degree programme code as it appears on the student
record sheet:

UA 796605411

Dissertationsgebiet lt. Studienblatt /
field of study as it appears on the student record sheet:

Physik

Betreut von / Supervisor:

Assoz.-Prof. Dr. Paul Winkler

Abstract

New particle formation is ubiquitous in the global atmosphere and is identified as the major source of nucleation mode particles. Newly formed particles largely contribute to the global number concentration and may grow to larger sizes and directly and indirectly influence the global climate. The focus of this research project is on the measurement of the sub-10 nm particle size regime to study the dynamics of freshly formed particles. This includes the detailed study of heterogeneous nucleation of different aerosol types in common particle counters. The size distribution of nanoparticles in the sub-10 nm size regime is measured with a high-precision instrumentation system based on the size classification using Differential Mobility Analyzers (DMAs), the so-called DMA-train. Six DMAs are operated in parallel to monitor particles of fixed but different size channels in the sub-10 nm size range to retrieve precise size information.

Condensation Particle Counters (CPCs) are used as detectors in the DMA-train and their counting efficiency is a large source of uncertainty regarding the size distribution. The CPCs have the lower detection limit between 1 - 4 nm and aerosol standards for instrument characterization measurements are needed. In this project, a novel bipolar electrospray source was set up in combination with a high-resolution UDMA-4 to extend the range of available clusters from 2 - 3 to up to 18 depending on the substance. The analysis of the clusters using mass spectrometry showed high purity of the sample aerosol allowing to perform precise counting efficiency measurements.

The activation of hygroscopic sodium chloride (NaCl) and non-absorbent silver (Ag) particles was investigated at three different nucleation temperatures in n-butanol-based CPCs and changing relative humidity of the carrier gas. The temperature dependent measurements revealed enhanced counting efficiencies at reduced nucleation temperature settings. A pronounced humidity dependence of the activation of NaCl particles when exposed to a humid carrier gas was found. The findings suggest a careful consideration of possible effects on the CPC counting efficiency when the sample is subject to changing relative humidity of the carrier gas and aerosol composition, especially under ambient conditions.

Atmospheric size distribution measurements with the focus on the sub-10 nm size range using the DMA-train were performed for the first time within the A-LIFE field experiment in Cyprus. Several NPF events and the sub-10 nm dynamics were studied in detail. The early particle growth did not always exceed 10 nm and was therefore not detected by the conventional size distribution measurement starting at 10 nm. The results suggest that the NPF frequency may be higher than assumed when the sub-10 nm size range is not covered. The combined size distributions reveal deep insight into the sub-10 nm aerosol dynamics in the atmosphere and highlight the importance of covering the complete atmospheric size range down to 1 nm.

Zusammenfassung

Die Bildung neuer atmosphärischer Partikel ist allgegenwärtig und wird als wesentliche Quelle für Partikel aus der Nukleationsmode identifiziert. Neugebildete Partikel tragen wesentlich zur globalen Anzahlkonzentration bei und können zu größeren Durchmessern heranwachsen und das globale Klima direkt und indirekt beeinflussen. Der Schwerpunkt dieses Forschungsvorhabens liegt auf der Messung von atmosphärischen Nanopartikeln mit Durchmessern kleiner als 10 nm. Dies beinhaltet die detaillierte Untersuchung der heterogenen Nukleationsprozesse von unterschiedlichen Aerosoltypen in konventionellen Partikelzählern. Die Größenverteilung von Nanopartikeln im sub-10 nm Größenbereich wird mit einem Messsystem basierend auf der Größenklassifizierung mittels "Differential Mobility Analyzers"(DMAs), dem sogenannten "DMA-train", gemessen. Sechs DMAs werden parallel betrieben um die nach Größe aufgelöste Anzahlkonzentration in festen, aber unterschiedlichen Größenkanälen aufzunehmen. Dieser Aufbau erlaubt die präzise Messung der sub-10 nm Größenverteilung mit einer hohen Zeitauflösung von 1 s.

"Condensation Particle Counters"(CPCs) werden im DMA-train als Detektoren eingesetzt, dementsprechend stellt die CPC Detektionseffizienz eine Quelle für Unsicherheiten in der Bestimmung der Größenverteilung dar. Das untere Detektionslimit der untersuchten CPCs bewegt sich im Größenbereich von 1 – 4 nm, weshalb Aerosolstandards in diesem Größenbereich ein wichtiges Werkzeug in der Messinstrumentencharakterisierung sind. Im Rahmen dieses Dissertationsvorhabens wurde eine neue bipolare Elektrosprayquelle zur Generierung von molekularen Clustern wohl bekannter Zusammensetzung mit einem hochauflösenden DMA kombiniert, um Mobilitätsstandards zu erzeugen. Die chemische Clusteranalyse mittels Massenspektrometrie wies hohe Reinheit der generierten Cluster nach und präzise Messungen der Detektionseffizienz von CPCs wurden durchgeführt.

Die Aktivierung von hygroskopischen Natriumchlorid (NaCl) und unlöslichen Silber (Ag)-partikeln wurde bei drei unterschiedlichen Nukleationstemperaturen in butanol-basierten CPCs sowie bei veränderlicher relativer Feuchte des Trägergases untersucht. Die temperaturabhängigen Messungen zeigen eine verbesserte Detektionseffizienz bei reduzierten Nukleationstemperaturen. Es zeigte sich eine ausgeprägte Feuchteabhängigkeit der Aktivierungseffizienz von NaCl Partikeln, wenn diese einer erhöhten Luftfeuchtigkeit ausgesetzt sind. Die Ergebnisse deuten auf eine sorgfältige Berücksichtigung möglicher Effekte auf die CPC Detektionseffizienz hin, wenn die Probe einer wechselnden relativen Luftfeuchte ausgesetzt ist und aus unterschiedlichen Aerosoltypen besteht. Dies kommt bei atmosphärischen Nanopartikelmessungen zum Tragen.

Atmosphärische Größenverteilungsmessungen unter Verwendung des DMA-trains mit dem Schwerpunkt auf den Größenbereich unterhalb von 10 nm wurden erstmals im Rahmen der A-LIFE Messkampagne auf Zypern durchgeführt. Einige Fälle von Partikelneubildung sowie

Partikelwachstum wurden beobachtet und die sub-10 nm Partikeldynamik im Detail untersucht. Es zeigte sich, dass nicht in allen Fällen neugebildete Partikel über 10 nm hinauswachsen. Dieses Ergebnis weist darauf hin, dass Partikelneubildung häufiger auftreten könnte als angenommen, wenn der Größenbereich unter 10 nm nicht abgedeckt ist. Die Größenverteilungsmessungen erlauben einen tieferen Einblick in die sub-10 nm Aerosoldynamik in der Atmosphäre und unterstreichen die Bedeutung der Abdeckung des gesamten atmosphärischen Größenbereichs bis hinunter zu 1 nm.

Contents

1	Introduction	9
1.1	Experimental Methods	13
1.2	References	22
2	Precision characterization of three ultrafine condensation particle counters using singly charged salt clusters in the 1 - 4 nm size range generated by a bipolar electrospray source	27
2.1	Introduction	28
2.2	Experimental Methods	30
2.3	Results and Discussion	35
2.4	Conclusion	46
2.5	Supplemental Information	48
2.6	Author Contributions	50
2.7	References	51
3	Humidity effects on the detection of soluble and insoluble nanoparticles in butanol operated condensation particle counters	57
3.1	Introduction	58
3.2	Experimental Section	60
3.3	Results and Discussion	63
3.4	Conclusion	74
3.5	Author Contributions	76
3.6	References	77
4	New particle formation and sub-10 nm size distribution measurements during the A-LIFE field experiment in Paphos, Cyprus	83
4.1	Introduction	84
4.2	Methods	85
4.3	Results and Discussion	90
4.4	Conclusion	99
4.5	Supplemental Information	100
4.6	Author Contributions	102
4.7	References	103
5	Conclusion	109
5.1	References	112

Chapter 1

Introduction

Atmospheric aerosols are tiny liquid or solid particles suspended in the air. With every single breath we take unwarily a vast number of aerosol particles enters our lungs and respiratory system. But not only adverse health affects and premature death worldwide are related to aerosol particles in air (Donaldson et al., 2000; Lelieveld et al., 2015), also the global climate is largely affected by the atmospheric aerosol loading (Spracklen et al., 2006). Primary aerosol particles are emitted directly into the atmosphere including mineral dust, sea spray and particles from biomass burning, or they form secondarily by gas-to-particle conversion. The precursor vapors contributing to particle formation in the atmosphere arise from natural and anthropogenic emissions, such as biogenic vapors, amines, ammonia and sulfur dioxide (Kürten et al., 2016; Rose et al., 2018; Sipilä et al., 2010). Human activity profoundly influences the global climate by altering the amount of atmospheric constituents. Today, awareness on climate change has become a major topic among society. Mankind has to deal with the environmental consequences of climate change such as an increased global surface temperature caused by enhanced greenhouse gas emissions, the resulting changing global rainfall patterns and a rise of sea level. The scientific evidence of climate change, its impacts and response options are summarized in the Assessment Report by the Intergovernmental Panel on Climate Change (IPCC) and can be found in Boucher et al. (2013).

Aerosol particles play an important role in the Earth-atmosphere system by their capability to form cloud droplets. Aerosols directly influence the energy flux in the atmosphere by scattering sunlight back into space, but also absorbing solar radiation. When an air parcel rises, expands and cools, particles can become cloud condensation nuclei (CCN). Polluted clouds composed of a larger number of CCN appear brighter and scatter back more sunlight (Twomey et al., 1984) and are less subject to rain-out thus increasing the cloud's lifetime (Albrecht, 1989).

Climate predictions require precise knowledge of the factors and mechanisms leading to climate change. Despite recent research efforts, uncertainties on the radiative forcing relative to preindustrial times from aerosol particles remain large (Boucher et al., 2013). Therefore, detailed knowledge on the aerosol-related processes and aerosol-cloud interactions on a global scale is urgently needed. This information is then fed into climate models to estimate impacts on the future climate.

The atmospheric number size distribution ranges from 1 nm to 10 μm and is displayed in Figure 1.1. Distinct size modes characterize the number size distribution with particles assigned

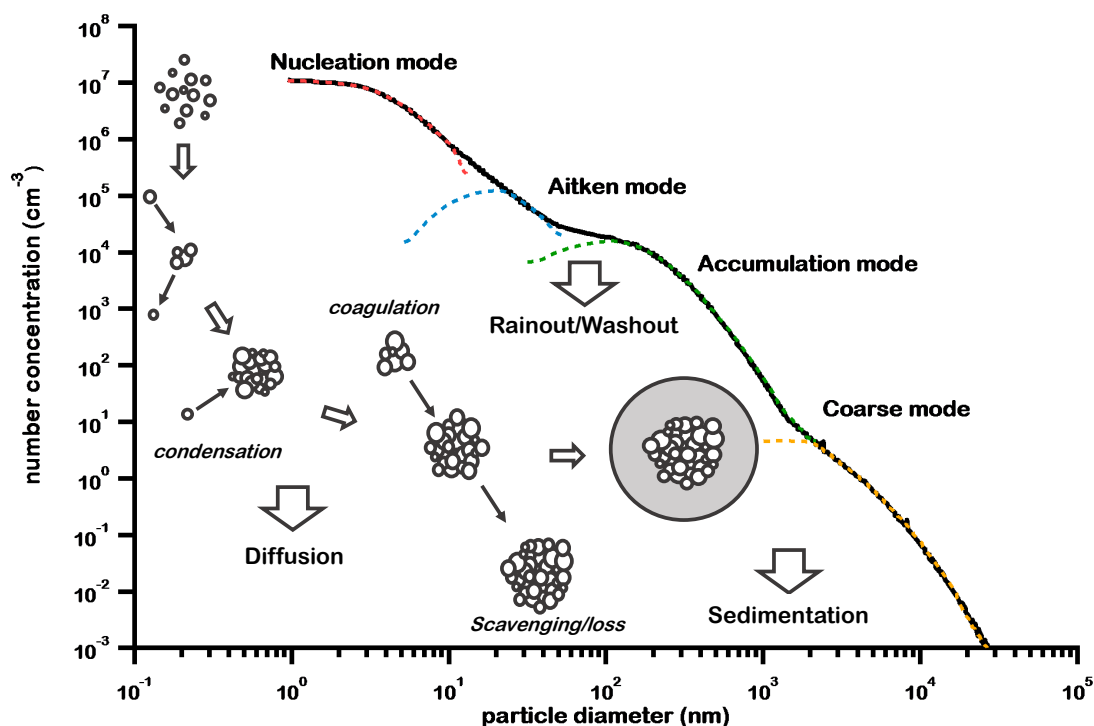


Figure 1.1. The number size distribution ranging from 1 nm to 10 μm of atmospheric aerosol particles shows the atmospheric particle modes typically observed in the atmosphere. The primary source of nucleation mode particles (red dashed line) is gas-to-particle conversion and a schematic of this process is illustrated in gray. The content of this Figure was adapted from Buseck and Adachi (2008).

to each mode having their specific sources, sinks, lifetimes, optical and chemical properties as well as transition pathways. Seinfeld and Pandis (2016) define particles with a diameter less than 20 nm as nucleation mode particles. Aitken mode particles range from 20 nm to 100 nm and accumulation mode particles from 100 nm - 2.5 μm followed by coarse mode particles with diameters larger than 2.5 μm (Seinfeld and Pandis, 2016). Nucleation mode particles, which constitute the main research focus of this work, form by gas-to-particle conversion. This phenomenon is called new particle formation (NPF) and is ubiquitous in the global atmosphere (Kulmala et al., 2004). Precursor gases oxidize to low-volatility compounds which, by statistical chance, build up molecular clusters at high enough vapor abundances (schematically shown in Figure 1.1). This process is called homogeneous nucleation since no surface or nucleus is present that the vapors can condense onto. The greater the supersaturation of the vapor, the larger the probability that single molecules form clusters. Once a cluster exceeds a critical cluster size, even momentarily, it overcomes the nucleation barrier, thus becomes stable and continues to grow by further condensation (Hinds, 1999). The critical cluster size is reached when the rate of molecules evaporating off from the cluster's surface equals the

rate of molecules condensing onto it. The theory of the underlying thermodynamic processes are summarized in the “Classical Nucleation Theory” (CNT) of which an overview is given, for example, in Curtius (2006) and Wyslouzil and Wölk (2016). The height of the nucleation barrier is lowered when a surface is present. This process is then termed heterogeneous nucleation which comes into place in the atmospheric context of cloud droplet activation. Water vapor itself would never undergo homogeneous nucleation in the atmosphere because an extraordinarily high vapor supersaturation would be needed that will practically never occur in our atmosphere (Curtius, 2006). Consequently, without aerosols there would be no clouds.

Aerosol particles in the size range below 50 nm are typically referred to as nanoparticles and constitute the largest fraction of ambient aerosol in terms of number (Buseck and Adachi, 2008) (see Figure 1.1). Their measurement is not straightforward since their size is smaller than the wavelength of visible light. Therefore, nanoparticles need to grow to larger sizes before they can be optically detected. Condensation Particle Counters (CPCs) are common instruments for measuring the aerosol number concentration. Nanoparticles are activated by heterogeneous nucleation of a suitable supersaturated vapor and thus grow to optically detectable sizes. The measured nanoparticle number concentration then allows to infer parameters describing the dynamics of a nanoparticle population during an NPF event. The formation rate describes at what rate particles have overcome the nucleation barrier whereas the particle growth rate characterizes how fast particles grow in diameter. As previously discussed, the particle diameter at the nucleation barrier is defined as the critical diameter. When the instrument detection limit is higher than the estimated critical cluster size, the measured formation rate needs to be corrected for the rate at which particles have grown further (Lehtinen et al., 2007). Therefore, the detailed determination of the growth of freshly nucleated particles is critical to study the process of NPF. Typical formation rates of 3 nm particles range from $0.01 \text{ cm}^{-3} \text{ s}^{-1}$ to $10 \text{ cm}^{-3} \text{ s}^{-1}$ in the boundary layer and growth rates of 1 nm h^{-1} to 20 nm h^{-1} have typically been observed in different environments (Kulmala et al., 2004).

Studying atmospheric aerosols in the low nanometer size regime is challenging and requires state-of-the-art instrumentation. The experimental methods to measure the size-resolved number concentration of particles and conduct studies on heterogeneous nucleation in the laboratory and in ambient environments are presented in Section 1.1 of this Chapter.

In Chapter 2, a new method for precision characterization of CPCs is presented. A bipolar electrospray source is set up in a laboratory experiment to produce singly charged salt clusters composed of single molecules and precisely known composition. The first mass spectrometric measurements on the clusters generated by the bipolar electrospray source are presented here. High-resolution mobility classification enables the generation of mobility standards in the approximated size range of 1 nm to 4 nm, which represents the overlapping region between the

larger end of the mass range covered by the Atmospheric pressure interface Time-Of-Flight (APi-TOF) mass spectrometer and the CPCs lower detection limit. This experiment allows to study the activation behavior of the salt clusters exposed to different types of supersaturated vapors and may serve as a calibration standard in future CPC calibration studies.

A second laboratory experiment with the focus on the activation behavior of soluble and insoluble particle seed types in a humid carrier gas at different nucleation temperatures is presented in Chapter 3. This experiment focuses on the effects of relative humidity (RH) and nucleation temperature on the CPCs lower detection limit and discusses the underlying activation process. The findings of this study are of practical interest for ambient measurements where all kind of seed types are present and the air is subject to changing RH.

Finally, an atmospheric experiment is presented in Chapter 4. During the A-LIFE (**A**bsorbing aerosol layers in a changing climate: aging, **l**ifetime and dynamics) field experiment in Cyprus, a DMA-train is set up for the first time in an atmospheric environment and measures the sub-10 nm size distribution to study the nanoparticle dynamics during NPF events. The possible effect of changing RH and reduced nucleation temperature on the CPC detection efficiency were considered in this study. With the A-LIFE nanoparticle size distribution measurements, another piece of the puzzle is added to the large set of observation points worldwide studying the global phenomenon of NPF in the atmosphere.

1.1 Experimental Methods

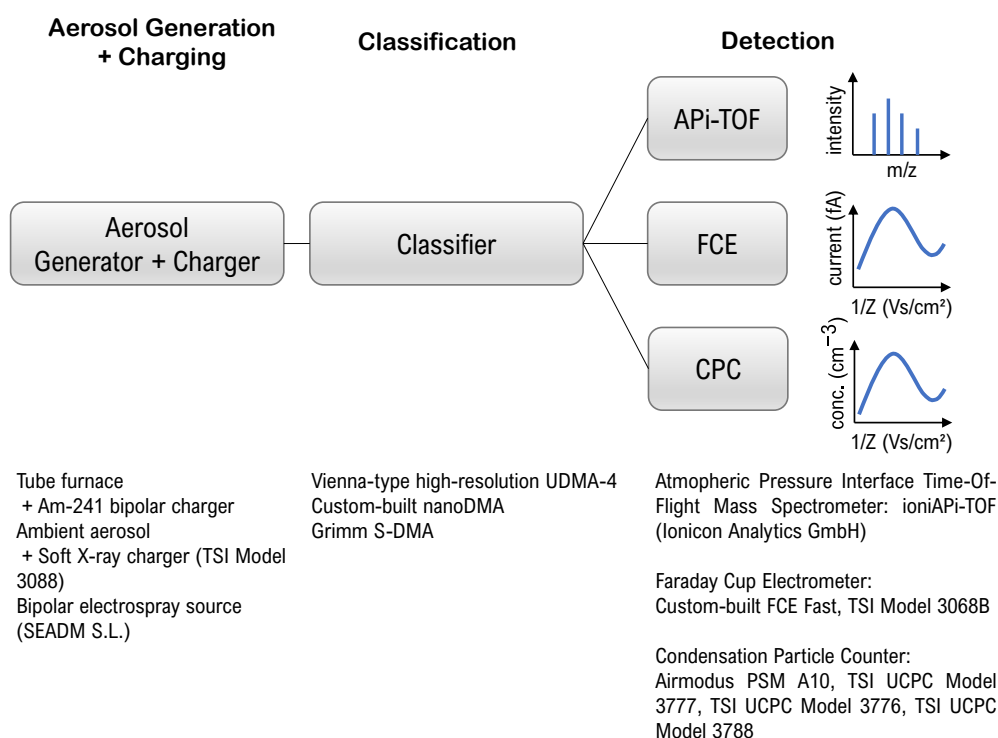


Figure 1.2. Overview of the measurement methods used in this work. The basic method is electrical mobility spectrometry and consists of the three major steps: aerosol generation and charging, size classification and detection. The instrumentation specifically used in this work is listed here.

On the following pages, an overview of the methods and instrumentation used during this research project is given. The principal measurement method is electrical mobility spectrometry which is based on the classification of charged particles or clusters according to their electrical mobility. Figure 1.2 illustrates the needed steps to take to obtain a size-resolved nanoparticle measurement. Electrical mobility spectrometry requires i. aerosol generation and charging, ii. classification and iii. detection of particles or clusters. Particles are classified in a Differential Mobility Analyzer (DMA). The mobility or mobility equivalent size classified particles are then analyzed. The Atmospheric Pressure interface Time-Of-Flight mass spectrometer (APi-TOF) measures the ion intensity vs. the mass-to-charge ratio of the sample. The particle number concentration is determined by a Condensation Particle Counter (CPC) or Faraday Cup Electrometer (FCE). The single components are discussed in this section with respect to their use in the experiments presented in Chapters 2, 3 and 4.

1.1.1 Aerosol Generation and Charging

Tube furnace. A common method to produce test aerosols is the condensation type aerosol generator which is described in Scheibel and Porstendörfer (1983). A test material, e.g. silver or sodium chloride in the solid phase, is inserted into a tube furnace. The material is heated, it evaporates and the vapor is transported into a cooler zone where supersaturation leads to homogeneous nucleation and the formation of nanoparticles. The mode of the resulting size distribution can be shifted by adjusting the temperature and the flows through the tube furnace. This method has been used in this work to produce soluble and insoluble nanoparticles of silver and sodium chloride to investigate the effect of nanoparticle activation when the test aerosol is exposed to a humid carrier gas (Tauber et al., 2019), see Chapter 3. The resulting polydisperse nanoparticle population does not carry charge and subsequent charging by an ionization source, such as a soft X-ray or radioactive charger is required for the classification by electrical mobility spectrometry.

Electrospray. The second method used extensively in this work was the generation of nanoparticles by the electrospray technique with the aim of having a variety of molecular clusters available for the investigation of their chemical composition and activation efficiency in the cluster-particle transition size regime. The electrospray technique is widely used in the field of Analytical Chemistry and was first introduced by Fenn et al. (1989). An overview of the background of the method and different measurement techniques including coupling an electrospray to a mass spectrometer can be found in Banerjee and Mazumdar (2012). An analyte sample is dissolved in a polar liquid such as water, methanol or acetonitrile. The solution is set to a high voltage potential and is pushed through a capillary. At the capillary's sharpened tip, a meniscus, also called Taylor cone, forms under the competing forces of the electric field and the surface tension of the liquid. A fine jet of charged droplets is emitted from the Taylor cone's tip towards a counter electrode. The solvent evaporates from the droplets surface which leads to an increased surface concentration of the charge. The droplets eventually reach the Rayleigh limit and explode repeatedly thus producing gas-phase ions. When the electrospray is operated at one polarity, it is referred to as unipolar mode electrospray which produces unipolar ions. The resulting ion population can be classified by electrical mobility analysis and clusters of different electrical mobility can be separated from each other. However, complex mixtures of clusters at charge states larger than 1 occur to a large extent at an inverse mobility larger than 2 V s cm^{-2} corresponding to approx. 1.7 nm mobility equivalent diameter. As a result, the clusters are not separable anymore by electrical mobility spectrometry. This limitation to small clusters can be overcome by exposing the cloud of unipolar ions to their counter ions. There have been different approaches to create counter-ions for the reduction of higher charger states. Favorably, the counter-ions have the same chemical composition, therefore Fernández de la Mora and Barrios-Collado (2017)

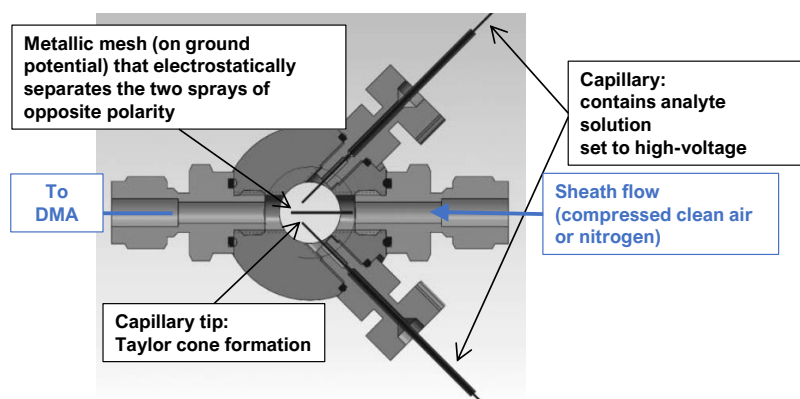


Figure 1.3. Schematic illustration of the bipolar electro spray chamber combining two capillaries set to opposite high voltage. The technical drawing was taken from Fernández de la Mora and Barrios-Collado (2017).

presented the idea of combining two electro sprays of opposite polarity. During this research project, the bipolar electro spray commercially available from SEADM S.L., Spain, was used. A schematic of the bipolar electro spray chamber is displayed in Figure 1.3. Two capillaries contain the same solution at opposite polarity which is pushed to the capillary tip by applying a gentle pressure (1 mbar to 20 mbar). A metallic mesh electrostatically separates the two capillary tips, where the Taylor cones form, in a reaction chamber. The cloud of bipolar ions is carried by a surrounding sheath gas and is transported to a DMA. As a result of recombination of ions with their counter ions, dominantly singly charged ions are formed. During this work, the bipolar electro spray source proved to be a powerful tool to create molecular clusters at charge state 1 that can be used for studying heterogeneous nucleation and performing instrument optimization. The experiments using this source and the results are presented in Chapter 2.

The smooth and stable operation of the electro spray source very much depends on different factors. Cleanliness of the sample, dry sheath gas conditions, stable applied pressure and not least the user's experience are to mention here. A detailed description on how to implement and operate the bipolar electro spray source at stable conditions can be found in the Master's thesis of Julian Resch (in preparation).

Particle charging. Depending on the generation method, particles need to be ionized prior to classification in a DMA. In the atmosphere, aerosol particles are dominantly neutral and particle charging is required for size-resolved ambient measurements. In this work, a radioac-

tive charger was used for charging sodium chloride and silver particles produced from a tube furnace, see Chapter 3, and a soft X-ray charger was implemented for charging atmospheric aerosol particles, as described in Chapter 4.

The charging mechanism of diffusional charging is simplified described by the attachment of ions to a particle (Hinds, 1999). An ionization source, e.g. radioactive or X-ray source, produces ionizing radiation. Air molecules are ionized, and these "charger ions" mix with the aerosol particles. By collisions due to Brownian motion, charge is transferred to the particles. When a particle and an air ion collide, the ion will stick to the particle. By accumulation of charges an electrostatic field will build up around the particle and repel incoming ions of the same polarity. This process continues until an equilibrium state, the Boltzmann equilibrium, is reached (Hinds, 1999). Whatever the initial charge distribution on the particles was, after a certain time a stationary state is established with a number of charges, n , attached to the particle (Fuchs, 1963). The charging probability of particles exposed to a bipolar ionic atmosphere is described by the Fuchs model (Fuchs, 1963) and requires detailed numerical computations. An approximation of the charging probability is provided in Wiedensohler (1988) which allows rapid calculation of the bipolar charge distribution for aerosols in the submicron size regime and was used during this work to estimate the charging efficiency. The charging probability from Wiedensohler (1988) shows that in the size regime below 10 nm, which makes up the largest part of this work, the charging state of an aerosol particle subsequent to bipolar charging is expected to be 1. The exact knowledge of the number of elementary charges attached to a particle is critical when particles are size-selected in a classifier.

1.1.2 Classification

Differential Mobility Analysis. Aerosol particle size classification is based on separating a polydisperse aerosol population into size classes. The classification is accomplished by introducing forces that balance or counteract the forces that are inherent to the particle (Flagan, 2008). These forces are inertia, aerodynamic drag force (Stokes drag law) and the force exerted on a charged particle when placed in an electrostatic field.

Charged particles are classified in a DMA, which are designed as capacitors. The measurement relies on the velocity of charged particles in a well-defined electric field and the determination of their electrical mobility, which expresses the particle's ability to move in an electric field. The electrical mobility is given by the ratio between the velocity the particle will reach in the electric field, v_E , and the electric field strength, E (Seinfeld and Pandis, 2016):

$$Z = \frac{v_E}{E} \tag{1.1}$$

By the balance of forces acting on the particle, the electrical mobility is also expressed as (Seinfeld and Pandis, 2016):

$$Z = \frac{n \cdot e \cdot E \cdot C_c(D_p)}{3 \cdot \pi \cdot \eta \cdot D_p} \quad (1.2)$$

From the conventional mobility-diameter relationship in Equation 1.2, it becomes evident that the number of elementary charges, $n \cdot e$, must be known to correctly infer the particle's electrical mobility. The Cunningham slip correction factor, $C_c(D_p)$, is dependent on the particle diameter, D_p , and needs to be considered for particles less than 0.1 μm in diameter (Hinds, 1999). The viscosity of the carrier gas, commonly air, is given by η . In principle, when the particle diameter is calculated from the mobility-diameter relationship, it is referred to as mobility-equivalent diameter or simply mobility diameter. Practically, the electrical mobility, Z , must be iteratively calculated from a given particle diameter, D_p , since the Cunningham slip correction is diameter dependent. However, in the low nanometer size range ($0.5 \text{ nm} < D_p < 5 \text{ nm}$), the mobility-diameter relationship can be approximated assuming one elementary charge per particle according to Mäkelä et al. (1996):

$$Z = 2.2458 \cdot 10^{-22} \cdot D_p^{-1.9956} \quad (1.3)$$

Note that the diameter, D_p , is in units of [m] and the mobility, Z , in [$\text{m}^2 \text{V}^{-1} \text{s}^{-1}$]. In this work, the mobility-diameter relationship in Equation 1.3 was used to infer the mobility diameter from the set DMA voltage.

In DMAs, an electric field is established between two electrodes which are set to a defined voltage potential. Charged aerosol particles are injected and are carried by a particle-free clean sheath gas parallel to the electrodes. Following a defined trajectory according to the particle's electrical mobility, a fraction of particles can exit the DMA through a slit at the opposite electrode. The geometry of the DMA and the flow rate of the sheath flow gas, Q_{sh} , in [$\text{m}^3 \text{s}^{-1}$] determine the relation between the electrical mobility and the applied voltage, U , to the electrode in units of [V]. In case of a cylindrical DMA, which was used during this work, the particle's electrical mobility relates to the DMA's geometric parameters and applied voltage as (Flagan, 2008):

$$Z = \frac{Q_{sh}}{2 \cdot \pi \cdot L \cdot U} \cdot \ln \frac{R_2}{R_1} \quad (1.4)$$

During large parts of this work the UDMA-4 was implemented, which is based on the previous UDMA-1 Vienna-type cylindrical design (Steiner et al., 2010). A technical drawing of the UDMA-4 is shown in Figure 1.4. The geometric parameters of the UDMA-4 are $R_1 = 0.0174 \text{ m}$ (inner radius), $R_2 = 0.024 \text{ m}$ (outer radius) and $L = 0.0065 \text{ m}$ (classification length). Major improvements in the UDMA-4 design include increased laminarization of the sheath flow by

three laminarization nets and an optimized pressure drop at the instrument outlet. Besides the cylindrical DMA design, other designs having their distinct features also exist and include planar and radial DMAs. Planar DMAs feature high resolution classification with a resolution power reaching 100 (Amo-González and Pérez, 2018). Radial DMA designs, such as the ROMIAC design (Mui et al., 2017), are suited for the measurement in the low nanometer size regime at minimized diffusional losses. A detailed overview of electrical aerosol measurements in the last century is given by Flagan (1998).

The DMA transfer function describes the relation between aerosol entering and exiting the DMA depending on the particle's electrical mobility, DMA geometry, flow settings and applied voltage. Consequently, the DMA transmission and DMA resolution are important parameters describing the instrument performance. Diffusion effects largely influence the DMA transfer function especially in the low nanometer size range and a detailed theoretical background on the DMA transfer function is given in Stolzenburg and McMurry (2008).

The choice of the classifier, the DMA, is critical when it comes to resolving single molecular clusters which is required for the generation of monodisperse nanoparticles. Brownian motion, which results in spreading of monodisperse particles around their trajectory, leads to substantial broadening of the transfer function. The broader the transfer function of a DMA, the less monodisperse the calibration standard, and consequently, the less useful a mobility standard becomes. In the past, this limitation has been overcome by introducing high-resolution DMAs capable of resolving single molecular ions. A high-resolution DMA has optimized geometries to reduce diffusional losses and operates at high sheath flow rates to further reduce the diffusional broadening of the transfer function. As can be seen from Equation 1.4, the mobility-voltage relation of a DMA is determined by knowing, as precisely as possible, the geometric dimensions and sheath flow rate of a DMA. However, when operating a high-resolution DMA at extraordinarily high sheath flow rates of about 1000 L min^{-1} , as is accomplished in state-of-the-art high-resolution DMAs, the flow is not measurable by conventional methods. A mobility standard then becomes a useful tool to infer the real sheath flow rate at known DMA geometry, set DMA voltage and particle electrical mobility.

Molecular mobility and mass standards. The generation of molecular mobility standards, which are characterized by being highly monodisperse and having a well-known composition, requires the production of cluster ions and their classification by electrical mobility spectrometry. Molecular mobility standards are well-suited for the calibration of aerosol instrumentation in the low nanometer size range and have been used to optimize DMA performance (Cai et al., 2018; Rosell-Llompart et al., 1996). Experiments on fragmentation inside an APi-TOF have previously been conducted using sulfuric acid clusters of known mobility and chemical composition (Passananti et al., 2019) and optimization of the ion transfer properties of the ioniAPiTOF using organic salt clusters was conducted (Leiminger et al., 2019). Furthermore, the availability of mobility and mass standards at nanometer dimension facil-

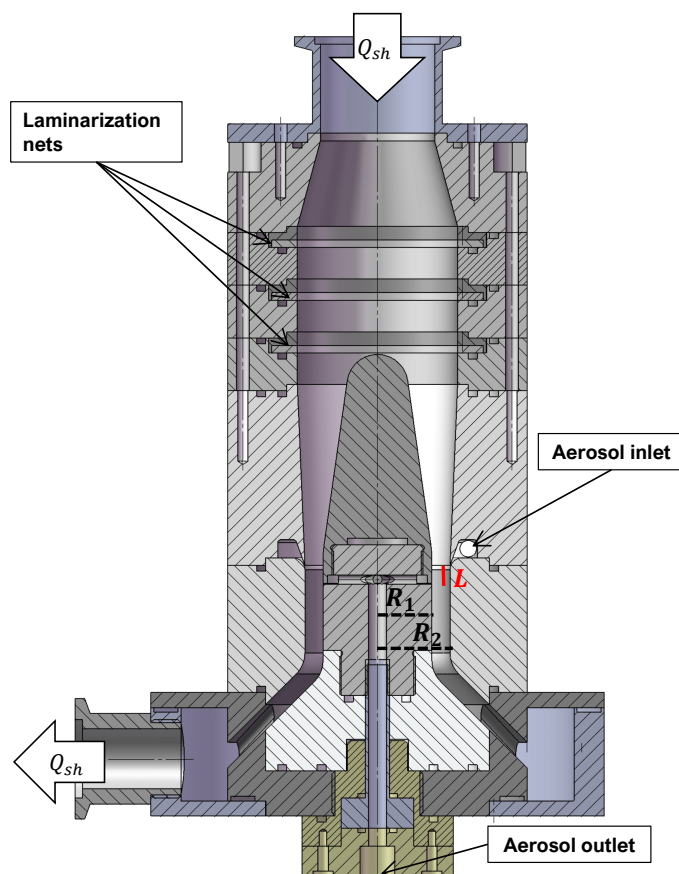


Figure 1.4. Technical drawing of the high-resolution UDMA-4. The geometric parameters of the UDMA-4 are $R_1 = 0.0174$ m (inner radius), $R_2 = 0.024$ m (outer radius) and $L = 0.0065$ m (classification length). Figure courtesy of Dr. Gerhard Steiner.

itates to getting information on the transfer function of a DMA, the performance of a CPC and the mass calibration of a mass spectrometer. When the composition (exact mass) and charge state of the calibration standard are precisely known, the clusters may well serve as mass standards. In Chapter 2, the bipolar electrospray source and a high-resolution DMA are used to generate mobility standards. Besides the advantages of mobility standards for instrument optimization, also the heterogeneous nucleation of a well-known cluster may be studied (see Chapter 2).

1.1.3 Detection

Condensation Particle Counter. The origin of CPC development dates back to John Aitken's pocket dust counter in 1892 (Aitken, 1892). Since then, large research efforts have made instrumentation available suited to detect particles as small as 1 nm. Nanometer sized

particles are grown by condensation of a supersaturated vapor until they are large enough to be optically detected by a laser and a photodiode. Different working fluids are used in CPCs to produce the supersaturated vapor. Common working fluids are n-butanol, diethylene glycol (DEG) and water. Depending on the working fluid and targeted vapor supersaturation, different instrument geometries, temperature zones and flow settings are realized in individual instrument designs. A widely used CPC type is the TSI UCPC Model 3776 (TSI 3776), where a particle-free sheath flow carrying n-butanol vapor is joined with the aerosol sample. The aerosol sample is guided into a cooler zone through a capillary and joins the supersaturated vapor in a laminar flow pattern. The CPC models used in this work including the turbulent-mixing type PSM and the laminar flow DEG-based TSI UCPC Model 3777 (“nanoEnhancer”) are listed in Figure 1.2. In Chapters 2 and 3, experiments have been performed to study the activation behavior of nanoparticles in different CPC models with regard to seed material, charge state, RH and instrument temperature and flow settings. Additional results regarding the RH-dependent counting efficiency of the PSM, the TSI nanoEnhancer and the TSI 3776 at modified temperature and flow settings can be found in the Master’s thesis of Peter Wlasits (Wlasits, 2019).

The counting efficiency, η , of a CPC is commonly inferred from the ratio of the number concentration of a monodisperse particle population measured by the CPC, N_{CPC} , to the number concentration measured by an FCE, N_{FCE} :

$$\eta = \frac{N_{CPC}}{N_{FCE}} \quad (1.5)$$

Faraday Cup Electrometer. The FCE measures the total net charge on particles by collecting them on an electrically isolated filter. The electric current, I in [A], draining from the filter can then be converted into particle number concentration, N_{FCE} in units of [cm^{-3}], at known number of elementary charges, n , attached to the particle and flow rate, Q in [$\text{m}^3 \text{s}^{-1}$]:

$$N_{FCE} = \frac{I}{n \cdot e \cdot Q} \quad (1.6)$$

Since the detection of particles by the measurement of the total net charge is a size-independent measurement, the FCE is commonly used as a reference to infer the counting efficiency of a CPC (see Equation 1.5). From Equation 1.6, it is evident that the analyzed particles must carry single charges to correctly determine the CPC counting efficiency. This property was exploited in Chapter 2 where the dominant presence of singly charged salt clusters generated by the bipolar electrospray source was confirmed by the comparison between the FCE and CPC number concentration.

As part of this study, a custom-built fast-response FCE based on the design of Winklmayr et al. (1991) is used to record mobility spectra of size-classified molecular clusters generated

by the bipolar electrospray source (see Chapter 2). The custom-built fast-response FCE and the commercially available TSI FCE (TSI Model 3068B) were implemented in the experimental setup to investigate the counting efficiency of different CPCs and thus study the activation behavior of different particle types (see Chapters 2 and 3).

Atmospheric Pressure interface Time-Of-Flight Mass Spectrometer. The chemical composition of cluster ions of atmospheric or lab-generated origin is commonly studied using the APi-TOF (Junninen et al., 2010). The atmospheric pressure interface (APi) at the instrument's inlet allows to gently guide ions to the TOF region such that the fragmentation of less stable ions at the transition to the high-vacuum region is reduced. The APi-TOF used during this work is the newly developed ioniAPi-TOF by Ionicon Analytik GmbH, Austria. The ioniAPi-TOF can be operated in positive and negative ion mode simultaneously and practically can be handled as two stand-alone instruments, with one for every polarity. The alternative approach of the ioniAPi-TOF is that the APi uses two hexapoles as ion guides which allow to transmit a broad mass range enabling the study of small precursor ions and heavy cluster ions at the same time (Leiminger et al., 2019). The mass resolution of the ioniAPi-TOF is about 2000 at a nominal mass of 410 Th and a detailed description of the instrument and its features can be found in Leiminger et al. (2019). In this work, the ioniAPi-TOF was a critical component of the experiment presented in Chapter 2. Organic salt clusters generated from the bipolar electrospray source were chemically analyzed to demonstrate their usability as mobility or mass standards having pure composition as well as charge state 1. The ioniAPi-TOF measurement yields the mass-to-charge ratio of the sample (see Figure 1.2), therefore information on the elemental composition and charge state can be inferred from the measured mass-to-charge ratio and isotopic pattern of the sample.

1.2 References

- J. Aitken. On a Simple Pocket Dust-Counter. *Proceedings of the Royal Society of Edinburgh*, 18:39–52, sep 1892. ISSN 0370-1646. doi:10.1017/S0370164600007240.
- B. A. Albrecht. Aerosols, Cloud Microphysics, and Fractional Cloudiness. *Science*, 245:1227–1230, 1989. doi:10.1126/science.245.4923.1227.
- M. Amo-González and S. Pérez. Planar Differential Mobility Analyzer with a Resolving Power of 110. *Analytical Chemistry*, 90(11):6735–6741, 2018. ISSN 15206882. doi:10.1021/acs.analchem.8b00579.
- S. Banerjee and S. Mazumdar. Electrospray Ionization Mass Spectrometry: A Technique to Access the Information beyond the Molecular Weight of the Analyte. *International Journal of Analytical Chemistry*, pages 1–40, 2012. ISSN 1687-8760. doi:10.1155/2012/282574.
- O. Boucher, D. Randall, P. Artaxo, C. Bretherton, G. Feingold, P. Forster, V.-M. Kerminen, Y. Kondo, H. Liao, U. Lohmann, P. Rasch, S. Satheesh, S. Sherwood, B. Stevens, and X. Zhang. IPCC, 2013: Clouds and Aerosols. In *Climate Change 2013: The Physical Science Basis. Contribution of Working Group I to the Fifth Assessment Report of the Intergovernmental Panel on Climate Change*, pages 571–658. Cambridge University Press, Cambridge, United Kingdom and New York, NY, USA, 2013. ISBN 9781107415324. doi:10.1017/CBO9781107415324.016.
- P. R. Buseck and K. Adachi. Nanoparticles in the atmosphere. *Elements*, 4(6):389–394, 2008. ISSN 18115209. doi:10.2113/gselements.4.6.389.
- R. Cai, M. Attoui, J. Jiang, F. Korhonen, J. Hao, T. Petäjä, and J. Kangasluoma. Characterization of a high-resolution supercritical differential mobility analyzer at reduced flow rates. *Aerosol Science and Technology*, 52(11):1332–1343, 2018. ISSN 15217388. doi:10.1080/02786826.2018.1520964.
- J. Curtius. Nucleation of atmospheric aerosol particles. *Comptes Rendus Physique*, 7(9-10):1027–1045, 2006. ISSN 16310705. doi:10.1016/j.crhy.2006.10.018.
- K. Donaldson, V. Stone, P. S. Gilmour, D. M. Brown, and W. Macnee. Ultrafine particles: Mechanisms of lung injury. *Philosophical Transactions of the Royal Society A: Mathematical, Physical and Engineering Sciences*, 358(1775):2741–2749, 2000. ISSN 1364503X. doi:10.1098/rsta.2000.0681.
- J. B. Fenn, M. Mann, C. K. A. I. Meng, S. F. Wong, and C. M. Whitehouse. Electrospray ionization for mass spectrometry of large biomolecules. *Science*, 246:64–71, 1989. doi:10.1126/science.2675315.

-
- J. Fernández de la Mora and C. Barrios-Collado. A bipolar electrospray source of singly charged salt clusters of precisely controlled composition. *Aerosol Science and Technology*, 51(6):778–786, 2017. ISSN 0278-6826. doi:10.1080/02786826.2017.1302070.
- R. C. Flagan. History of Electrical Aerosol Measurements. *Aerosol Science and Technology*, 28(4):301–380, 1998. ISSN 15217388. doi:10.1080/02786829808965530.
- R. C. Flagan. Differential mobility analysis of aerosols: A tutorial. *KONA Powder and Particle Journal*, 26:254–268, 2008. ISSN 21875537. doi:10.14356/kona.2008023.
- W. C. Hinds. *Aerosol Technology*. Johny Wiley & Sons, Incorporated, 1999.
- H. Junninen, M. Ehn, Petäjä, L. Luosujärvi, T. Kotiaho, R. Kostianen, U. Rohner, M. Gonin, K. Fuhrer, M. Kulmala, and D. R. Worsnop. A high-resolution mass spectrometer to measure atmospheric ion composition. *Atmospheric Measurement Techniques*, 3(4):1039–1053, 2010. ISSN 18671381. doi:10.5194/amt-3-1039-2010.
- M. Kulmala, H. Vehkamäki, T. Petäjä, M. Dal Maso, A. Lauri, V. M. Kerminen, W. Birmili, and P. H. McMurry. Formation and growth rates of ultrafine atmospheric particles: A review of observations. *Journal of Aerosol Science*, 35(2):143–176, 2004. ISSN 00218502. doi:10.1016/j.jaerosci.2003.10.003.
- A. Kürten, A. Bergen, M. Heinritzi, M. Leiminger, V. Lorenz, F. Piel, M. Simon, R. Sitals, A. C. Wagner, and J. Curtius. Observation of new particle formation and measurement of sulfuric acid, ammonia, amines and highly oxidized organic molecules at a rural site in central Germany. *Atmos. Chem. Phys*, 16:12793–12813, 2016. doi:10.5194/acp-16-12793-2016.
- K. E. Lehtinen, M. Dal Maso, M. Kulmala, and V. M. Kerminen. Estimating nucleation rates from apparent particle formation rates and vice versa: Revised formulation of the Kerminen-Kulmala equation. *Journal of Aerosol Science*, 38(9):988–994, 2007. ISSN 00218502. doi:10.1016/j.jaerosci.2007.06.009.
- M. Leiminger, S. Feil, P. Mutschlechner, A. Ylisirniö, D. Gunch, L. Fischer, A. Jordan, S. Schobesberger, A. Hansel, and G. Steiner. Characterisation of the transfer of cluster ions through an Atmospheric Pressure interface Time-of-Flight mass spectrometer with hexapole ion guides. *Atmospheric Measurement Techniques*, 12:5231–5246, 2019. ISSN 1867-8610. doi:10.5194/amt-12-5231-2019.
- J. Lelieveld, J. S. Evans, M. Fnais, D. Giannadaki, and A. Pozzer. The contribution of outdoor air pollution sources to premature mortality on a global scale. *Nature*, 525(7569):367–371, 2015. ISSN 14764687. doi:10.1038/nature15371.

- J. M. Mäkelä, M. Riihelä, A. Ukkonen, V. Jokinen, and J. Keskinen. Comparison of mobility equivalent diameter with Kelvin-Thomson diameter using ion mobility data. *Journal of Chemical Physics*, 105:1562–1571, 1996. ISSN 00219606. doi:10.1063/1.472017.
- W. Mui, H. Mai, A. J. Downard, J. H. Seinfeld, and R. C. Flagan. Design, simulation, and characterization of a radial opposed migration ion and aerosol classifier (ROMIAC). *Aerosol Science and Technology*, 51(7):801–823, 2017. ISSN 15217388. doi:10.1080/02786826.2017.1315046.
- M. Passananti, E. Zapadinsky, T. Zanca, J. Kangasluoma, N. Myllys, M. P. Rissanen, T. Kurtén, M. Ehn, M. Attoui, and H. Vehkamäki. How well can we predict cluster fragmentation inside a mass spectrometer? *Chemical Communications*, 55(42):5946–5949, 2019. ISSN 1364548X. doi:10.1039/c9cc02896j.
- C. Rose, Q. Zha, L. Dada, C. Yan, K. Lehtipalo, H. Junninen, S. B. Mazon, T. Jokinen, N. Sarnela, M. Sipilä, T. Petäjä, V. M. Kerminen, F. Bianchi, and M. Kulmala. Observations of biogenic ion-induced cluster formation in the atmosphere. *Science Advances*, 4:1–11, 2018. ISSN 23752548. doi:10.1126/sciadv.aar5218.
- J. Rosell-Llompart, I. G. Loscertales, D. Bingham, and J. Fernández de la Mora. Sizing nanoparticles and ions with a short differential mobility analyzer. *Journal of Aerosol Science*, 27(5):695–719, 1996. ISSN 00218502. doi:10.1016/0021-8502(96)00016-X.
- H. G. Scheibel and J. Porstendörfer. Generation of monodisperse Ag- and NaCl-aerosols with particle diameters between 2 and 300 nm. *Journal of Aerosol Science*, 14(2):113–126, 1983. ISSN 00218502. doi:10.1016/0021-8502(83)90035-6.
- J. H. Seinfeld and S. N. Pandis. *Atmospheric chemistry and physics: from air pollution to climate change*. Wiley, Hoboken, New Jersey, 3rd edition, 2016. ISBN 9781119221166.
- M. Sipilä, T. Berndt, T. Petäjä, D. Brus, J. Vanhanen, F. Stratmann, J. Patokoski, R. L. Mauldin, A. P. Hyvärinen, H. Lihavainen, and M. Kulmala. The role of sulfuric acid in atmospheric nucleation. *Science*, 327(5970):1243–1246, 2010. ISSN 00368075. doi:10.1126/science.1180315.
- D. V. Spracklen, K. S. Carslaw, M. Kulmala, V. M. Kerminen, G. W. Mann, and S. L. Sihto. The contribution of boundary layer nucleation events to total particle concentrations on regional and global scales. *Atmospheric Chemistry and Physics*, 6(12):5631–5648, 2006. ISSN 16807324. doi:10.5194/acp-6-5631-2006.
- G. Steiner, M. Attoui, D. Wimmer, and G. P. Reischl. A medium flow, high-resolution Vienna DMA running in recirculating mode. *Aerosol Science and Technology*, 44:308–315, 2010. ISSN 02786826. doi:10.1080/02786821003636763.

- M. R. Stolzenburg and P. H. McMurry. Equations governing single and tandem DMA configurations and a new lognormal approximation to the transfer function. *Aerosol Science and Technology*, 42(6):421–432, 2008. ISSN 02786826. doi:10.1080/02786820802157823.
- C. Tauber, S. Brilke, P. J. Wlasits, P. S. Bauer, G. Köberl, G. Steiner, and P. M. Winkler. Humidity effects on the detection of soluble and insoluble nanoparticles in butanol operated condensation particle counters. *Atmospheric Measurement Techniques*, 12:3659–3671, 2019. doi:10.5194/amt-12-3659-2019.
- S. A. Twomey, M. Piepgrass, and T. L. Wolfe. An assessment of the impact of pollution on global cloud albedo. *Tellus*, 36 B(5):356–366, 1984. ISSN 16000889. doi:10.3402/tellusb.v36i5.14916.
- A. Wiedensohler. An approximation of the bipolar charge distribution for particles in the submicron size range. *Journal of Aerosol Science*, 19(3):387–389, 1988. ISSN 00218502. doi:10.1016/0021-8502(88)90278-9.
- W. Winklmayr, G. P. Reischl, A. Lindner, and A. Berner. A new electromobility spectrometer for the measurement of aerosol size distributions in the size range from 1 to 1000 nm. *Journal of Aerosol Science*, 22(3):289–296, 1991. doi:10.1016/S0021-8502(05)80007-2.
- P. J. Wlasits. On the Effect of Relative Humidity on the Activation of Aerosol Particles in Butanol Based Condensation Particle Counters. Master’s thesis, University of Vienna, 2019. URL <http://othes.univie.ac.at/>.
- B. E. Wyslouzil and J. Wölk. Overview: Homogeneous nucleation from the vapor phase - The experimental science. *Journal of Chemical Physics*, 145(21), 2016. ISSN 00219606. doi:10.1063/1.4962283.

Chapter 2

Precision characterization of three ultrafine condensation particle counters using singly charged salt clusters in the 1 - 4 nm size range generated by a bipolar electrospray source

This chapter was submitted by S. Brilke, J. Resch, M. Leiminger, G. Steiner, C. Tauber, P.J. Wlasits & P.M. Winkler to *Aerosol Science and Technology* on Sep 26 2019 and has been accepted for publication on Dec 11 2019.

doi: <https://doi.org/10.1080/02786826.2019.1708260>.

Abstract. Molecular singly charged clusters generated by electrospray sources are commonly used for calibration measurements of ultrafine Condensation Particle Counters (CPCs) in the sub-2 nm size range. This technique has been limited to the smallest singly charged clusters. In this study, we used a bipolar electrospray source combining two electrosprays of opposite polarities to generate singly charged clusters of ammonium salts dissolved in acetonitrile, i.e. tetra-heptyl ammonium bromide (THABr) and tetra-butyl ammonium iodide (TBAI) clusters. A high-resolution UDMA acts as a classifier for positively and negatively charged clusters which are used as mobility standards for the measurement of the complete ascent of the detection efficiency curve of three ultrafine CPCs. The CPCs characterized in this work are two laminar flow-type CPCs using n-butanol (TSI UCPC Model 3776, TSI Inc., Minneapolis, USA) and diethylene glycol (DEG) (TSI UCPC Model 3777, TSI Inc., Minneapolis, USA) as working fluid and the turbulent mixing-type DEG-based Particle Size Magnifier (Airmodus A10 PSM). The clusters generated by the bipolar electrospray source are analyzed for their elemental composition using the Atmospheric Pressure interface Time-Of-Flight mass spectrometer (ioniAPi-TOF, Ionicon Analytik GmbH, Austria) in positive and negative ion mode. We present mobility-dependent mass spectra from experiments using the UDMA and the ioniAPi-TOF in series for the analysis of positively charged clusters when operating the electrospray source in unipolar and in bipolar mode to demonstrate the charge reduction and purity of the sample.

2.1 Introduction

The study of new particle formation has encouraged the development of instrumentation capable of analyzing nanoparticles at the transition from molecular clusters to newly formed particles. In recent years, the Atmospheric Pressure interface Time-of-Flight mass spectrometer (APi-TOF) has become a common technique for the analysis of single ions to molecular clusters in laboratory and field experiments (Junninen et al., 2010). The APi-TOF instrument enabled the measurement of charged clusters at mobility equivalent diameters between 1 - 2 nm during new particle formation (Almeida et al., 2013). Bridging the gap between the measurement of large molecular clusters and the lower detection limit of particle counters has become a major challenge in aerosol science. The number concentration of particles is commonly inferred from particle counting by optical detection subsequent to condensational growth. The cut-off diameter, i.e. the size where 50 % of particles are detected, is a parameter characterizing a Condensation Particle Counter's (CPC's) performance. For ultrafine CPCs, the cut-off diameter lies in the size range between 1 and 4 nm depending on the working fluid, working principle and instrument design. Detailed instrument characterization studies are therefore essential to follow the growth of newly formed particles. Aerosol standards with nanometer dimensions for instrument calibration are produced by means of electrospray generation. Previous studies (Kangasluoma et al., 2013; Ude and Fernández de la Mora, 2005) have demonstrated that solutions of tetra-alkyl ammonium halides are well-suited for the clean generation of mobility standards at inverse mobilities below 2 Vs/cm^2 for instrument calibration (Cai et al., 2018; Jiang et al., 2011). It should be noted though that the mobility spectra for cluster ions electrosprayed from tetra-alkyl ammonium halides are dominated by larger multiply charged clusters leading to a too pronounced background to distinguish mobility peaks of singly charged clusters (Attoui et al., 2013). The analysis of mass spectra showed distinct presence of peaks assigned to multiply charged clusters from tetra-heptyl ammonium bromide (Fernández de la Mora et al., 2005). The technique of generating mobility standards from electrospray has so far been limited to the smallest clusters consisting of monomers and dimers due to the dominant presence of higher charge states. Therefore, counting efficiencies obtained from mobility standards were typically limited to 1 - 3 data points omitting major parts of a counting efficiency curve. The high background composed of cluster ions at higher charge states can be reduced by means of controlled neutralization by exposing the cluster ions to ions of opposite polarity produced by e.g. an aerosol neutralizer (Steiner et al., 2017) or their direct counter-ions (Fernández de la Mora and Barrios-Collado, 2017). The latter technique has the advantage that exact knowledge of the chemical composition of the counterpart ions is given. In this study, we exploit the technique of combining two electrospray sources described in the study of Fernández de la Mora and Barrios-Collado (2017) for the generation of dominantly singly charged clusters for the calibration of three different com-

mercially available ultrafine CPCs. Prior to counting efficiency measurements, the generated clusters are analyzed to ensure exact knowledge of the sample composition.

Ultrafine CPCs have a detection limit in the 1 - 3 nm mobility diameter size range depending on the supersaturation of the condensing vapor that the aerosol sample is exposed to. Various approaches have been made to activate the smallest particles. A laminar flow butanol-based CPC (Stolzenburg and McMurry, 1991) has become a standard instrument for particle counting and paved the way for the commercially available and widely used TSI UCPC Model 3776 which was characterized in this study at modified temperature settings. The use of different working fluids in laminar flow CPCs (Iida et al., 2009; Wimmer et al., 2013) has further decreased the lowest detectable particle size. The second particle counter characterized in this study is a laminar flow DEG-based particle counter that is commercially available as the TSI UCPC Model 3777. Subsequent to particle activation, particles are detected in a “booster”-stage butanol-based CPC (TSI CPC Model 3772). Further research on instrument design and working principle to achieve high supersaturation for the promotion of condensational growth have led to the development of mixing-type CPCs (Sgro and Fernández de la Mora, 2004) such as the commercially available Airmodus A10 PSM (Vanhanen et al., 2011) which exposes the aerosol sample to a DEG vapor in a turbulent mixing chamber to achieve supersaturation and activate condensational growth. The Airmodus PSM is the third instrument that was implemented in the experimental setup of this study in combination with the Airmodus A20 butanol-based CPC. The above-mentioned CPC types are widely used for number concentration as well as size distribution measurements when coupled to a Differential Mobility Analyzer (DMA) that classifies particles according to their electrical mobility in both laboratory and ambient environments. Evidently, number concentration and size distribution measurements in the size range of the cut-off diameter require detailed instrument characterization. Uncertainties on the number size distribution in the size range of freshly nucleated particles are especially sensitive to the detailed knowledge of the detection efficiency curve (Kangasluoma and Kontkanen, 2017). Therefore, it is of large experimental interest to have a variety of aerosol standards in the critical mobility size range available.

In this work, we first present mass spectra obtained by the ioniAPi-TOF (Ionic Analytik GmbH, Austria) in positive ion mode and directly compare mass and mobility spectra when the electrospray source is operated in unipolar and in bipolar mode. Further, we demonstrate results from an experimental setup comprising three commercially available ultrafine CPCs, which are characterized in parallel using the molecular clusters generated by the electrospray source in both polarities, and positively and negatively charged silver particles produced from a tube furnace.

2.2 Experimental Methods

Cluster generation from the bipolar electrospray source

The bipolar electrospray source was described recently (Fernández de la Mora, 2018; Fernández de la Mora and Barrios-Collado, 2017) and is commercially available from SEADM, S.L., Spain. A stainless-steel chamber combines two electrospray capillaries that are inserted into two vial holders containing the analyte solution which are set at opposite high voltages. The analyte solution is pushed to the capillary tips (silica capillaries, 125 μm inner diameter) which are electrostatically separated by a 50 % transparent stainless-steel mesh. Different mesh sizes are available to separate the capillary tips. In this study, we used a mesh that isolates the two electrospray regions to the center point of the bipolar electrospray chamber (half mesh). The bipolar electrospray source chamber is filled with a dry and clean carrier gas which transports charge reduced ions to the next stage. The relative humidity (RH) of the transport gas was monitored and was found $< 2\%$ using SHT75 sensors with an accuracy of $\pm 1.8\%$ RH. The approach for charge reduction of combining ions of a certain composition with their counter-ions gives control of the composition of the anion and cation. By reducing the charge state, dominantly singly charged clusters are generated. For the generation of charged clusters, tetra-butyl ammonium iodide (TBAI) and tetra-heptyl ammonium bromide (THABr), are dissolved in acetonitrile at a concentration of 1 mMol/L. Positively and negatively charged clusters of the form $(A^{+/-})_z(AB)_n$ were produced, where n is the number of neutral pairs in the cluster and z the number of cations. The ideal position of the two capillaries, i.e. where the single electrospray currents measured by two nano-amperemeters are independent from each other, was empirically determined. The electrospray currents between 100 – 200 nA were found to be most stable over time periods for a measurement run of 1 – 2 hours when the pressure applied to the vials containing the analyte solution was kept between 1 – 10 mbar. Cleanliness of the sample solution and the capillaries proved to be of essential importance, therefore the capillaries were rinsed through multiple times using ethanol and methanol before and after each measurement run.

For the calibration of the CPCs, it is critical that only singly charged clusters are present in the sample. Therefore, a cluster composition analysis is conducted using the ioniAPi-TOF in positive and negative ion mode. Second, a reference measurement of the counting efficiency is performed using silver particles generated by a tube furnace and subsequent particle charging in an ^{241}Am charger. With this setup, a charge state of ± 1 of the classified silver particles at sizes below 5 nm can be assumed (Fuchs, 1963) and the resulting counting efficiency used as a reference.

To ensure that the electrospray is run at optimum conditions, both electrospray currents need to be carefully adjusted so that symmetric sprays of positive and negative polarity can be

established. The approach in this study is to classify one resolvable peak at a mobility equivalent diameter that is in the size range where the counting efficiency reaches its maximum value (plateau) and compare the number concentration measured by the CPC and a Faraday Cup Electrometer (FCE) at varying ratio of the electrospray currents. The FCE used here was developed at the University of Vienna and is based on the design presented by Winklmayr et al. (1991) with an improved response time of 0.1 s. When the counting efficiency approaches the expected value, it can be inferred that singly charged clusters clearly dominate the sample. An example demonstration is displayed in Figure 2.9 with additional details in the online Supplementary Information (SI).

Mobility and mass analysis

The intention of this study is to verify that solely singly charged cluster ions are classified in the Vienna-type high-resolution UDMA (Steiner et al., 2010). Large multiply charged ions having the same electrical mobility would pass through the DMA and lead to multiple counts in the FCE, which we used as the reference instrument during the counting efficiency measurements. The clusters generated by the electrospray source in unipolar and bipolar mode were analyzed by coupling the DMA to the ionAPI-TOF, which is described elsewhere (Leiminger et al., 2019), in positive/negative ion mode (see Figure 2.1 (a)). The tandem DMA-MS technique has been used in previous studies, e.g. on electrosprayed ionic liquid nanodrops (Hogan and Fernández de la Mora, 2009), tetra-hexyl ammonium bromide clusters (Rus et al., 2010) and THABr clusters (Fernández de la Mora et al., 2005). Limitations of this setup are given by resolution power of the DMA, transmission of the DMA and mass-dependent transmission of the mass spectrometer (Heinritzi et al., 2016; Leiminger et al., 2019).

The Vienna-type high resolution DMA used in this study is referred to as UDMA-4 which was designed to measure mobilities of clusters and ions down to 1 nm. The precursor prototype to the UDMA-4 is the UDMA-1, which was found to have a comparatively large resolution power of 15 to separate charged molecular clusters (Steiner et al., 2010). The design of the cylindrical Vienna-type UDMA-4 was improved for an increased laminarization of the sheath flow and allows to use sheath flow rates between 400 and 1000 L/min. As discussed in Flagan (1999), the resolution power of a DMA is inferred from the ratio of the mobility at the peak of the transfer function to the full width half maximum of the transfer function. At the sheath flow (Q_{sh}) and aerosol flow (Q_a) settings used during the experiments of this study ($Q_{sh} = 1000$ L/min, $Q_a = 10$ L/min), the resolution power of the UDMA-4 was found to be 20 at the size of the THABr monomer at the used experimental conditions.

The large sheath flow rates are not measurable using conventional flow meters, therefore the sheath flow rate is calibrated using a mobility standard. The linear relationship between

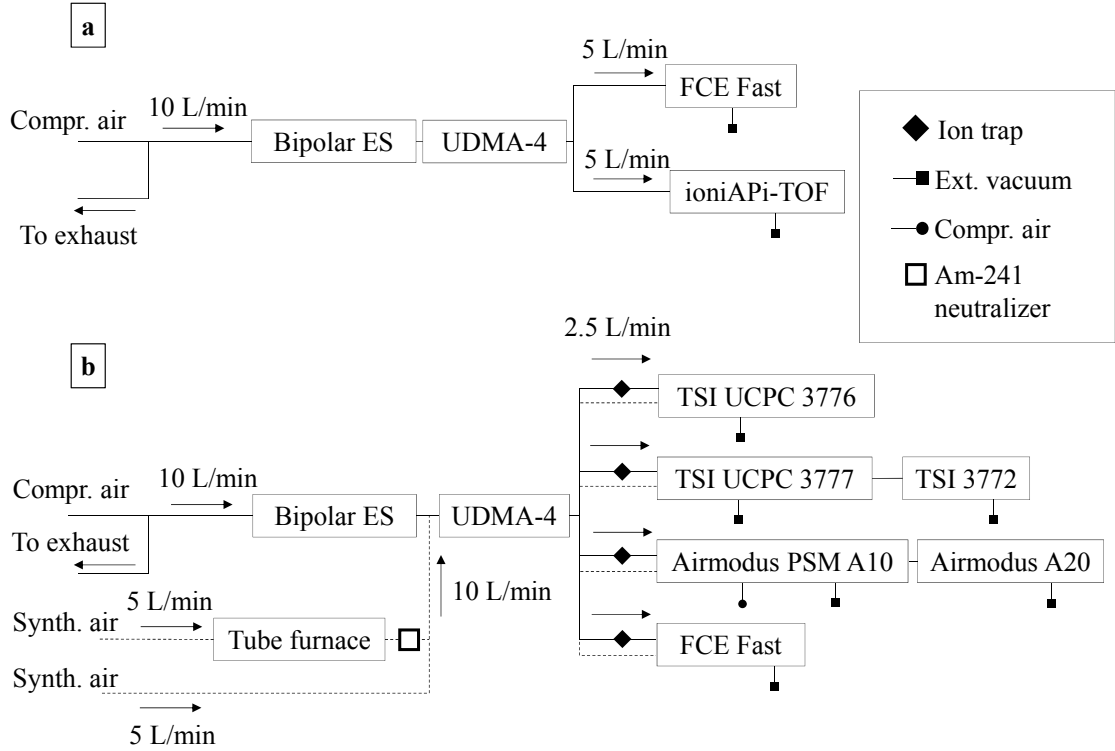


Figure 2.1. Two setups were used to, first (a), analyze the clusters generated by the bipolar electrostatic source by a tandem UDMA-MS setup where positively/negatively charged clusters are classified in the UDMA-4 and subsequently analyzed for their mass-to-charge ratio in the ionAPI-TOF in positive/negative ion mode. Second, panel (b), counting efficiency measurements were conducted using three different ultrafine CPC (TSI UCPC Model 3776, TSI UCPC Model 3777 and Airmodus PSM A10) in parallel and a fast-response FCE as a reference instrument using ion traps at the counter inlets (continuous lines). For the silver measurements, the bipolar electrostatic source is replaced by a tube furnace and silver particles are generated and subsequently charged using an ^{241}Am aerosol neutralizer (dashed lines).

inverse electrical mobility, Z , and set voltage, V , allows to infer the actual flow rate from an operational characterization factor, K :

$$Z^{-1} = K \cdot V \quad (2.1)$$

A fast-response FCE collects charged particles on a filter and measures the electrical current to obtain the mobility spectrum. The centroid electrical mobilities of the resolvable peaks in the mobility spectrum were derived by applying normal (Gaussian) fits to the single mobility peaks. The approximate mobility equivalent diameter, d_Z , was calculated from an empirical formula valid in the particle size range of 0.5 – 5 nm (Mäkelä et al., 1996) as

$$Z = 2.2458 \cdot 10^{-22} \cdot d_Z^{-1.9956} \quad (2.2)$$

The electrical mobility, Z , is given in units of m^2/Vs and the mobility equivalent diameter in m assuming singly charged particles. Note that in the size range of molecular clusters, the mobility equivalent diameter can only be regarded as a convenient size indicator.

In addition to the mobility analysis, the generated clusters were analyzed for their elemental composition using the ioniAPi-TOF with hexapole ion guides. The ion transfer properties of the instrument for the mass range of the analyzed clusters are therefore an important parameter. Compared with APi-TOF instruments with quadrupole ion guides, e.g. APi-TOF MS, Aerodyne Research Inc. and Tofwerk AG, instruments with higher multipole ion guides are assumed to have a broader mass window (Gerlich, 2004). The ioniAPi-TOF was recently characterized regarding ion transmission efficiency, mass range transmission and the effect of ion transfer properties by Leiminger et al. (2019).

We investigated positively charged clusters using the ioniAPi-TOF in positive ion mode when the electrospray was operated in unipolar and bipolar mode. Three-dimensional mass-mobility spectra (Hogan and Fernández de la Mora, 2009; Rus et al., 2010) were obtained using the tandem UDMA-MS setup that is schematically shown in 2.1 (a). The UDMA-4 voltage was stepped at an increment of 10 V and integration of the mass spectra for 15 s in the mass range up to 2000 Th yielded the mass-mobility spectra. Additional non size-resolved measurements were performed in positive ion mode by coupling the electrospray source directly at the ioniAPi-TOF inlet for chemical analysis at increased ion transmission and are presented in the SI, Figure S2. Negatively charged clusters were analyzed using the ioniAPi-TOF in negative ion mode by classifying distinct peaks at a fixed voltage in the UDMA-4 and recording the corresponding mass spectra. The time-of-flight of the ioniAPi-TOF was adjusted to a mass range up to 3400 Th in positive ion mode and up to 5000 Th in negative ion mode.

Counting efficiency measurements

Counting efficiency measurements of the three ultrafine CPCs in parallel were performed using the setup presented in 2.1 (b). Dry and particle-free air is drawn into the high-resolution UDMA-4 at an aerosol flow rate of 10 L/min which is controlled by the individual inlet flow rates of the particle counters which are each set to 2.5 L/min. The relatively high aerosol flow rate of 10 L/min was chosen to be able to characterize the three CPCs in parallel at adequate number concentrations detected in the FCE ($> 1000 \text{ cm}^{-3}$). The UDMA-4 is operated at approx. 1000 L/min sheath flow rate. Subsequently, the flow carrying the particles is evenly split using a four-way splitter and is drawn into the three ultrafine CPCs and the FCE. At each measurement point, the classifier voltage is fixed, and the ion traps set to ground voltage for a duration of 120 s. For the background measurement, the classifier voltage is kept constant with the ion traps set to $\pm 500 \text{ V}$ to remove all charged particles. Since particle counting in the FCE is size-independent, it is used as a reference instrument to infer the counting

efficiency of every CPC. By comparing the number concentration of each CPC, N_{CPC} , to the measured number concentration in the FCE, N_{FCE} , the counting efficiency, η , is determined as

$$\eta = \frac{N_{CPC}}{N_{FCE}} \quad (2.3)$$

When switching the electrospray from unipolar to bipolar mode, an increased neutral background is measured behind the classifier which we assume to originate from the recombination of bipolar ions leading to a high number concentration of neutral particles. A fraction of the neutral particles is still counted by the CPCs when the DMA is in classifier mode. The CPCs count both neutral and charged particles whereas the FCE accounts only for charged particles. Therefore, the CPC number concentration is background corrected by removing all charged particles using the ion traps at the counter's inlets. Simultaneously, the FCE's baseline is determined by removing all charged particles using the ion trap at the FCE inlet. Thus, only the fraction of charged particles measured behind the classifier is accounted for. Depending on the settings of the bipolar electrospray, an increased background is also observed in the FCE, i.e. charged particles, when the classifier is set to zero. This background most likely originates from extraordinarily high ion concentrations that are not completely filtered out by the DMA when operating the electrospray in bipolar mode.

For the counting efficiency measurements, the CPCs and the PSM were operated at temperature and flow settings which allow to have the increase of the detection efficiency curve within the size range of the inverse mobility between 1 – 4 Vs/cm². The PSM saturator temperature was set to 80 °C and the growth tube temperature to 1 °C at 1 L/min saturator flow rate. In principle, the PSM can be operated at settings that further increase the detection efficiency (Kangasluoma et al., 2013). The TSI UCPC Model 3776 was operated at reduced nucleation temperature to increase the supersaturation inside the CPC which mainly determines the CPC detection efficiency (Barmounis et al., 2018). The temperature of the saturator, T_{sat} , was set to 33.1 °C and the condenser temperature, T_c , was decreased from standard factory settings to 1.1 °C which results in $\Delta T = 32$ °C. These temperature settings of the TSI UCPC Model 3776 have been presented by a previous study (Tauber et al., 2019a). The inlet flow rate was augmented to 2.5 L/min to reduce diffusional particle losses at the instrument inlet. Likewise, the TSI UCPC Model 3777 was operated at modified temperature settings with the saturator temperature set to 66 °C and the condenser temperature decreased to 10 °C.

Additional counting efficiency measurements were conducted using silver particles (Ag) generated by a tube furnace (Scheibel and Porstendörfer, 1983) and charged in a bipolar radioactive ²⁴¹Am charger (see Figure 2.1 (b), dashed lines). In the investigated particle size range between 1 and 5 nm, it can be assumed that only singly charged particles enter the DMA. For each measurement, the mean concentration at fixed classifier voltage measured in the CPCs was compared to the mean concentration measured in the FCE for 120 s. The background measurement was performed by setting the classifier voltage to zero to account for possi-

ble homogeneous nucleation inside the CPCs and the FCE noise level. Silver particles are considered as a widely-used standard of a spherical and insoluble test aerosol for laboratory characterization of ultrafine CPCs and therefore serve here as a reference case of a well-studied system (Hermann et al., 2007; Petäjä et al., 2006).

2.3 Results and Discussion

Mobility and mass analysis

The mobility spectra were recorded by the FCE for THABr and TBAI clusters of both polarities and are shown in Figure 2.2. The peaks are labeled with the number of neutral pairs in the cluster, n , where $n = 0$ corresponds to the monomer, $n = 1$ to the dimer and so forth. Contrary to mobility spectra from a unipolar electrospray source (Attoui et al., 2013; Steiner et al., 2010), the presented spectra exhibit a larger number of resolvable peaks which was also shown by Fernández de la Mora and Barrios-Collado (2017). Note that in the positive spectrum for THABr the abundance of the $A^+(AB)_3$ ion peak (tetramer) is lower than its neighboring peaks but clearly resolved. Similar observations have been made by Ude and Fernández de la Mora (2005). During the preparation of our experiments, we found the 50 % transparent half mesh configuration of the bipolar electrospray chamber favorable compared to the full mesh for resolving the tetramer. The electric field and flow configuration in the bipolar electrospray chamber might promote the abundance of the tetramer. For the negative spectrum of TBAI at $n=7,8$ the peaks are not fully resolved. However, we find a range of peaks that can potentially be used as mobility standards. The positive THABr spectra reveal resolvable peaks up to $n=10$, whereas for TBAI clusters up to $n = 18$ can be detected. The inverse electrical mobilities, $1/Z$ [Vs/cm²], of the resulting peaks were determined by fitting a normal (Gaussian) function to the series of peaks up to the decamer. The clusters were classified in the UDMA-4 and the mass-to-charge ratio was measured in the ioniAPi-TOF in either positive or negative ion mode. The experiments were conducted in laboratory conditions at atmospheric pressure, $T=22^\circ\text{C}$ and $\text{RH} < 3.5\%$. The mobility peaks, which were clearly resolved and identified in the ioniAPi-TOF, are listed in Table 2.1 with their inverse electrical mobility, $1/Z$ [Vs/cm²], exact atomic mass, m/z [Th], and approximate diameter, d_Z [nm], calculated from Equation 2.2.

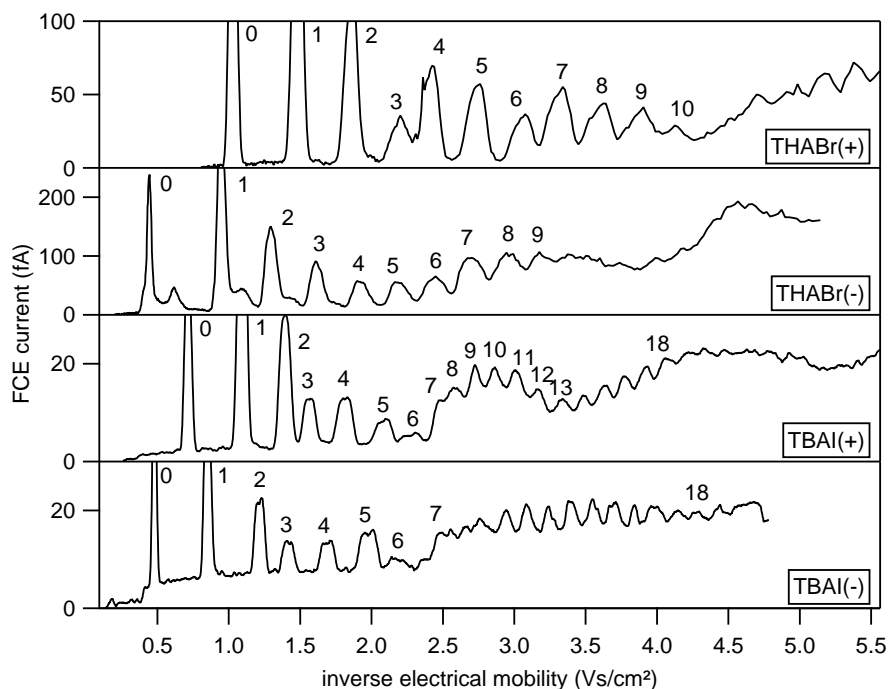


Figure 2.2. Positive and negative mobility spectra of tetra-heptyl ammonium bromide (THABr) und tetra-butyl ammonium iodide (TBAI) cluster ions recorded by the FCE. Peak labels denote the number of neutral pairs in the cluster, n .

For the assignment of mobility peaks to their mass, the UDMA-4 was coupled to the ioniAPi-TOF. The signal measured by the FCE was proved to be sufficiently high and the UDMA-4 resolving power was large enough to clearly distinguish single molecular ions. The ioniAPi-TOF mass calibration was conducted using the clusters generated by the bipolar electrospray source. For the analysis of the mass spectra, m/z values were converted to n/z , where n is the number of neutral pairs in the cluster by calculating (Rus et al., 2010)

$$\frac{n}{z} = \frac{\frac{m}{z} - m_A}{m_{AB}} \quad (2.4)$$

The mass of the cation and cation-ion-pair is given by m_A and m_{AB} , respectively. The representation by n/z gives a clear indication of multiply charged ions present in the spectra which then appear at fractions of the integer values of n/z . Figure 2.3 shows the ratio of number of neutral pairs in the clusters to their charge state vs. the inverse electrical mobility of the cluster in unipolar mode (a, c) and bipolar mode (b, d). Clearly, in unipolar mode, higher charge states clusters are present with doubly charged clusters at half integer n/z values ($z = 2$) and triply charged clusters at third integer values ($z = 3$). Whereas in bipolar mode, these multiply charged ions disappear which suggests the dominant presence of singly charged clusters. We observe large contributions of the smaller monomer and dimer clusters

Table 2.1. Inverse mobility, $1/Z$ [Vs/cm²], and approximated mobility diameter, d_Z [nm], using Equation 2.2 for positively (A^+) and negatively (A^-) singly charged ($z=1$) tetra-butyl ammonium iodide and tetra-heptyl ammonium bromide clusters. The exact atomic mass is listed as m/z [Th].

n	TBAI, A ⁺			THABr, A ⁺			TBAI, A ⁻			THABr, A ⁻		
	1/Z	d_Z	m/z	1/Z	d_Z	m/z	1/Z	d_Z	m/z	1/Z	d_Z	m/z
0	0.71	1.21	242.28	1.03	1.45	410.47	0.48	0.99	126.90	0.44	0.953	78.91
1	1.09	1.5	611.47	1.52	1.77	899.86	0.85	1.32	496.09	0.95	1.40	568.30
2	1.39	1.69	980.66	1.89	1.97	1389.25	1.22	1.58	865.28	1.30	1.63	1057.70
3	1.57	1.79	1349.85	2.23	2.14	1878.64	1.42	1.71	1234.47	1.62	1.82	1547.09
4	1.81	1.93	1719.04	2.45	2.25	2368.03	1.70	1.87	1603.66	1.92	1.99	2036.48
5	2.09	2.07	2088.23	2.79	2.40	2857.42	1.98	2.02	1972.85	2.19	2.12	2525.87
6	-	-	-	3.13	2.54	3346.81	2.18	2.12	2342.04	2.45	2.25	3015.26
7	-	-	-	-	-	-	-	-	-	2.71	2.36	3504.65
8	-	-	-	-	-	-	-	-	-	2.97	2.47	3994.04

when classifying the dimer or trimer, respectively. We suggest that at the transition from ambient pressure to the low pressure in the ioniAPi-TOF smaller clusters ($n < 3$) do not remain intact which results in a source of additional ions at smaller mobilities detected in the ioniAPi-TOF. Similar observations of positively charged THABr clusters have been made by Ude and Fernández de la Mora (2005).

Positive mass-mobility spectra for TBAI reveal similar patterns regarding unipolar vs bipolar mode as demonstrated in Figure 2.3 (c, d). Distinct bands of ions at higher charge states become visible in unipolar mode which are not detected in bipolar mode. Additional peaks appear at higher m/z when the trimer, tetramer and pentamer are classified. Likewise, in the unipolar mobility-mass spectrum we observe signals from the monomer when classifying the dimer. Correspondingly, signals of smaller cluster ions ($n/z = 0, 1, 2, 3$) appear when classifying clusters up to $n/z = 4$. This indicates an instability of the smaller clusters when entering the vacuum system of the mass spectrometer.

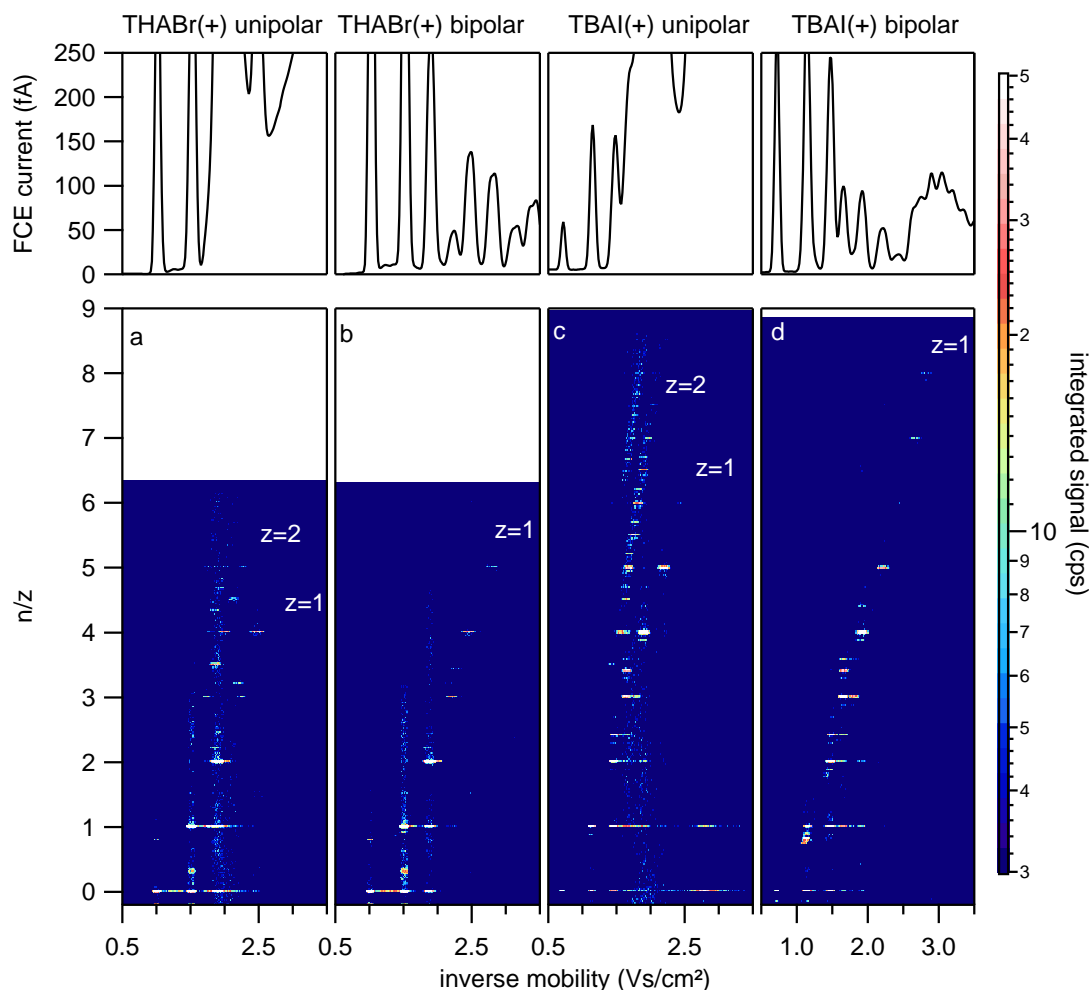


Figure 2.3. The upper panel shows the positive mobility distribution measured in the FCE during each measurement run. Positive mass-mobility spectra from electro sprayed THABr and TBAI clusters are added in the lower panel when the electro spray is operated in unipolar (a, c) and bipolar (b, d) mode. When operated in unipolar mode, the positive electro spray is used only whereas in bipolar mode the positive and negative electro sprays are combined. The color scheme in the mass-mobility spectra shows the logarithmically scaled signal of intensity measured by the ioniAPi-TOF. Panels (a) and (c) show the spectra of clusters when the electro spray is operated in unipolar mode and higher charge states are detected (white labels) for THABr and TBAI clusters. In bipolar mode, higher charge states disappear, (b) and (d).

The resolving power of the DMA is critical to ensure chemical purity of the classified cluster. The mobility spectra shown in Figure 2.2 exhibit non-ideal shapes of the mobility peaks which can be explained by non-idealities in the DMA geometry, i.e. DMA eccentricity. Non-idealities in the DMA eccentricity and thus limited resolving power can generally be addressed by using a different DMA geometry such as a parallel-plate DMA. However, the UDMA-4 resolving power showed to be large enough to resolve single peaks as presented in Figure 2.2.

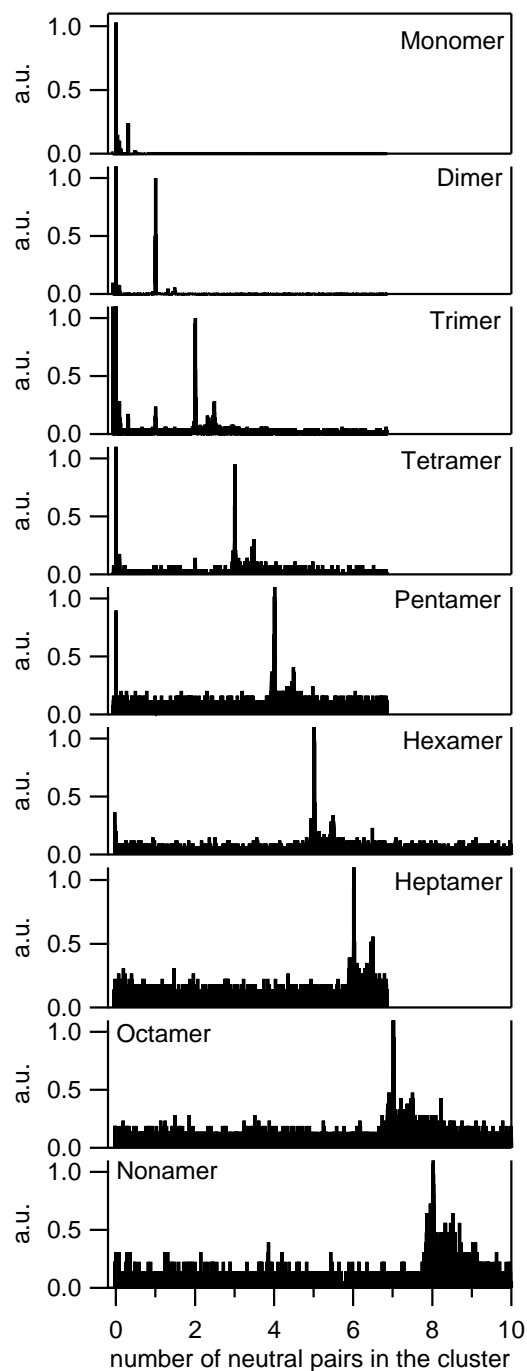


Figure 2.4. Negative mass spectra were measured by the ioniAPi-TOF of THABr for each classified mobility peak in the mobility distributions demonstrated in Figure 2.2. The mass-to-charge ratio was calculated to the number of neutral pairs in the cluster using Equation 2.4 where $m_A=78.92$ Th and $m_{AB}=(78.92 + 410.47)$ Th. The dataset of each classified cluster was normalized to the intensity at the expected cluster mass. The measured intensities of large clusters are low compared to small clusters based on a reduced transmission efficiency of the ioniAPi-TOF at larger masses which in turn have a higher transmission probability in the UDMA-4.

Ion transmission of the tandem DMA-MS setup is limited by the transmission of the UDMA-4 and the ioniAPi-TOF. A higher transmission probability of larger ions is expected in the UDMA-4 while ion transmission in the ioniAPi-TOF is lower at higher m/z due to a decreased duty cycle and lower transmission of heavier ions. The reduced transmission efficiency was accounted for by increasing the sampling duration. The DMA-MS system would benefit from an improved ion transmission in the DMA, which has cylindrical geometry in this case. In principal, a parallel-plate DMA with optimized geometry for cluster transmission is recommended for DMA-MS studies, as shown in Rus et al. (2010). In this study, additional non size-resolved measurements were performed to verify the non-presence of higher charge states by installing the electrospray source directly at the ioniAPi-TOF inlet. The positive mass spectra are presented in Figure S2 (SI). THABr clusters of charge states $z = +2$ are marked in the upper panel and correspond to the m/z values as listed in the study of Fernández de la Mora et al. (2005). These and clusters of higher charge states are substantially reduced in bipolar mode (lower panel) indicating the dominant presence of singly charged clusters.

In principle, negative ions from an electrospray source can cluster with and ionize substances present in the carrier gas. Therefore, the possibility of ion-adducts forming due to impurities in the carrier gas needs to be considered. Negatively charged THABr clusters were analyzed by operating the UDMA-4 in fixed voltage mode and at a sample duration of 1 – 2 hours depending on the signal intensity. Figure 2.4 shows the mass spectra of each classified negatively charged THABr cluster to the number of neutral pairs in the cluster calculated from Equation 2.4. The spectra were normalized to the intensity at the dominant peak, i.e. the expected mass-to-charge ratio or n value, respectively, to facilitate the comparison. The series of dominant peaks is observed at the expected mass-to-charge values for clusters up to 8 neutral pairs per cluster, i.e. the nonamer. Commonly, the instrument resolution of the ioniAPi-TOF substantially decreases at the upper end of the mass range. In this case, at the mass of the monomer ($m/z = 79$ Th) an instrument resolution of 1370 is derived, which decreases for larger masses. The maximum flight-time in the ioniAPi-TOF was increased by reducing the extraction frequency to allow the detection of ions at higher m/z .

When classifying the monomer, dimer and trimer, we observe peaks of clusters of Br^- with acetonitrile and ethanol. Ethanol is used for rinsing the capillaries before and after each measurement run. Though RH in the system is monitored and kept to a minimum (< 3.5 % RH), we also detect Br^- water clusters. In the case of the classified monomer, an additional prominent peak is observed at $m/z = 232$ Th which was not identified here. The relative abundance of this peak to the expected monomer peak at $m/z = 79$ Th is 0.2:1. This peak might originate from Br^- forming adducts with possible impurities in the pressurized air used as carrier gas. At larger clusters, an additional signal at a similar distance to the cluster mass of the classified mobility peak is noted. For classified clusters up to $n = 4$ (pentamer), a monomer

peak is detected with highest relative abundance for the classified trimer (5:1). As discussed earlier, we suggest that the smaller clusters originate from evaporation at the TOF transition which was also suggested by previous tandem DMA-MS studies (Ude and Fernández de la Mora, 2005). At larger clusters ($n > 3$), an additional ion signal in the region of the classified cluster is recorded. Due to the low resolution in this high mass range, these peaks cannot be identified. Since the operational settings are at the experimental limit of the instrument, we cannot exclude that the signal originates from scattering of heavy ions, i.e. the large clusters, at the detector.

In summary, the mass-mobility study of the clusters generated by the bipolar electrospray revealed that, firstly, positive and negative mobility spectra of THABr and TBAI as large as 3 – 4 nm can be obtained using the high-resolution UDMA-4. Second, by stepping the UDMA-4 voltage and sampling positively charged clusters, mass-mobility spectra were generated and the reduction of multiply charged clusters when operating the electrospray in bipolar mode was verified and supported by results from a non-size-resolved measurement of the mass-to-charge ratio (Figure S2, SI). Ultimately, mass spectra recorded by the ioniAPi-TOF in negative ion mode demonstrated that the series of the first mobility peaks corresponds to the expected cluster mass, i.e. mobility peaks were clearly assigned to their mass-to-charge ratio.

2.3.1 CPC counting efficiency

Silver particle measurements

Firstly, we present results from counting efficiency measurements using silver particles to have a reference to a well-known aerosol test substance. The results of the counting efficiency curves from charged silver particles using the tube furnace as aerosol source are presented in Figure 2.5. The counting efficiency is plotted versus the mobility equivalent diameter which is calculated from Equation 2.2. At small sizes, an additional increase of the counting efficiency is observed for the Airmodus PSM and the TSI UCPC Model 3776. In the lower panel of Figure 2.5, the mobility distributions of ions generated by the bipolar ^{241}Am aerosol neutralizer in the absence of particles were added. Clearly, charger ions are activated by the TSI UCPC Model 3776 and, much more pronounced, by the Airmodus PSM when positively charged particles are classified. This observation highlights the importance of accounting for ions produced by the aerosol neutralizer present in the aerosol sample (Hering et al., 2017). The cut-off diameters, at which 50 % of the particles are detected, D_{50} , are listed in Table 2.2. For negatively charged silver particles, we observe a decrease of the cut-off diameter for the TSI UCPC Model 3776 and the TSI UCPC Model 3777. Note that the cut-off diameter for positively charged silver particles of the Airmodus PSM is omitted due to the increased

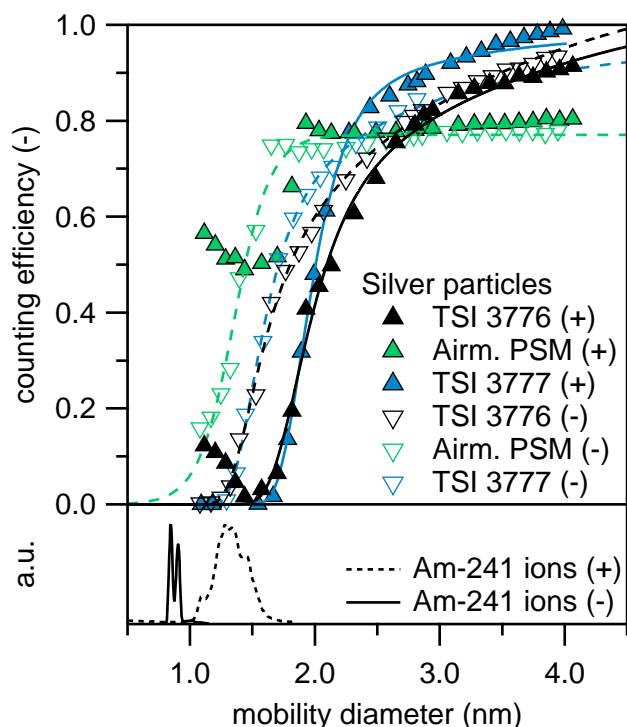


Figure 2.5. Counting efficiency results using positively (+) and negatively (-) charged silver (Ag) particles produced in a tube furnace. The lower panel shows the normalized mobility distribution of charger ions produced in the bipolar ^{241}Am neutralizer in the absence of particles. A sigmoidal fit function was applied to the data points and are presented as continuous (Ag+) and dashed (Ag-) lines.

activation efficiency at small sizes caused by charger ions present in the sample. The reason for a decreased cut-off diameter in the case of negatively charged silver particles remains unclear and ion composition of silver was not measured by this study. Sign preferences regarding the activation probability have been observed by previous studies (Tauber et al., 2019a; Winkler et al., 2008).

Tetra-alkyl ammonium halide cluster measurements

As a next step, we discuss results for mobility standards from positively charged TBAI clusters and compare the plateau height of the activation curves. Figure 2.6 demonstrates the counting efficiency vs. the inverse electrical mobility of the size-selected positively charged TBAI clusters with the corresponding mobility spectrum of the generated clusters shown in the upper panel. Evidently, the plateau of the activation curve approaches the maximum activation efficiency in the 3 – 4 nm range of about 90 % for the TSI 3777 and about 70 % in the PSM. As we have seen in the results of the silver particle measurement in Figure 2.5, the cut-off curves of the TSI 3776 and the TSI 3777 reach a plateau at approximately 4 nm,

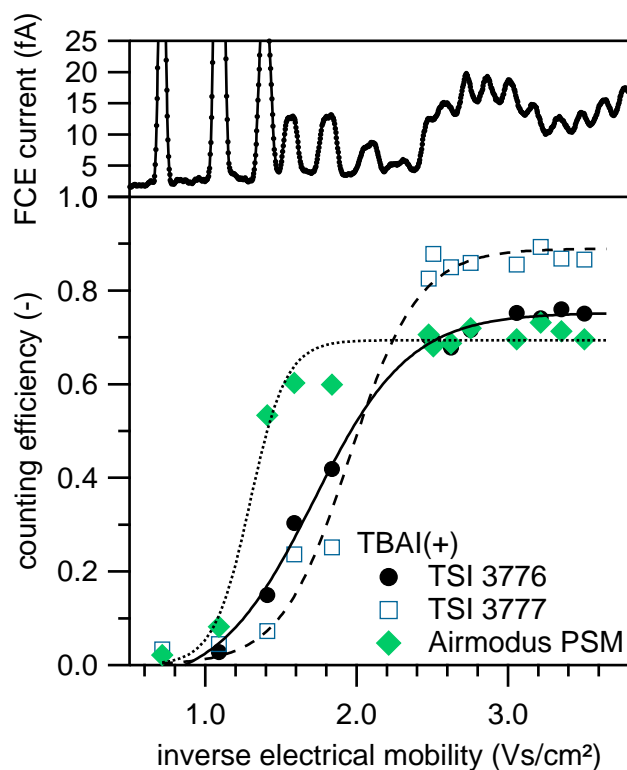


Figure 2.6. Counting efficiency measurements from positively charged TBAI clusters were plotted against the inverse electrical mobility, $1/Z$. The positive mobility spectrum recorded by the FCE is presented in the upper panel. Mobility peaks are classified in the UDMA-4 and are carried into the particle counters, the TSI UCPC Model 3776 and TSI UCPC Model 3777 which are operated at modified temperature setting and the Airmodus PSM. Uncertainties in the counting efficiency are dominated by the 10 % and 5 % counting accuracy of the CPCs and the FCE and are not depicted here.

which corresponds to the maximum activation efficiency in the investigated size range when only singly charged clusters are analyzed. Based on Equation 2.3, the size-selected clusters are therefore equally counted in the CPCs and the FCE when using the mobility standards by the bipolar electrospray. Hence, multiply charged clusters are negligible in the sample which would lead to overcounting in the FCE and thus an underestimated counting efficiency. Figure 2.7 summarizes the counting efficiency measurements for the two tetra-alkyl ammonium halides for both polarities and the resulting cut-off diameters are reviewed in Table 2.2. An overview of the resulting cut-off diameters for the different substances and CPCs is given in Figure 2.8. The error bars in Figure 2.8 were estimated from the UDMA-4 resolution at the monomer peak during each measurement run. Results of the study by Kangasluoma et al. (2016), which included the investigation of the activation behavior of three different CPC's using THABr clusters generated from a tube furnace and subsequent charging in an ^{241}Am charger, were added as black markers.

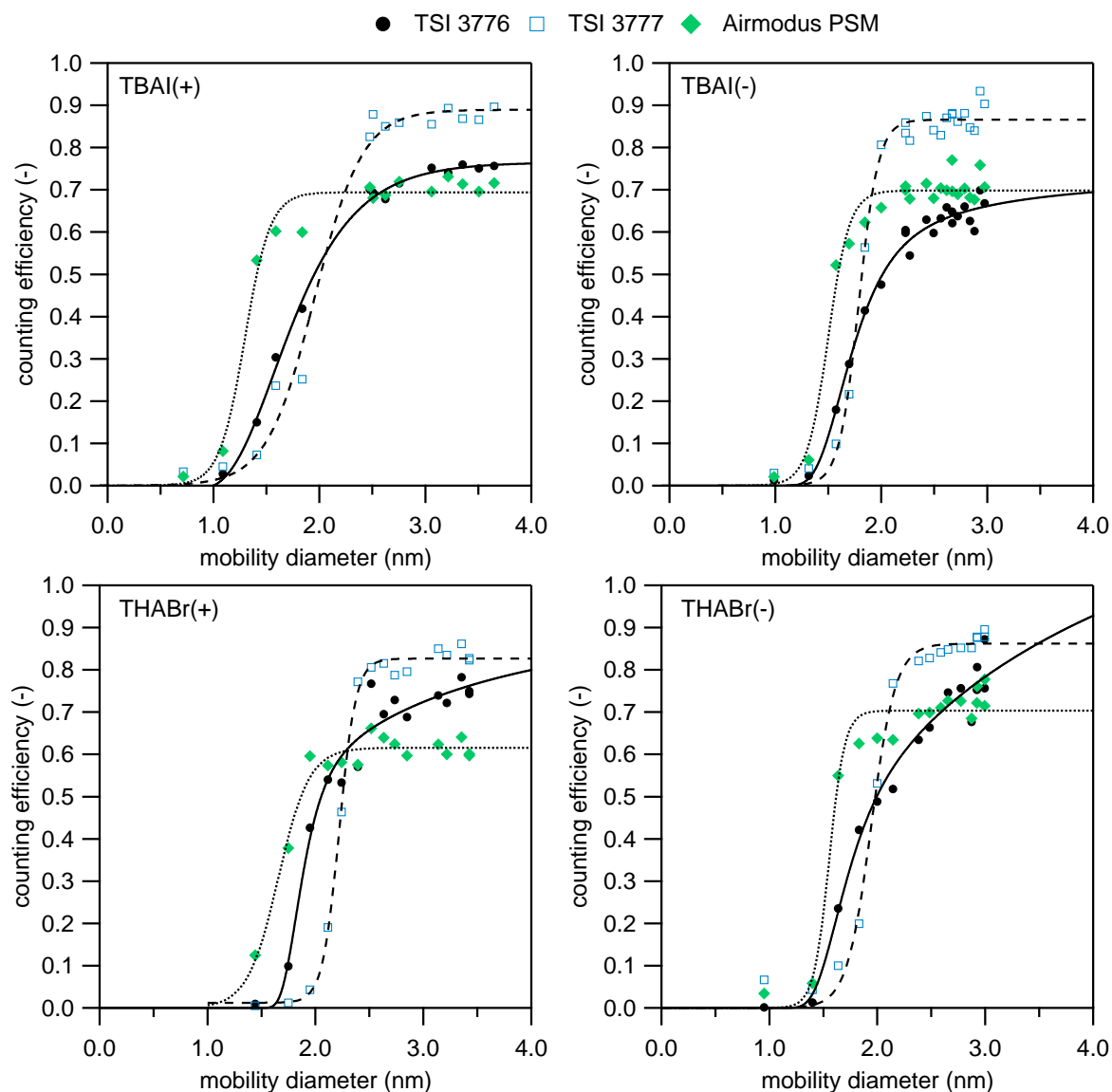


Figure 2.7. Results of the counting efficiency measurements using positively and negatively charged THABr and TBAI clusters generated by the bipolar electro spray source vs. the mobility equivalent particle diameter. A sigmoidal fit function was applied to the data points and are presented as continuous (TSI UCPC Model 3776), dashed (TSI UCPC Model 3777) and dotted (Airmodus PSM) lines.

A trend towards an improved activation efficiency, i.e. lower cut-off diameter, can be observed for the DEG-based counters with lowest cut-off diameters for the turbulent mixing-type Airmodus PSM (see Figure 2.8). However, least scattering of the results when different substances and polarities are tested is found for the modified TSI UCPC Model 3776. Indeed, the cut-off diameters from the tetra-alkyl ammonium halides agree within the measurement uncertainty (see Figure 2.8). This finding suggests a reduced composition dependency of the

Table 2.2. Cut-off diameters, D_{50} , in nm at 50 % counting efficiency for the three characterized particle counters. The TSI UCPC Model 3776 and the TSI UCPC Model 3777 were operated at modified temperature settings.

Substance	Polarity	TSI 3776	TSI 3777	Airmodus PSM
Ag	+	2.10	2.0	-
	-	1.80	1.71	1.45
TBAI	+	1.95	2.01	1.41
	-	2.01	1.81	1.59
THABr	+	2.05	2.25	1.86
	-	2.0	1.98	1.61

cut-off diameter for the butanol based and modified TSI UCPC Model 3776. Based on the study of Barmounis et al. (2018), a maximum saturation ratio of about 4.6 is achieved in a butanol-based laminar flow type CPC for the temperature settings at $\Delta T = 32^\circ\text{C}$ at reduced condenser temperature. Tauber et al. (2019b) derived a maximum of the saturation ratio between 4.5 and 4.6 for the TSI UCPC Model 3776 which was used in this study. In a previous study by Tauber et al. (2018) negatively charged THABr/TBAI monomer, Br^- and I^- , are found to activate at saturation ratios between 4.47 and 4.57 using an adiabatic expansion-type particle counter and n-butanol vapor. The activation of monoatomic ions with a mobility diameter close to 1 nm would be possible according to the estimated supersaturation profile inside the CPC condenser. Hence, the cut-off diameter at 2 nm can be attributed to the CPC geometry and flow settings, e.g. diffusional losses in the capillary at the saturator inlet at a flow rate of 0.05 L/min. The TSI UCPC Model 3777 operates at a capillary flow rate of 0.15 L/min and yields lowered cut-off diameters compared to the TSI UCPC Model 3776 which supports limitations due to inlet geometries and flow rate settings. However, the activation in the DEG-based TSI UCPC Model 3777 will differ from the activation achieved in the TSI UCPC Model 3776. Since the PSM activation is based on supersaturation from turbulent mixing of the supersaturated vapor and the aerosol sample, higher activation efficiencies can be accomplished (Kangasluoma et al., 2013; Vanhanen et al., 2011). The resulting cut-off diameters from the study of Kangasluoma et al. (2016) are comparable to the results of this study. However, note that the CPC operational settings were different.

A tendency to improved detection, i.e. lower cut-off diameter, of TBAI towards THABr clusters is observed for the DEG-based counters, see Figure 2.7. TBAI and DEG are both relatively polar in contrast to THABr and n-butanol. A better solubility of TBAI in DEG

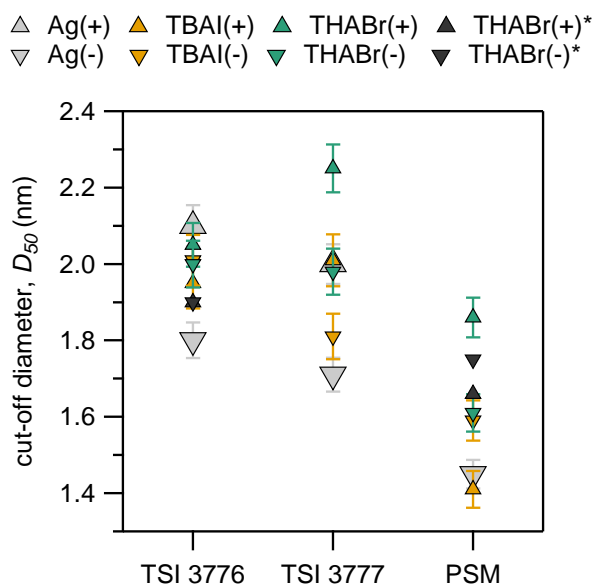


Figure 2.8. Summary of the resulting cut-off diameters (listed in Table 2.2) for the TSI UCPC Model 3776, the TSI UCPC Model 3777 and the Airmodus PSM using silver particles, THABr and TBAI as test aerosols. Upward arrows represent positively charged particles and downward arrow negatively charged particles, respectively. Measurement uncertainties were derived from the UDMA-4 resolution using the positive THABr monomer as calibrant ion. Results of THABr measurements from the study of Kangasluoma et al. (2016) were added as black markers(*), note that the counters were operated here at different settings.

can therefore be expected and explain the lower cut-off diameter.

A polarity dependence cannot be inferred from the cut-off diameters for the tetra-alkyl ammonium halides (see Figure 2.8). With clusters being composed of either a surplus of a cation or anion, structural effects, i.e. the composition of the sample, on the cut-off diameter might dominate over the polarity of the cluster (Kangasluoma et al., 2013).

2.4 Conclusion

The bipolar electrospray source proved to be a powerful tool to generate bipolar mobility spectra dominated by singly charged clusters from THABr and TBAI when coupled with the UDMA-4 at decent concentrations for subsequent analysis and instrument calibration purposes. In combination with the ioniAPi-TOF in positive and negative ion mode, mobility peaks were clearly assigned to their masses for clusters up to the nonamer. Effective reduction of higher charge states of ions generated from the electrospray when switching from unipolar to bipolar mode was confirmed from the ioniAPi-TOF measurement.

We have demonstrated that the mobility standards generated by the bipolar electrospray

source can be used to characterize ultrafine CPCs. Counting efficiency measurements were performed for two laminar flow CPCs using n-butanol and DEG as working fluid (TSI UCPC Model 3776 and 3777) at modified temperature settings and the turbulent mixing type Airmodus PSM in the 1 – 4 nm size range. The comparison of CPC and FCE concentration at larger classified clusters confirmed that the aerosol sample consists of essentially singly charged clusters when comparing the resulting cut-off curves to the results from the silver measurements. The generation of dominantly singly charged clusters can be concluded from the combined results of the counting efficiency measurements and the chemical analysis.

The cut-off analysis using high-resolution mobility classification showed a significantly reduced composition dependency when using the butanol-based TSI UCPC Model 3776 at modified temperature settings compared to the DEG-based TSI UCPC Model 3777 and Airmodus PSM. This finding is of general interest for the measurement of sub-3 nm particle concentration and size distribution measurement of newly formed particles, especially when the composition of the sample is not known during ambient measurements. Given its precision in the size and composition of seed particles the setup presented here may well serve as a calibration standard in future CPC calibration studies.

2.5 Supplemental Information

2.5.1 Adjustment of the settings of the bipolar electro spray source

An exemplary demonstration of the procedure for choosing the right settings of the electro spray is given in Figure 2.9 (SI). In the upper panel, the increase in the background measured by the FCE is presented. The FCE background, i.e. a surplus of positive or negative ions behind the DMA, arises when the bipolar electro spray switches from unipolar to bipolar mode. By adjusting the electro spray currents, the background can be reduced to zero. At those settings, the electro spray is assumed to be run at symmetric spray conditions. The counting efficiency of two low cut-off CPCs measured at each electro spray current setting reaches a plateau for high enough current ratios as is displayed in the lower panel of Figure 2.9. This behavior is linked to a high enough abundance of counter-ions leading to efficient charge reduction of ions at higher charge states. By the described procedure, the electro spray currents are adjusted prior to each measurement.

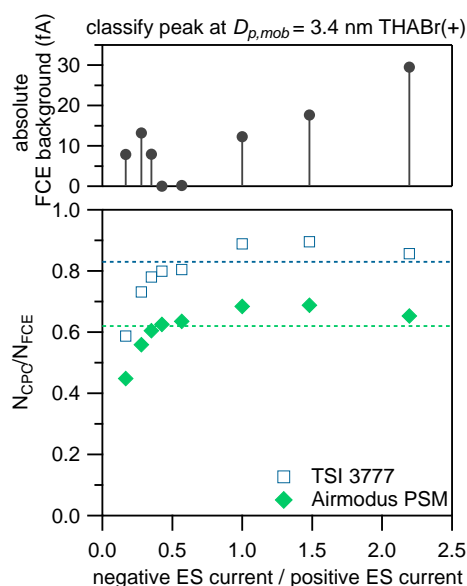


Figure 2.9. Example demonstration of the adjustment of the electro spray currents when classifying a large positive THABr cluster at an approximate mobility equivalent diameter of 3.4 nm. Note that these electro spray settings individually depend on the capillary geometry and capillary tip position. In the upper panel, the absolute FCE background when switching from unipolar to bipolar mode is displayed for different ratios of the negative to positive electro spray current. The lower panel shows the counting efficiency measured by the TSI 3777 and Airmodus PSM for each ratio of the currents. At current ratios between approx. 0.5 – 1, the FCE background decreases to zero. The dashed lines mark the value of the counting efficiency curves as shown in Figure 2.7.

2.5.2 Non size-resolved composition measurement of clusters generated by the bipolar electro spray source

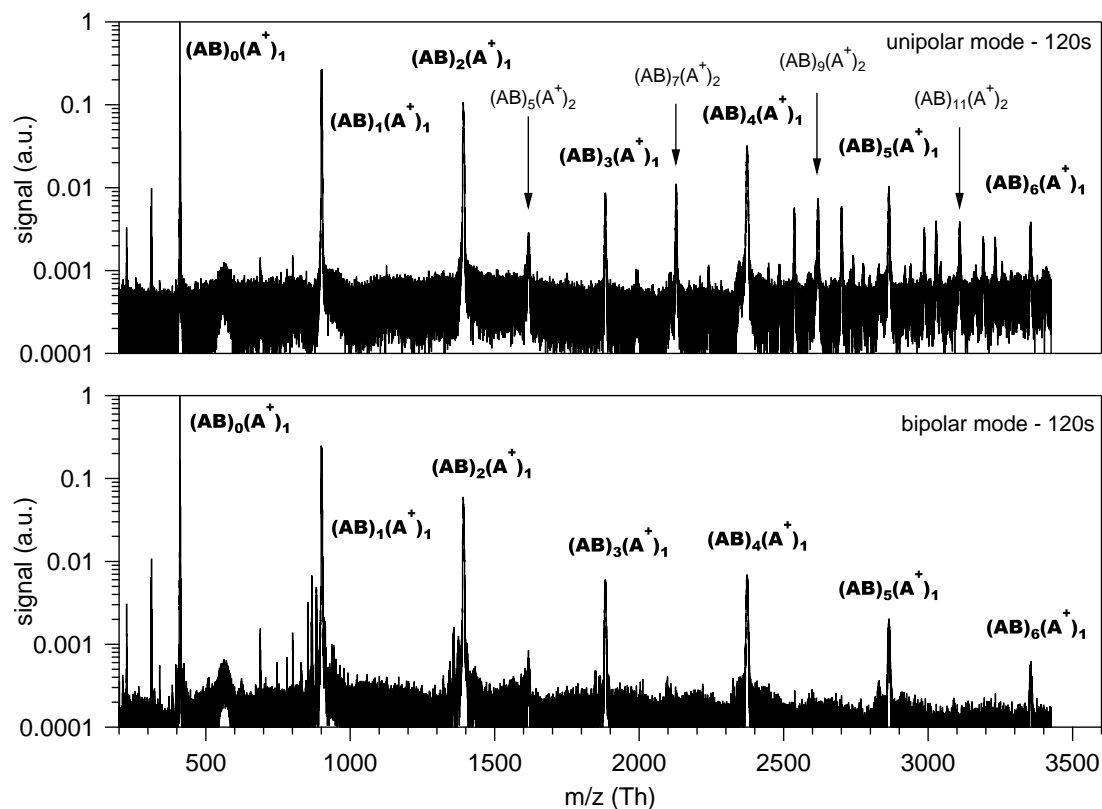


Figure 2.10. Positive mass spectra of THABr averaged over 120 s of clusters generated from the bipolar electro spray directly installed to the ioniAPI-TOF inlet. The upper panel shows the resulting clusters when operating the electro spray in unipolar (positive) mode, the lower panel the spectrum when having switched to bipolar mode. The ion signal was normalized to the intensity of the monomer peak. The bold text marks the peak that are assigned to singly charged clusters, $z = +1$, of the form $(AB)_n(A^+)_1$. The arrow markers show clusters at charge states $z = +2$, that correspond to the doubly charged species as presented in Fernández de la Mora et al. (2005).

2.6 Author Contributions

S.B., J.R. and G.S. designed the setup, S.B., J.R., M.L., C.T. and P.J.W. performed the measurements, S.B., J.R., M.L., G.S., C.T., P.J.W. and P.M.W. were involved in the scientific interpretation and discussion, and S.B. wrote the manuscript.

2.6.1 Personal Contributions

The development of the experimental setup was performed by myself. Prior to the measurements shown in this study, several adjustments to the setup and measurement method had been needed to generate reproducible data. All data shown here originate from my own measurements including the operation of the APi-TOF MS. The data analysis was done by me. The scientific interpretation of the data was conducted in collaboration with the co-authors of the study. I wrote the manuscript and did the main part of the review process of the paper.

2.7 References

- J. Almeida, S. Schobesberger, A. Kürten, I. K. Ortega, O. Kupiainen-Määttä, A. P. Praplan, A. Adamov, A. Amorim, F. Bianchi, M. Breitenlechner, A. David, J. Dommen, N. M. Donahue, A. Downard, E. Dunne, J. Duplissy, S. Ehrhart, R. C. Flagan, A. Franchin, R. Guida, J. Hakala, A. Hansel, M. Heinritzi, H. Henschel, T. Jokinen, H. Junninen, M. Kajos, J. Kangasluoma, H. Keskinen, A. Kupc, T. Kurtén, A. N. Kvashin, A. Laaksonen, K. Lehtipalo, M. Leiminger, J. Leppä, V. Loukonen, V. Makhmutov, S. Mathot, M. J. McGrath, T. Nieminen, T. Olenius, A. Onnela, T. Petäjä, F. Riccobono, I. Riipinen, M. Rissanen, L. Rondo, T. Ruuskanen, F. D. Santos, N. Sarnela, S. Schallhart, R. Schnitzhofer, J. H. Seinfeld, M. Simon, M. Sipilä, Y. Stozhkov, F. Stratmann, A. Tomé, J. Tröstl, G. Tsagkogeorgas, P. Vaattovaara, Y. Viisanen, A. Virtanen, A. Vrtala, P. E. Wagner, E. Weingartner, H. Wex, C. Williamson, D. Wimmer, P. Ye, T. Yli-Juuti, K. S. Carslaw, M. Kulmala, J. Curtius, U. Baltensperger, D. R. Worsnop, H. Vehkamäki, and J. Kirkby. Molecular understanding of sulphuric acid-amine particle nucleation in the atmosphere. *Nature*, 502(7471):359–363, 2013. ISSN 00280836. doi:10.1038/nature12663.
- M. Attoui, M. Paragano, J. Cuevas, and J. Fernández de la Mora. Tandem DMA Generation of Strictly Monomobile 1 - 3.5 nm Particle Standards. *Aerosol Science and Technology*, 47(5):499–511, 2013. doi:10.1080/02786826.2013.764966.
- K. Barmounis, A. Ranjithkumar, A. Schmidt-Ott, M. Attoui, and G. Biskos. Enhancing the detection efficiency of condensation particle counters for sub-2 nm particles. *Journal of Aerosol Science*, 117:44–53, 2018. ISSN 0021-8502. doi:10.1016/j.jaerosci.2017.12.005.
- R. Cai, M. Attoui, J. Jiang, F. Korhonen, J. Hao, T. Petäjä, and J. Kangasluoma. Characterization of a high-resolution supercritical differential mobility analyzer at reduced flow rates. *Aerosol Science and Technology*, 52(11):1332–1343, 2018. ISSN 15217388. doi:10.1080/02786826.2018.1520964.
- J. Fernández de la Mora. Mobility Analysis of Proteins by Charge Reduction in a Bipolar Electrospray Source. *Analytical Chemistry*, 90(20):12187–12190, 2018. ISSN 0003-2700. doi:10.1021/acs.analchem.8b03296.
- J. Fernández de la Mora and C. Barrios-Collado. A bipolar electrospray source of singly charged salt clusters of precisely controlled composition. *Aerosol Science and Technology*, 51(6):778–786, 2017. ISSN 0278-6826. doi:10.1080/02786826.2017.1302070.
- J. Fernández de la Mora, B. A. Thomson, and M. Gamero-Castaño. Tandem Mobility Mass Spectrometry Study of Electrosprayed Tetraheptyl Ammonium Bromide Clusters. *Journal of the American Society for Mass Spectrometry*, 16(5):717–732, 2005. doi:10.1016/j.jasms.2005.01.019.

- R. C. Flagan. On Differential Mobility Analyzer Resolution. *Aerosol Science and Technology*, 30(6):556–570, 1999. ISSN 15217388. doi:10.1080/027868299304417.
- N. A. Fuchs. On the stationary charge distribution on aerosol particles in a bipolar ionic atmosphere. *Geofisica Pura e Applicata ISSN: 0367-4355*, 56:185–193, 1963. doi:10.1007/BF01993343.
- D. Gerlich. Applications of rf fields and collision dynamics in atomic mass spectrometry. *Journal of Analytical Atomic Spectrometry*, 19:581–590, 2004. ISSN 0267-9477. doi:10.1039/b404032p.
- M. Heinritzi, M. Simon, G. Steiner, A. C. Wagner, A. Kürten, A. Hansel, and J. Curtius. Characterization of the mass-dependent transmission efficiency of a CIMS. *Atmospheric Measurement Techniques*, 9(4):1449–1460, 2016. ISSN 18678548. doi:10.5194/amt-9-1449-2016.
- S. V. Hering, G. S. Lewis, S. R. Spielman, A. Eiguren-Fernandez, and N. M. Kreisberg. Detection near 1 nm with a laminar-flow, water-based condensation particle counter. *Aerosol Science and Technology*, 51(3):354–362, 2017. ISSN 0278-6826. doi:10.1080/02786826.2016.1262531.
- M. Hermann, B. Wehner, O. Bischof, H. S. Han, T. Krinke, W. Liu, A. Zerrath, and A. Wiedensohler. Particle counting efficiencies of new TSI condensation particle counters. *Journal of Aerosol Science*, 38(6):674–682, 2007. ISSN 00218502. doi:10.1016/j.jaerosci.2007.05.001.
- C. J. Hogan and J. Fernández de la Mora. Tandem ion mobility-mass spectrometry (IMS-MS) study of ion evaporation from ionic liquid-acetonitrile nanodrops. *Physical Chemistry Chemical Physics*, 11(36):8079–8090, 2009. ISSN 14639076. doi:10.1039/b916865f.
- K. Iida, M. R. Stolzenburg, and P. H. McMurry. Effect of Working Fluid on Sub-2 nm Particle Detection with a Laminar Flow Ultrafine Condensation Particle Counter. *Aerosol Science and Technology*, 43(1):81–96, 2009. doi:10.1080/02786820802488194.
- J. Jiang, M. Chen, C. Kuang, M. Attoui, and P. H. McMurry. Electrical Mobility Spectrometer Using a Diethylene Glycol Condensation Particle Counter for Measurement of Aerosol Size Distributions Down to 1 nm. *Journal of Aerosol Science*, 45(4):510–251, 2011. doi:10.1080/02786826.2010.547538.
- H. Junninen, M. Ehn, Petäjä, L. Luosujärvi, T. Kotiaho, R. Kostianen, U. Rohner, M. Gonin, K. Fuhrer, M. Kulmala, and D. R. Worsnop. A high-resolution mass spectrometer to measure atmospheric ion composition. *Atmospheric Measurement Techniques*, 3(4):1039–1053, 2010. ISSN 18671381. doi:10.5194/amt-3-1039-2010.

- J. Kangasluoma and J. Kontkanen. On the sources of uncertainty in the sub-3 nm particle concentration measurement. *Journal of Aerosol Science*, 112:34–51, 2017. ISSN 18791964. doi:10.1016/j.jaerosci.2017.07.002.
- J. Kangasluoma, H. Junninen, K. Lehtipalo, J. Mikkilä, J. Vanhanen, M. Attoui, M. Sipilä, D. R. Worsnop, M. Kulmala, and T. Petäjä. Remarks on ion generation for CPC detection efficiency studies in sub-3-nm size range. *Aerosol Science and Technology*, 47(5):556–563, 2013. ISSN 1521-7388. doi:10.1080/02786826.2013.773393.
- J. Kangasluoma, A. Samodurov, M. Attoui, A. Franchin, H. Junninen, F. Korhonen, T. Kurtén, H. Vehkamäki, M. Sipilä, K. Lehtipalo, D. R. Worsnop, T. Petäjä, and M. Kulmala. Heterogeneous Nucleation onto Ions and Neutralized Ions: Insights into Sign-Preference. *Journal of Physical Chemistry C*, 120(13):7444–7450, 2016. ISSN 19327455. doi:10.1021/acs.jpcc.6b01779.
- M. Leiminger, S. Feil, P. Mutschlechner, A. Ylisirniö, D. Gansch, L. Fischer, A. Jordan, S. Schobesberger, A. Hansel, and G. Steiner. Characterisation of the transfer of cluster ions through an Atmospheric Pressure interface Time-of-Flight mass spectrometer with hexapole ion guides. *Atmospheric Measurement Techniques*, 12:5231–5246, 2019. ISSN 1867-8610. doi:10.5194/amt-12-5231-2019.
- J. M. Mäkelä, M. Riihelä, A. Ukkonen, V. Jokinen, and J. Keskinen. Comparison of mobility equivalent diameter with Kelvin-Thomson diameter using ion mobility data. *Journal of Chemical Physics*, 105:1562–1571, 1996. ISSN 00219606. doi:10.1063/1.472017.
- T. Petäjä, G. Mordas, H. Manninen, P. P. Aalto, K. Hämeri, and M. Kulmala. Detection Efficiency of a Water-Based TSI Condensation Particle Counter 3785. *Aerosol Science and Technology*, 40:1090–1097, 2006. ISSN 15217388. doi:10.1080/02786820600979139.
- J. Rus, D. Moro, J. A. Sillero, J. Royuela, A. Casado, F. Estevez-Molinero, and J. Fernández de la Mora. IMS-MS studies based on coupling a differential mobility analyzer (DMA) to commercial API-MS systems. *International Journal of Mass Spectrometry*, 298:30–40, 2010. ISSN 13873806. doi:10.1016/j.ijms.2010.05.008.
- H. G. Scheibel and J. Porstendörfer. Generation of monodisperse Ag- and NaCl-aerosols with particle diameters between 2 and 300 nm. *Journal of Aerosol Science*, 14(2):113–126, 1983. ISSN 00218502. doi:10.1016/0021-8502(83)90035-6.
- L. A. Sgro and J. Fernández de la Mora. A Simple Turbulent Mixing CNC for Charged Particle Detection Down to 1.2 nm. *Aerosol Science and Technology*, 38:1–11, 2004. ISSN 15217388. doi:10.1080/02786820490247560.

- G. Steiner, M. Attoui, D. Wimmer, and G. P. Reischl. A medium flow, high-resolution Vienna DMA running in recirculating mode. *Aerosol Science and Technology*, 44:308–315, 2010. ISSN 02786826. doi:10.1080/02786821003636763.
- G. Steiner, A. Franchin, J. Kangasluoma, V. M. Kerminen, M. Kulmala, and T. Petäjä. Production of neutral molecular clusters by controlled neutralization of mobility standards. *Aerosol Science and Technology*, 51(8):946–955, 2017. ISSN 15217388. doi:10.1080/02786826.2017.1328103.
- M. R. Stolzenburg and P. H. McMurry. An ultrafine aerosol condensation nucleus counter. *Aerosol Science and Technology*, 14:48–65, 1991. ISSN 15217388. doi:10.1080/02786829108959470.
- C. Tauber, X. Chen, P. E. Wagner, P. M. Winkler, C. J. Hogan, and A. Maißer. Heterogeneous Nucleation onto Monoatomic Ions: Support for the Kelvin-Thomson Theory. *ChemPhysChem*, 19:3144–3149, 2018. ISSN 14397641. doi:10.1002/cphc.201800698.
- C. Tauber, S. Brilke, P. J. Wlasits, P. S. Bauer, G. Köberl, G. Steiner, and P. M. Winkler. Humidity effects on the detection of soluble and insoluble nanoparticles in butanol operated condensation particle counters. *Atmospheric Measurement Techniques*, 12:3659–3671, 2019a. doi:10.5194/amt-12-3659-2019.
- C. Tauber, G. Steiner, and P. M. Winkler. Counting efficiency determination from quantitative intercomparison between expansion and laminar flow type condensation particle counter. *Aerosol Science and Technology*, 53(3):344–354, 2019b. ISSN 15217388. doi:10.1080/02786826.2019.1568382.
- S. Ude and J. Fernández de la Mora. Molecular monodisperse mobility and mass standards from electrosprays of tetra-alkyl ammonium halides. *Journal of Aerosol Science*, 36:1224–1237, 2005. ISSN 00218502. doi:10.1016/j.jaerosci.2005.02.009.
- J. Vanhanen, J. Mikkilä, K. Lehtipalo, M. Sipilä, H. E. Manninen, E. Siivola, T. Petäjä, and M. Kulmala. Particle size magnifier for nano-CN detection. *Aerosol Science and Technology*, 45:533–542, 2011. ISSN 02786826. doi:10.1080/02786826.2010.547889.
- D. Wimmer, K. Lehtipalo, A. Franchin, J. Kangasluoma, F. Kreissl, A. Kürten, A. Kupc, A. Metzger, J. Mikkilä, T. Petäjä, F. Riccobono, J. Vanhanen, M. Kulmala, and J. Curtius. Performance of diethylene glycol-based particle counters in the sub-3nm size range. *Atmospheric Measurement Techniques*, 6:1793–1804, 2013. ISSN 18671381. doi:10.5194/amt-6-1793-2013.
- P. M. Winkler, G. Steiner, A. Vrtala, H. Vehkamäki, M. Noppel, K. E. Lehtinen, G. P. Reischl, P. E. Wagner, and M. Kulmala. Heterogeneous nucleation experiments bridging the scale

from molecular ion clusters to nanoparticles. *Science*, 319:1374–1377, 2008. ISSN 00368075. doi:10.1126/science.1149034.

W. Winklmayr, G. P. Reischl, A. Lindner, and A. Berner. A new electromobility spectrometer for the measurement of aerosol size distributions in the size range from 1 to 1000 nm. *Journal of Aerosol Science*, 22(3):289–296, 1991. doi:10.1016/S0021-8502(05)80007-2.

Chapter 3

Humidity effects on the detection of soluble and insoluble nanoparticles in butanol operated condensation particle counters

This chapter was published by C. Tauber, S. Brilke, P.J. Wlasits, P.S. Bauer, G. Köberl, G. Steiner & P.M. Winkler in *Atmospheric Measurement Techniques* **12**, 3659 - 3671; (2019)

doi: <https://doi.org/10.5194/amt-12-3659-2019>.

Abstract. In this study the impact of humidity on heterogeneous nucleation of n-butanol onto hygroscopic and nonabsorbent charged and neutral particles was investigated using a fast expansion chamber and commercial continuous flow type condensation particle counters (CPCs). More specifically, we measured the activation probability of sodium chloride (NaCl) and silver (Ag) nano-particles by using n-butanol as condensing liquid with the size analyzing nuclei counter (SANC). In addition, the cut-off diameters of regular butanol based CPCs for both seed materials under different charging states were measured and compared to SANC results. Our findings reveal a strong humidity dependence of NaCl particles in the sub-10 nm size range since the activation of sodium chloride seeds is enhanced with increasing relative humidity. In addition, negatively charged NaCl particles with a diameter below 3.5 nm reveal a charge enhanced activation. For Ag seeds this humidity and charge dependence was not observed, underlining the importance of molecular interactions between seed and vapor molecules. Consequently, the cut-off diameter of a butanol based CPC can be reduced significantly by increasing the relative humidity. This finding suggests that cut-off diameters of butanol CPCs under ambient conditions are likely smaller than corresponding cut-off diameters measured under clean (dry) laboratory conditions. At the same time, we caution that the humidity dependence may lead to wrong interpretations if the aerosol composition is not known.

3.1 Introduction

In the atmosphere nano-particle formation by gas-to-particle conversion has been observed in a variety of locations and conditions (Kulmala et al., 2004b). On a global scale, it is seen as an important source controlling the number size distribution of atmospheric aerosols (Kulmala et al., 2014). Thereby, a phase transition from the gaseous to the liquid or solid state occurs in the presence of supersaturated vapors. This process of nucleation arises homogeneously from gas molecules only, or heterogeneously by the formation of vapor clusters on preexisting particles (Ferreiro et al., 2016; Kangasluoma et al., 2016; Strey et al., 1986; Tauber et al., 2018; Winkler et al., 2008b). These nano-particles then can grow up to a size at which they act as cloud condensation nuclei (CCN) (Merikanto et al., 2009; Spracklen et al., 2008). Thereby nanometer-sized particles contribute to the indirect radiative forcing, thus influencing the Earth's climate (Boucher et al., 2013).

Heterogeneous nucleation in the atmosphere takes place for seed particles and vapor molecules of different chemical composition. Aerosol particles acting as seeds in the heterogeneous nucleation process have different physicochemical surface properties such as charging state, wettability, shape or size. Interactions between the seed and the vapor molecules as well as solubility play an important role (Kupc et al., 2013; McGraw et al., 2012, 2017). Atmospheric aerosol can contain hygroscopic salts and is therefore sensitive to relative humidity which can contribute to a phase transition within the aerosol particle.

A highly hygroscopic and well characterized example is sodium chloride (NaCl) which mainly originates from sea spray (Biskos et al., 2006; Clarke et al., 2003; Krämer et al., 2000; Lawler et al., 2014; Zieger et al., 2017). Water vapor strongly influences the phase of the hygroscopic NaCl particles which under dry conditions exhibit a solid crystalline structure. At high relative humidity (RH), salt particles take up water and form saline droplets with increased volume which affects their physical, chemical and optical properties. In contrast to increasing RH, aqueous saline aerosol particles shrink with decreasing relative humidity. Thereby the water evaporates and the seed crystallizes (Biskos et al., 2006; Martin, 2000).

In a recently published paper by Tauber et al. (2018), it has been shown that the presence of monoatomic ions significantly lowers the energy barrier for the heterogeneous nucleation of n-butanol compared to neutral seeds. It is known from previous studies that ion induced nucleation is highly affected by the chemical structure of the condensing vapor and seed ion properties like charge state (Iida et al., 2009; Kangasluoma et al., 2016). This process comes into play especially in the sub-3 nm size range at which condensation-based nanoparticle detection methods have their lower detection limit. Thereby the initial charge state of aerosol particles with diameters within this size range can influence the detection efficiency.

In the atmosphere usually more than a single species of vapor molecules contributes to the vapor-liquid nucleation. Both processes, gas-to-particle conversion and the existence of insoluble particles in the atmosphere, can initiate heterogeneous nucleation processes (Kuang et al., 2010, 2012; Kulmala et al., 2004a; McMurry et al., 2005; Wang et al., 2013). A commonly used technique to measure preexisting particles in the atmosphere is condensation particle counting, which often use n-butanol as working fluid (McMurry, 2000). However, under ambient conditions significant amounts of water vapor usually enter the condensation particle counter (CPC) and can modify its detection behavior. Previous studies on binary heterogeneous nucleation of n-propanol-water vapor mixtures on sodium chloride (NaCl) particles indicated a decrease of the activation barrier in accordance with the theory of binary heterogeneous nucleation and reported a soluble-insoluble transition in the particle activation behavior (Petersen et al., 2001). Butanol is chemically similar to propanol and commonly used as working fluid in CPCs. Therefore the process of heterogeneous nucleation of n-butanol and water vapor on nanometer sized particles is of high relevance in ambient nanoparticle characterization studies. In addition, pulse height analysis conducted by Hanson et al. (2002) for sulfuric acid particles revealed a strong dependence of the particle counter's response on chemical composition and water vapor. The size resolved chemical composition measurements of nanoparticles from reactions of sulfuric acid with ammonia and dimethylamine, investigated by Chen et al. (2018), suggest that small, acidic and newly formed particles can affect the physicochemical properties during the cluster formation process and thereby enhance early particle growth. This indicates a chemical cluster composition and working fluid dependent activation behavior at the lower detection limit of the used CPC.

Over the last years various studies investigated the onset saturation ratio and the nucleation temperature for different seeds and vapors. These studies include measurements by Chen and Tao (2000) for water on SiO₂ and TiO₂, and Schobesberger et al. (2010) for n-propanol on silver (Ag) and sodium chloride seeds. All studies show that the expected temperature trend agrees with theory, except for the nucleation of n-propanol on NaCl particles. In this specific case an opposite temperature trend of the onset saturation ratio compared to the Kelvin equation in the temperature range from 262 K to 287 K was recorded (Schobesberger et al., 2010).

Despite the common use of butanol as working fluid for the detection of ambient nanoparticles, comparatively little research on the fundamental aspects of butanol nucleation has been done in the sub-10 nm size range, e.g. Barmounis et al. (2018) and Sem (2002). For DEG based CPCs Iida et al. (2009) and Kangasluoma et al. (2013) investigated the temperature and humidity dependence of the working fluid on the particle activation. Here, we investigate heterogeneous nucleation of n-butanol vapor on differently sized seeds in the sub-10 nm diameter range depending on relative humidity, charge state and nucleation temperature. We

aim at getting a better understanding of the effect of RH and initial charging states on the nucleation process in CPCs with the focus on sub-5 nanometer particles. Thereby the relative humidity effect and charge dependence on the lower particle detection limit can be analyzed. The results help to improve the understanding of heterogeneous nucleation of n-butanol vapor on soluble and insoluble seeds. By that the acting mechanism during the nucleation process can be analyzed and used to explain changes of the counting efficiencies in commercial CPCs (Ankilov et al., 2002).

3.2 Experimental Section

We examined the nucleation probability and counting efficiency of n-butanol based CPCs as shown schematically in Figure 3.1 and Figure S1 in the supporting information. Ag and NaCl particles were generated in a tube furnace (Scheibel and Porstendörfer, 1983) which was supplied with synthetic air (ALPHAGAZ 1 AIR, $\geq 99.999\%$ (5.0), Air Liquide) or particle-free dry compressed air. The flow carrying the polydisperse aerosol was kept constant at 3 L/min through the Americium 241 (Am-241) charger and the nano differential mobility analyzer (nDMA) for both experimental approaches. By applying positive or negative voltage to the nDMA a monodisperse negatively or positively charged particle fraction was selected. By placing an Am-241 charger either at the Size Analyzing Nuclei Counter (SANC) or the CPC inlet the size selected particles were neutralized. Subsequently, ions that form inside the charger were removed using a home-built ion precipitator (ion trap). By applying a voltage of $\pm 500\text{V}$ to a tubing which is cut in two half pipes and separated by a non conductive material all charger ions were removed. An adjustable well-defined flow of humid air joined the aerosol flow after the nDMA in order to vary the humidity before the CPC inlet flow. Accordingly, the carrier gas was humidified by passing it through a diffusion type humidifier (see Figure 3.1). The relative humidity of the carrier gas was monitored and recorded throughout every measurement. The recorded RH values were stable within $\pm 1\%$ which is below the sensor accuracy. Two humidity sensors (HIH-4000-004, Honeywell) monitored the humidity of the aerosol flow before and after the injection of the humid flow. The amount of water vapor during the counting efficiency measurements was kept constant. Diffusional particle losses were kept to a minimum by keeping tubing as short as possible. In every measurement sequence, particle tubing to CPC and FCE was kept to the same length. In addition, the flow rates were kept constant and the flow was symmetrically split. The additional particle losses for the neutral experiments were calculated following Tauber et al. (2019b).

Measurements of heterogeneous nucleation of n-butanol at nucleation temperatures ranging from 270 K to 292 K were carried out with the SANC (Wagner et al., 2003). To this end, monodisperse particle fractions were mixed with a carrier gas flow of 5 L/min containing

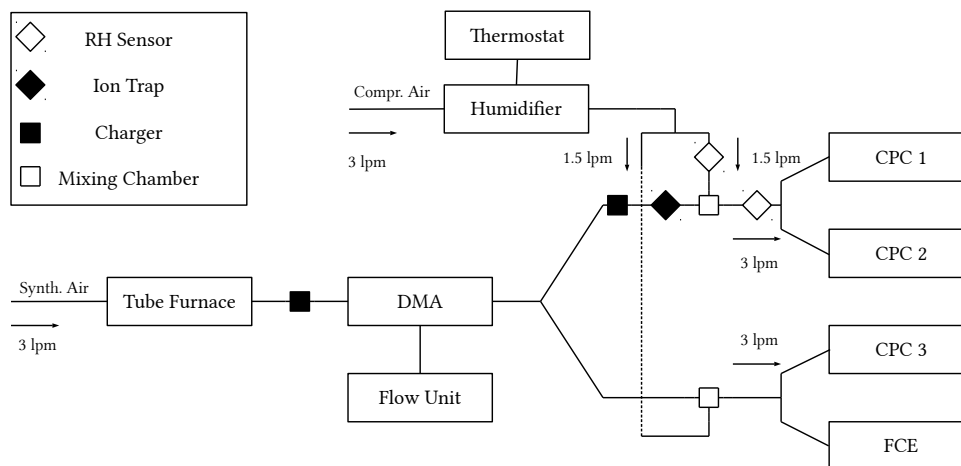


Figure 3.1. The experimental setup for evaluating the relative humidity dependent counting efficiency of continuous flow type CPCs (TSI 3776 UCPC), which was measured relative to a Faraday Cup Electrometer (FCE) (Wlasits, 2019).

n-butanol vapor and led into the expansion chamber of the SANC. N-butanol vapor was added to the system by controlled injection using a syringe pump, followed by quantitative evaporation of the liquid beam in a heating unit (Winkler et al., 2008a). As a result, the well-defined and nearly saturated binary vapor-air mixture together with size selected, neutralized monodisperse seed particles from the nDMA was passed into the temperature controlled expansion chamber. Vapor supersaturation was achieved by adiabatic expansion, and the number concentration of droplets nucleating on the seeds was measured with the Constant Angle Mie Scattering (CAMS) method (Wagner, 1985). Based on the CAMS-method a one to one correlation between the time dependent measured scattered light flux under a constant angle and the calculated scattered light flux as a function of droplet size can be established. Thus, the radius and the number concentration of the growing droplets could be determined simultaneously. This allows us to determine the growth curve of the growing droplets which can be compared to theoretical calculations from a condensation model. Thereby, the saturation ratio can be verified with an accuracy of 2-3 percent. By varying the chamber temperature and the pressure drop in the expansion chamber, different nucleation conditions were analyzed. The nucleation or activation probabilities were measured with the SANC/CAMS method (Wagner et al., 2003). To evaluate the onset saturation ratio, which corresponds to a nucleation probability value of $P = 0.5$, the experimental data were fitted with a two-parameter fit function (Winkler et al., 2016).

In addition to the SANC measurements, the counting efficiencies of three ultrafine continuous flow type CPCs (Model UCPC 3776, TSI Inc., Minneapolis, USA), which temperature settings

Table 3.1. Temperature settings of the three TSI 3776 UCPCs used in this study in parallel.

settings	low T [°C]	standard T [°C]	high T [°C]
condenser	1.1	10.0	18.9
saturator	30.1	39.0	47.9
optics	31.1	40.0	48.9

were changed over a range of 18 degrees, were measured. In contrast to the SANC, the supersaturation is obtained by saturating a laminar flow and subsequently cooling the aerosol together with the saturated flow in the condenser. Both methods lead to heterogeneous nucleation and condensation of n-butanol vapor on the aerosol particles due to a temperature reduction. Thereby the particles grow to a size at which they can be detected optically. To measure the detection efficiency of the TSI UCPCs, the aerosol flow subsequent to size classification was symmetrically split. The aerosol was passed to three CPCs ($N_{CPC,1-3}$), each operating at different temperature settings (see Table 3.1), and to the Faraday Cup Electrometer (FCE) (N_{FCE}), which was operated in parallel. Thereby the counting efficiency was determined relative to a FCE (Model 3068B Aerosol Electrometer, TSI Inc., Minneapolis, USA). The detection efficiency η of a UCPC can be determined by comparing the number concentration of the CPC $N_{CPC,1-3}$ and the total number concentration N_{FCE} according to the following relation:

$$\eta = \frac{N_{CPC,1-3}}{N_{FCE}}. \quad (3.1)$$

In order to calculate the counting efficiency of the neutralized aerosol, we evaluated the charging efficiency and the theoretical penetration efficiency for the FCE and CPC to correct for the neutralization and penetration losses following Tauber et al. (2019a). By operating the CPCs at different temperature settings we were able to analyze simultaneously the detection efficiency with varying peak super saturation ratios (Tauber et al., 2019a). The particle detection efficiency mainly depends on the activation probability, which is primarily a function of supersaturation and particle diameter (Barmounis et al., 2018). By conducting detection efficiency measurements the cut-off diameter is determined. The cut-off diameter corresponds to the mobility diameter at which 50% of the particles are counted in a CPC.

3.3 Results and Discussion

3.3.1 Temperature and Humidity Effects

In this chapter we discuss the measurements of the onset saturation ratio of n-butanol depending on nucleation temperature and humidity with the SANC. The heterogeneous nucleation probability (P) for different seeds and seed properties in the size range of 2.5 to 10.5 nm mobility diameter was investigated. The heterogeneous nucleation probability represents the number concentration of activated seeds normalized to the total number concentration of the aerosol. It depends on the saturation ratio which is given by the ratio of partial vapor pressure divided by the equilibrium vapor pressure at the corresponding temperature after expansion (nucleation temperature T_{nuc}). Measurements were conducted at constant T_{nuc} by varying the vapor amount and keeping the pressure drop constant. In a recent study we have shown that with reduced nucleation temperatures the onset saturation ratio needed to activate a certain Ag particle size increases (Tauber et al., 2019a). This is in line with classic Kelvin predictions (Thomson, 1871), where with decreasing temperature the required equilibrium saturation ratio increases. This behaviour agrees with homogeneous nucleation. To investigate the impact of RH on heterogeneous nucleation probability the Ag measurements were complemented by NaCl seeds. The resulting onset saturation ratios depending on the nucleation temperatures are shown in Figure 3.2. Clearly, the required saturation ratio to activate a certain particle size is always lower for Ag particles compared to NaCl particles. Heterogeneous nucleation of n-butanol vapor on NaCl and Ag aerosol particles shows a remarkably different behavior. An opposite temperature trend for NaCl seeds was identified when compared to the Kelvin prediction, except for the smallest sodium chloride particles with a mobility diameter of 2.5 nm. Such a trend was not found for silver nano-particles.

This finding is consistent with already published results from Schobesberger et al. (2010) for n-propanol, where an opposite temperature trend for NaCl but not for Ag seeds could be observed. To rule out any humidity effects, the sheath air of the nDMA was monitored using a commercial relative humidity sensor during the measurements. Thereby an accumulation of water in the used silica gel dryer of the sheath air loop could be recorded. The water aggregation in the dryer, originating from the compressed air supply, reached values up to 10% RH at 22°C room temperature. As a consequence, the carrier gas supplement for the experiment was changed from dried and filtered compressed air to synthetic air. Additional measurements were performed with a relative humidity < 3.5% at room temperature.

In Figure 3.3 the experimental values for neutral sodium chloride seeds are shown and listed in Tables S5-S9 of the supporting information for both considered aerosol species. The necessary onset saturation ratio for activating "dry particles" of a certain size is at the same value as

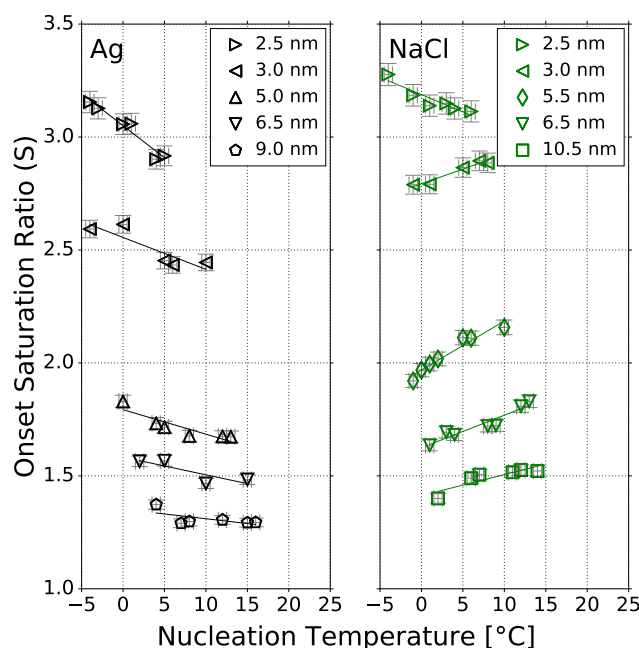


Figure 3.2. The onset saturation ratio versus nucleation temperature for neutral Ag (black) and NaCl (green) particles of different mobility equivalent diameters. With decreasing temperature the onset saturation ratio decreases for sodium chloride and increases for silver nanometer sized particles. Only the 2.5 nm NaCl seeds do not follow the opposite temperature trend. Lines represent a linear fit of data to show the temperature dependence for NaCl and Ag seeds. The onset saturation ratio increases with decreasing seed size for both test aerosols.

for "high" RH values ($< 10\%$) or (with one exception) increased for dry measurements (RH $< 3.5\%$). In other words, the additional small amount of water vapor during the measurements decreases the energy barrier which has to be overcome to activate a sodium chloride nanoparticle with n-butanol in the observed size range. This finding suggests that even small contamination of water vapor can influence the heterogeneous nucleation of butanol, a finding that agrees with already published studies for n-propanol-water mixtures on Ag and NaCl particles (Wagner et al., 2003).

For the heterogeneous nucleation of n-butanol on silver seeds no decrease of the onset saturation ratio due to the presence of water was observed. The opposite temperature dependence for NaCl and synthetic air as carrier gas (blue symbols in Figure 3.3) vanishes for small mobility diameters (< 3.5 nm), but particle sizes above 3.5 nm still follow the unusual temperature dependence. This indicates that sodium chloride particles act differently in the observed size range. It seems that NaCl seeds at sizes below ~ 3.5 nm are less prone to dissolution or restructuring effects. As a result, the nucleation of n-butanol on small NaCl seeds is comparable to silver clusters. The opposite temperature trend vanishes and follows the Kelvin relation. Another remaining question is: Does the charge sign have an effect on heterogeneous nucle-

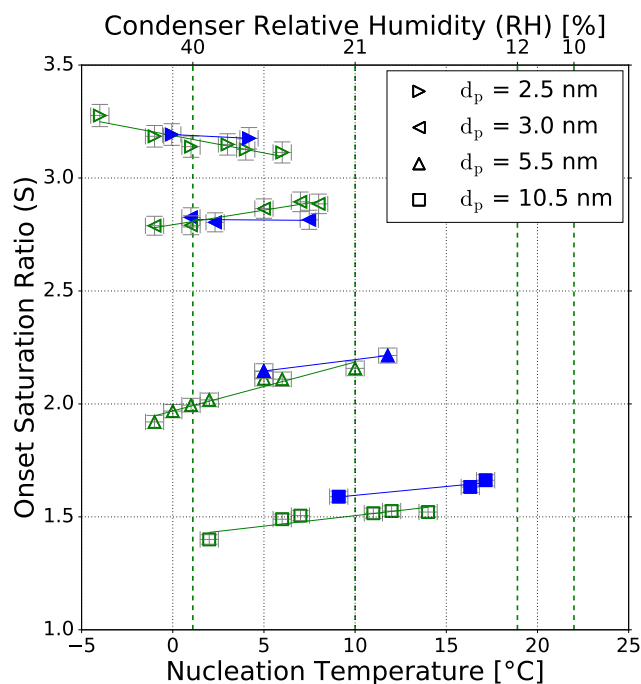


Figure 3.3. The onset saturation ratio versus nucleation temperature for NaCl particles of different mobility equivalent diameters. The green symbols show the onset saturation values recorded with relative humidity values $\leq 10\%$ and the blue symbols represent measurement values when the RH was $< 3.5\%$. The green dashed vertical lines represent the calculated relative humidity at the corresponding preset condenser temperature (see Table 3.1) with a starting value of 10% RH at 22°C. The increased relative humidity inside the condenser of a TSI 3776 UCPC for reduced nucleation temperatures is shown and will be discussed in the counting efficiency measurements section.

ation? To answer this question, additional measurements focusing on charge and humidity for NaCl particles in the corresponding nanometer range were conducted.

3.3.2 The Influence of Charge and Particle Restructuring Effects

To investigate the charge effect on heterogeneous nucleation of n-butanol vapor on silver and sodium chloride particles the neutralizer and ion-trap in front of the expansion chamber (see Figure S1) were removed. Thereby the seeds were positively or negatively charged, depending on the applied voltage to the nDMA. Nucleation studies were conducted with constant nucleation temperatures but varying charge state of the aerosol using synthetic air as carrier gas. For positively charged silver particles no charge dependence on heterogeneous nucleation was found. However, NaCl seeds show a charge dependence, especially below 5 nm. As listed in Table 3.2 the necessary onset saturation ratio for neutral and positively charged silver particles is below the NaCl values, and no charge enhancement was found. Negatively charged Ag particles could not be fully investigated due to technical problems

Table 3.2. SANC experimental results for the onset saturation ratio for neutral (n), positively (+) and negatively (-) charged particles. D_p is the mean mobility equivalent diameter, σ_g the mean geometric standard deviation and S_{onset} the onset saturation ratio.

		Ag ($RH < 2.5\%$)			NaCl ($RH < 2.5\%$)		
		S_{onset}	S_{onset}	S_{onset}	S_{onset}	S_{onset}	S_{onset}
D_p [nm]	σ_g	n	+	-	n	+	-
2.5	1.073	3.10	3.07	-	3.19	3.20	3.04
3.0	1.070	2.48	2.48	-	2.81	2.72	2.64
3.5	1.067	2.33	2.33	-	2.60	2.54	2.47
5.5	1.065	1.85	1.85	1.83	2.21	-	2.20
9.0	1.068	1.34	1.36	-	-	-	-
10.5	1.067	-	-	-	1.64	1.66	1.63

with the SANC at the end of the measurement run. Kangasluoma et al. (2016) conducted measurements using tungsten oxide, ammonium sulfate and tetraheptylammonium bromide nano clusters of different charge states to determine the counting efficiency. During their studies a charge enhanced particle activation was observed similar to our findings regarding the NaCl measurements.

It is known from prior research that NaCl aerosol particles, which are generated by evaporation and condensation in a tube furnace, undergo a structural change in the presence of water (Biskos et al., 2006; Krämer et al., 2000) or n-propanol (Kulmala et al., 2001; Petersen et al., 2001). As a consequence, the particles shrink in the presence of polar vapors. In order to test a humidity induced change in particle size, we used a standard DMPS setup, which has a filtered and dried (using Silica gel) sheath air loop. The corresponding setup schema can be found in the supporting information (Figure S3). Our results confirmed the measurements conducted by Biskos et al. (2006), showing the shrinkage of sodium chloride particles in the presence of water vapor. This shrinkage was also investigated in our study for n-butanol. The experimental results for water are shown in Figure 3.4. We measured monodisperse NaCl aerosols with mobility diameters between 4.5 and 11 nm at relative humidities up to 50%. The shrinkage measurements in Figure 3.4 were conducted with SHT75 sensors, with an accuracy of $\pm 1.8\%$ RH and with a HMI38 Humidity Data Processor with a HMP35E probe, with an accuracy of $\pm 2.0\%$ RH. However, with decreasing mobility diameter, also

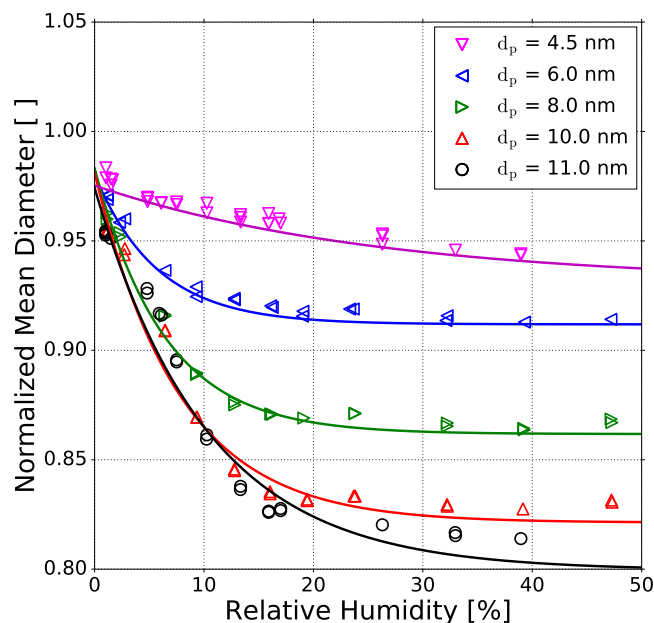


Figure 3.4. Normalized mean diameter of sodium chloride particles as a function of relative humidity which represents the shrinkage of NaCl seeds in the presence of water vapor. All sizes are mobility equivalent diameters. Each line represents a tentative three-parameter fit of an exponential decay. The measurements were conducted with SHT75 sensors with an accuracy of $\pm 1.8\%$ RH and with a HMP35E probe with an accuracy of $\pm 2.0\%$ RH.

the shrinkage becomes less. For example, an 11 nm NaCl particle exposed to 40% RH is shrinking by about 15%. A 4.5 nm particle at 40% RH shrinks only by about 3%. Hence, the structural rearrangement of particles below 5 nm is not as pronounced as for larger ones. This decrease in size for particles > 5 nm is a result of solvation on the surface of the NaCl particle caused by the presence of water vapor. Thereby a wet surface accrues (Castarède and Thomson, 2018). Due to this dissociation process and the resulting liquid surface the particle attracts more polar vapor molecules. In addition, the overall polarity of the working fluid of n-butanol and water mixture increases, due to the higher dipole moment of water (6.2×10^{-30} Cm) compared to n-butanol (5.8×10^{-30} Cm) (Reichardt and Welton, 2010). As a result, additional vapor molecules can more readily condense onto the seed aerosol. This mechanism could explain the resulting lower onset saturation ratio needed for NaCl seeds ≥ 3 nm as shown in Figure 3.3 for lower nucleation temperatures. Consequently, by reducing the nucleation temperature the saturation vapor pressure decreases, leading to an increase in the saturation ratio for water (RH is increasing, see Figure 3.3, upper x-axis).

In summary, the SANC measurements allowed us to study the heterogeneous nucleation of n-butanol depending on the charge state, nucleation temperature and humidity of the carrier gas. Charge enhanced nucleation could be found for sodium chloride particles ≤ 3.5 nm. By

Table 3.3. Calculated maxima of the CPC saturation ratio profiles S_{max} for low, standard and high temperature settings (Tauber et al., 2019a), in comparison to the extrapolated S_{onset} as measured by the SANC.

d_p [nm]		NaCl neutral ($RH < 3.5\%$)				NaCl neutral ($RH < 10.0\%$)			
		2.5	3.0	3.5	5.5	2.5	3.0	3.5	5.5
T settings	S_{max}	S_{onset}	S_{onset}	S_{onset}	S_{onset}	S_{onset}	S_{onset}	S_{onset}	S_{onset}
low	4.3	3.18	2.81	2.65	2.10	3.17	2.80	-	1.99
standard	3.4	3.15	2.81	2.57	2.20	3.03	2.92	-	2.18
high	2.8	3.11	2.80	2.50	2.28	2.90	3.03	-	2.37

taking special care of the water vapor amount a humidity enhanced nucleation for sodium chloride seeds was found. Under dry conditions the observed opposite temperature trend for NaCl seeds < 3.5 nm vanishes. For larger sodium chloride particles this trend is found to be persistent.

3.3.3 Counting Efficiency Measurements

Complementing the SANC measurements we have performed counting efficiency measurements at different condenser temperatures, but constant ΔT between saturator and condenser for a commercial n-butanol TSI 3776 UCPC. Thereby, we were able to increase or decrease the saturation ratio profile as described by Tauber et al. (2019a). The onset saturation ratio and nucleation temperature measured with the SANC for a classified monodisperse seed particle size could be compared to the three different temperature settings of the condenser. The maximum value for the calculated saturation ratio profiles and the extrapolated S_{onset} for NaCl (partly extrapolated from the lines in Figure 3.2 and 3.3) under different humidity conditions at low, standard and high condenser temperatures are listed in Table 3.3. Thus, the ability to activate sodium chloride seeds in the cut-off range of a commercial UCPC could be analyzed. With increasing temperature the maximum saturation ratio (S) decreases. As a result, the detection efficiency is shifting to larger particle sizes.

For the verification of our findings we measured the cut-off diameter, charge and relative humidity dependence for the TSI 3776 UCPC at different temperature settings. By varying the temperature settings of the UCPC we were also able to measure under different condenser (nucleation) temperatures (see Table 3.1). For comparison, particle classification with the nDMA was always performed under dry conditions ($RH < 3.5\%$), so that the structural change

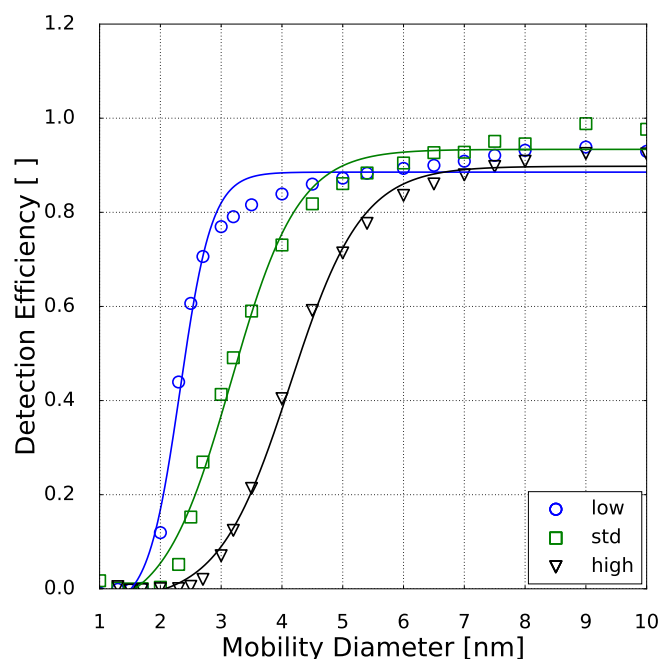


Figure 3.5. Detection efficiency as a function of mobility diameter for neutral sodium chloride particles. The symbols represent the measured counting efficiencies for low (circles), standard (std, squares) and high temperature (triangles) settings at 10% RH at room temperature of the inlet line. The line displays a fit to the measured counting efficiencies (Wiedensohler et al., 1997). Thereby the corresponding cut-off diameter with the detection efficiency of 0.5 can be evaluated.

of the sodium chloride clusters resulting from water vapor are kept to a minimum. Subsequent to the size selection, the particles were mixed with humidified air to reach RH values ranging from 0 to 40% as shown in Figure 3.1. Hence, we were able to vary the relative humidity with an accuracy of $\pm 3.5\%$ by measuring the humidity before and after the mixing zone. In total, about 400 detection efficiency curves were recorded. To rule out any dependence of the individual activation behavior of different CPCs, measurements involving one single CPC set to all three temperature settings one after another, and measurements involving three CPCs that were all set to one specific setting, have been performed. Based on these measurements, the maximum error of the cut-off diameter linked to the individual activation behavior was calculated to be at the highest at 8.1%. Results of earlier studies indicate a discrepancy of the humidity dependence for sodium chloride and silver nano-particles on the detection efficiency of commercial CPCs (Sem, 2002). In the study conducted by Sem (2002), at increased RH the used CPCs had a lower cut-off diameter above 5 nm. In this size range the particle shrinkage plays an important role: The already mentioned emerging liquid surface would attract further vapor molecules. Consequently, the NaCl particles can be easier activated than an insoluble seed.

However, in this study a TSI 3776 UCPC was used, which has a cut-off diameter well below

5 nm. An exemplary detection efficiency measurement for the three CPC temperature settings is depicted in Figure 3.5. These measurements were conducted under elevated humidity conditions (RH = 10% at room temperature), which lead to a decrease compared to dry conditions (RH = 3.5%) of the necessary onset saturation ratio for neutral NaCl seeds as shown in Figure 3.3. Due to the temperature decrease in the condenser, the saturation ratio for water vapor increases up to $S = 1.6$ with an inlet RH of 40% at room temperature. Studies conducted by Petersen et al. (2001) on binary heterogeneous nucleation of water-n-propanol vapor mixtures onto NaCl seeds also show that small amounts of water reduce the propanol activity substantially. Butanol is hardly miscible with water in macroscopic mixtures, but still small amounts support the nucleation. The resulting cut-off diameters for neutral, negatively and positively charged sodium chloride nano-particles are shown in Figure 3.6. It can be clearly seen that with increasing relative humidity the cut-off diameter is decreasing for a UCPC operating at standard conditions (green) from about 3.7 to about 2.0 nm for neutral NaCl clusters. To investigate a possible effect of the charge history of neutral particles, positively and negatively charged particles were neutralized. An effect from charge history could possibly be that previously positively charged particles differ from those that were negatively charged prior to neutralization, e.g. by their original properties or because of a change of properties during the neutralization process (Alonso and Alguacil, 2008; Kangasluoma et al., 2013). The resulting cut-off diameters are shown in Figure 3.6 (left). Regarding the charge history, no difference in activation could be found for sodium chloride. Only under high n-butanol saturation ratios (low temperature settings) and high relative humidity conditions the previously negatively charged particles exhibit a lower cut-off diameter. In Figure 3.6 (right panel), the cut-off diameters as a function of RH are shown for particles of different polarity. Remarkably, for charged NaCl particles we find increased cut-off diameters compared to the neutral particles. Since the flow carrying monodisperse aerosols and the flow of humid air are joined together in front of the CPC inlet, the increase of cut-off diameters could be a result of the increased attraction of water molecules to charged NaCl particles under sub-saturated conditions. Thereby the Na^+ and Cl^- ions get separated and form a solvent cage around themselves (Castarède and Thomson, 2018). This solvent cage reduces the tendency of ions to aggregate (Loudon, 2009).

Li and Hogan (2017) performed measurements on the uptake of organic vapor molecules by nanometer scaled sodium chloride cluster ions, using a DMA coupled to a Time-of-Flight (TOF) mass spectrometer. The results show that the polarity and the molecular structure of the vapor molecules control the vapor uptake. This is in agreement with our findings: Increasing amounts of water molecules are mixed with already preexisting butanol molecules. As a result, the overall bulk polarity of the working fluid increases and the activation of sodium chloride clusters is improved. In contrast to the SANC measurements, no significant sign preference for charge enhanced nucleation could be found. This is probably due to the

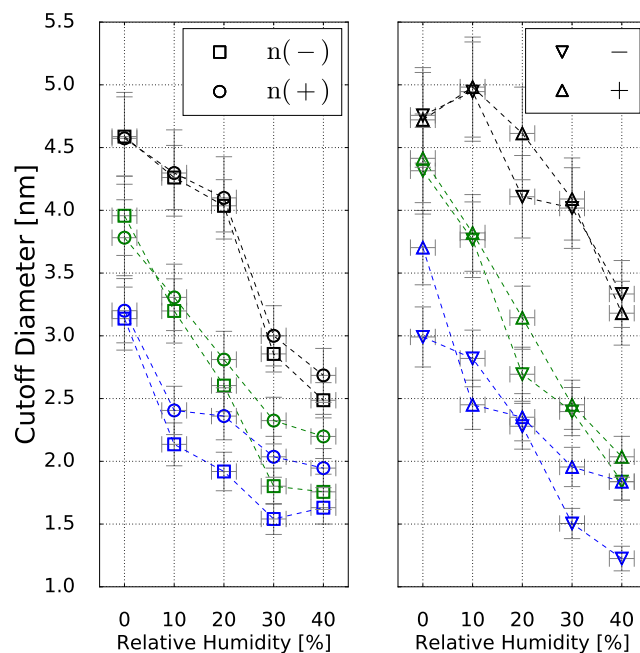


Figure 3.6. Cut-off diameter as a function of RH for neutral (left) and charged (right) sodium chloride seeds for low (blue), standard (green) and high (black) temperature settings.

cut-off diameter size which is for most of the counters > 3 nm. Except for negatively charged NaCl particles, which show a charge enhancement as it was observed with the SANC for particles < 3 nm mobility diameter. In addition, the recorded cut-off diameter for high T settings is in the size range, where the opposite temperature trend was recorded by the SANC measurements. Consequently, by decreasing the temperature the needed saturation ratio to activate a NaCl particle in this size range is decreasing. Furthermore, the increasing RH supports the structural rearrangement which reduces the cut-off diameter (see Figure 3.6) compared to dry conditions. As stated in Castarède and Thomson (2018), the solvation of sodium chloride clusters leads to an electrical potential. In this study, we show that nucleation of n-butanol vapor onto soluble NaCl below 3.5 nm is enhanced. This effect takes place as the aerosol is exposed to RH, i.e. before the sample enters the CPC. Subsequently, inside the CPC, the RH increases due to the temperature reduction inside the condenser which will have an effect on the charge enhancement. As a matter of fact, our results lead to an improved detection efficiency for sodium chloride clusters. At high relative humidity and low temperature settings the detection efficiency is further promoted by charge enhanced nucleation.

Results on the cut-off diameter depending on the relative humidity at the UCPC inlet for neutralized and charged silver seeds are shown in Figure 3.7. For Ag particles no shrinkage in mobility diameter could be measured, and the clusters at a certain size can be assumed to be

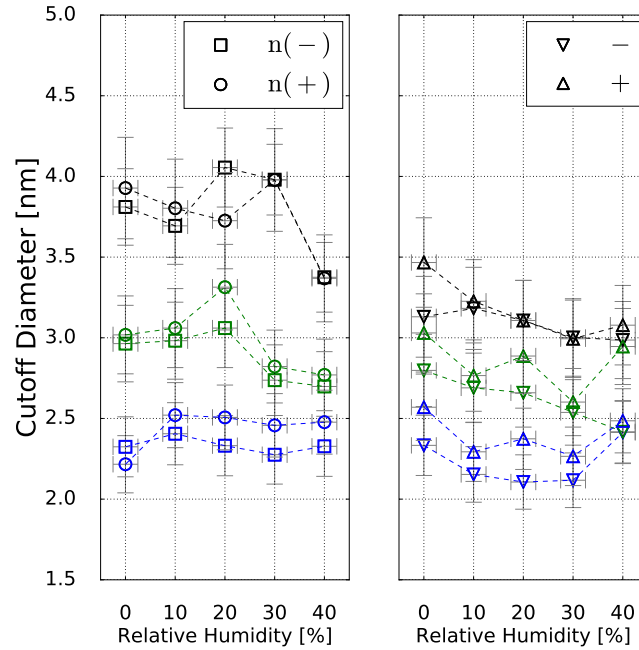


Figure 3.7. Cut-off diameter as a function of RH for neutral (left) and charged (right) Ag seeds for low (blue), standard (green) and high (black) temperature settings.

spherical (Winkler et al., 2016). As we can see in Figure 3.7, no relative humidity dependence on the cut-off diameter within the uncertainty range was observed.

However, for charged particles we see slightly reduced cut-off diameters compared to neutral particles indicating charge enhanced nucleation. While this finding is in line with previous work (Winkler et al., 2008b), the significant difference between neutral and charged particles especially at the higher temperature settings is likely a consequence of insufficient maximum saturation ratio to activate neutral particles of the same size. The calculated value of S_{max} at high temperature settings of 2.8 (see Table 3.3) would be sufficient to activate particles of approx. 2.8 nm according to the SANC measurements (Table 3.2 and Figure 3.2). It should be noted though that in the CPC the region of S_{max} is limited to the center line and most particles travelling outside this region will experience lower saturation ratios resulting in increased cut-off diameters. Overall, the charge enhancement seems to be weak both in the SANC measurements and the CPC settings. Only at the lowest temperature settings a sign-preference becomes visible favouring the activation of negatively charged particles. As expected, this sign-preference vanishes for higher temperature settings (lower saturation ratios) which is in agreement with Winkler et al. (2008b).

In general, particle counting at the detection limit of ultra-fine condensation particle counters has to be treated with care. The lowest detectable particle size, i.e. the cut-off diameter of

a CPC, is among the largest sources of inaccuracy in the sub-10 nm particle concentration measurement (Kangasluoma et al., 2018). Given that, not only seeds of different chemical compositions but also different particle solubilities are present in the atmosphere – these uncertainties in the determination of the number concentration need to be considered. A straightforward approach to assess the uncertainty of a humid sample flow is to dry the inlet flow of a CPC by e.g. using a Silica gel dryer or Nafion dryer, which is a common method for ambient measurements. Additionally, the inlet RH should be monitored and kept below a threshold value in order to narrow down the uncertainty from the humidity dependent change of the cut-off curve in the case of a soluble seed. In the ideal case, measuring instruments are calibrated up to the maximum RH that they are exposed to.

Hygroscopicity measurements of particles in the targeted size range further improve the assessment on the uncertainty of the number concentration. The location of the measurement site is also a clear indicator of a possible enhanced contribution of hygroscopic seed particles, i.e. when the measurement site is located close to the coastline. Thereby the accuracy of the data interpretation would increase. Even without these additional measurements, the location of the measurement site and the source region of the seed particles can be used for data interpretation. As a result, studies that consider sea spray as a particle source should consider the effect of humidity on the particle detection efficiency. Furthermore, studies that investigate aerosol from sources that involve soluble seeds, should consider the effect of humidity on the particle detection efficiency. Soluble seeds do not only include sodium chloride particles which were analyzed in this study. Ammonium sulfate, which originates from the gas-phase from precursor gases having both natural and anthropogenic origin (Sakurai et al., 2005; Smith et al., 2004), can act as soluble seed. Consequently, we suggest to consider a possible shift in cut-off diameter when such soluble species are present in the sample.

Based on solubility effects and the increased polarity of the working fluid due to the addition of water molecules, similar effects using different working fluids can be assessed by interpreting their chemistry. Diethylene glycol (DEG) is a well polarized molecule due to three oxygen atoms per DEG molecule. Adding water does not increase the overall polarity as much as in the case of butanol. NaCl particles are soluble in DEG as well. As presented in Kangasluoma et al. (2013) variation of the inlet flow RH leads to increased detection efficiency for a turbulent mixing type CPC.

Working fluids like perfluorcarbonates (Fluorinert, FC-43) consist of carbon chains with fluorine atoms instead of hydrogen atoms. These molecules have a low dipole moment. Due to the spherical structure and highly electronegative atoms on the outside the overall surface of the molecule is slightly negatively polarized. Consequently, a shift in the cut-off diameter can be expected by using a mixture of perfluorcarbonates and water. The overall polarity of the working fluid would almost exclusively be based on the dipole moment of water molecules.

Pulse height analysis measurements by Hanson et al. (2002), revealed a pronounced substance dependency and a difference in peak distribution when using n-butanol or FC-43 as working fluid in a CPC. The interaction between NaCl seed and water molecule remains regardless of the working fluid. If RH cannot be kept at 0%, the instrument should be calibrated to the corresponding conditions and a possible change in cut-off diameter be considered in the data analysis to ensure high data quality. Especially at measurement sites located near the sea or at changing/high RH, which is the case for most regions.

3.4 Conclusion

The presented measurements conducted with expansion and continuous flow type CPCs have shown that sodium chloride particles with a mobility diameter below 10 nm indicate different activation regimes. According to the SANC measurements, the required saturation ratio to activate a certain particle size is always lower for Ag particles compared to NaCl particles. As a consequence, the cut-off diameters measured for NaCl particles under dry conditions are always higher than for Ag seeds in butanol-based CPCs. Under dry conditions for particles ≤ 3 nm no opposite temperature trend compared to classical Kelvin predictions was observed. However, for negatively charged NaCl seeds a charge enhanced activation was measured with the SANC. Above 3.5 nm the charge does not play a role during the nucleation process. Charge enhanced particle activation did only occur at the lowest CPC temperature settings. We conclude that the activation of NaCl particles can be enhanced by increased humidity. For Ag this humidity dependence could not be observed. This is an indicator for the importance of molecular interactions between seed and vapor molecules.

A recently published study on heterogeneous nucleation of n-butanol on monoatomic ions has shown that the initial formation of a critical cluster does not favor one of the two possible polarities of the seed particle (Tauber et al., 2018). However, under sub-saturated conditions the existence of seed particle charge plays an important role concerning vapor uptake. Hence the vapor molecules are in contact with the NaCl particles under sub-saturated conditions before the temperature drops and can attach to the seeds. We performed measurements with NaCl seeds which are known to be hygroscopic. Therefore the water molecules dissociate the NaCl cluster and a solvation process takes place. As a consequence, the charged sodium chloride seeds attract the vapor molecules stronger and thereby the nucleation and condensational growth can start at smaller seed sizes. In this work we assumed that the chemical composition and charging state are the driving forces of nucleation and growth in the size range of the cut-off diameter of the used UCPC. Hence we recommend that in future studies the chemical composition of the generated particles in different charging states should be investigated.

As described by Li and Hogan (2017), the impact of vapor polarity in the measured particle size range, where interactions between single atoms are of importance, cannot be neglected. Additional water molecules increase the dipole moment of the n-butanol/water mixture and can change the structure of the sodium chloride cluster. If water vapor is present charge effects on the surface promote the initial steps of nucleation even more. As a result, the energy barrier for activating nanometer sized NaCl particles can be reduced - this is comparable to already published results for n-propanol/water mixtures conducted by Petersen et al. (2001). Our data shows a strong effect of RH on heterogeneous nucleation of n-butanol on NaCl particles, but not for Ag seeds. This finding suggests that the different RH sensitivity is less a consequence of binary heterogeneous nucleation, but rather attributable to changing seed properties in the interaction with vapor molecules. According to the NaCl shrinkage measurements, a change in diameter during the presence of water vapor - which we associated with a restructural effect - could be observed.

To improve our understanding of the observed restructuring effect, future studies on heterogeneous nucleation depending on different seeds and humidity should be conducted. Also the herein presented measurements could be extended with the size selection after the particle restructuring. Additionally, higher RH conditions could be used to investigate the restructural effect on even smaller particles. In particular, the humidity dependent activation of hygroscopic nanoparticles which are present in the atmosphere would be of great interest. Thereby, the molecular interactions between the seed and the vapor molecules can be further evaluated which may lead to a model description.

Our results suggest that atmospheric measurements of ambient nanoparticles should take into account possible RH effects on the instrument's cut-off diameter, when a large hygroscopic particle fraction is present. Thus, number concentration measurements should be paired with chemical and/or hygroscopicity measurements to improve the assessment of the uncertainty. If these additional measurements cannot be conducted, the location of the measurement site should be taken into account for data interpretation. Especially when conducting studies in marine surroundings, at which sea spray is one of the contributing particle sources, special care should be taken during the data evaluation (Lawler et al., 2014; Zieger et al., 2017). As a standard procedure, in many atmospheric studies the CPC inlet flow is dried before entering the instrument. We suggest that additional monitoring of the RH of the inlet flow is critical, since the variation in RH between 0 and 40 % even shows a pronounced shift in the cut-off diameter. This would lead to an overestimation in the number concentration of nucleation mode particles. In ambient conditions this mode usually contains high number concentrations of particles. Comparison between measurements taken in different regions with varying hygroscopic nanoparticle concentrations thus need to be treated with care to avoid wrong interpretation.

3.5 Author Contributions

C.T. designed the setup, C.T. performed the SANC experiments, C.T., S.B. and P.J.W. performed the detection efficiency measurements, P.S.B. and G.K. performed the shrinkage measurements, C.T., S.B., P.J.W., G.S. and P.M.W. were involved in the scientific interpretation and discussion, and C.T., S.B., P.J.W. and P.M.W. wrote the manuscript.

3.5.1 Personal contributions

As part of this investigation, I was involved in setting up the experiment regarding the second part of this study, which is the setup for the measurement of the detection efficiency of the butanol-based CPC. This work included the introduction of the humidifier that was needed to perform the measurement at changing levels of relative humidity in the sample flow. I was part of the scientific discussion of the measurement results and took actively part in writing the manuscript.

3.6 References

- M. Alonso and F. J. Alguacil. Particle size distribution modification during and after electrical charging: Comparison between a corona ionizer and a radioactive neutralizer. *Aerosol and Air Quality Research*, 8(4):366–380, 2008. ISSN 20711409. doi:10.4209/aaqr.2008.07.0029.
- A. Ankilov, A. Baklanov, M. Colhoun, K. H. Enderle, J. Gras, Y. Julanov, D. Kaller, A. Lindner, A. A. Lushnikov, R. Mavliev, F. McGovern, T. C. O’Connor, J. Podzimek, O. Preining, G. P. Reischl, R. Rudolf, G. J. Sem, W. W. Szymanski, A. E. Vrtala, P. E. Wagner, W. Winklmayr, and V. Zagaynov. Particle size dependent response of aerosol counters. *Atmospheric Research*, 62(3-4):209–237, 2002. ISSN 01698095. doi:10.1016/S0169-8095(02)00011-X.
- K. Barmounis, A. Ranjithkumar, A. Schmidt-Ott, M. Attoui, and G. Biskos. Enhancing the detection efficiency of condensation particle counters for sub-2 nm particles. *Journal of Aerosol Science*, 117:44–53, 2018. ISSN 0021-8502. doi:10.1016/j.jaerosci.2017.12.005.
- G. Biskos, A. Malinowski, L. M. Russell, P. R. Buseck, and S. T. Martin. Nanosize effect on the deliquescence and the efflorescence of sodium chloride particles. *Aerosol Science and Technology*, 40(2):97–106, 2006. ISSN 02786826. doi:10.1080/02786820500484396.
- O. Boucher, D. Randall, P. Artaxo, C. Bretherton, G. Feingold, P. Forster, V.-M. Kerminen, Y. Kondo, H. Liao, U. Lohmann, P. Rasch, S. Satheesh, S. Sherwood, B. Stevens, and X. Zhang. IPCC, 2013: Clouds and Aerosols. In *Climate Change 2013: The Physical Science Basis. Contribution of Working Group I to the Fifth Assessment Report of the Intergovernmental Panel on Climate Change*, pages 571–658. Cambridge University Press, Cambridge, United Kingdom and New York, NY, USA, 2013. ISBN 9781107415324. doi:10.1017/CBO9781107415324.016.
- D. Castarède and E. S. Thomson. A thermodynamic description for the hygroscopic growth of atmospheric aerosol particles. *Atmospheric Chemistry and Physics*, 18(20):14939–14948, 2018. ISSN 16807324. doi:10.5194/acp-18-14939-2018.
- C. C. Chen and C. J. Tao. Condensation of supersaturated water vapor on submicrometer particles of SiO₂ and TiO₂. *Journal of Chemical Physics*, 112(22):9967–9977, 2000. ISSN 00219606. doi:10.1063/1.481633.
- H. Chen, S. Chee, M. J. Lawler, K. C. Barsanti, B. M. Wong, and J. N. Smith. Size resolved chemical composition of nanoparticles from reactions of sulfuric acid with ammonia and dimethylamine. *Aerosol Science and Technology*, 52(10):1120–1133, 2018. ISSN 15217388. doi:10.1080/02786826.2018.1490005.
- A. Clarke, V. Kapustin, S. Howell, K. Moore, B. Lienert, S. Masonis, T. Anderson, and D. Covert. Sea-salt size distribution from breaking waves: Implications for marine aerosol

- production and optical extinction measurements during SEAS. *Journal of Atmospheric and Oceanic Technology*, 20(10):1362–1374, 2003. ISSN 07390572. doi:10.1175/1520-0426(2003)020<1362:SSDFBW>2.0.CO;2.
- J. J. Ferreiro, S. Chakrabarty, B. Schläppi, and R. Signorell. Observation of propane cluster size distributions during nucleation and growth in a Laval expansion. *Journal of Chemical Physics*, 145:211907, 2016. ISSN 00219606. doi:10.1063/1.4960050.
- D. R. Hanson, F. L. Eisele, S. M. Ball, and P. M. McMurry. Sizing small sulfuric acid particles with an ultrafine particle condensation nucleus counter. *Aerosol Science and Technology*, 36(5):554–559, 2002. ISSN 02786826. doi:10.1080/02786820252883793.
- K. Iida, M. R. Stolzenburg, and P. H. McMurry. Effect of Working Fluid on Sub-2 nm Particle Detection with a Laminar Flow Ultrafine Condensation Particle Counter. *Aerosol Science and Technology*, 43(1):81–96, 2009. doi:10.1080/02786820802488194.
- J. Kangasluoma, H. Junninen, K. Lehtipalo, J. Mikkilä, J. Vanhanen, M. Attoui, M. Sipilä, D. R. Worsnop, M. Kulmala, and T. Petäjä. Remarks on ion generation for CPC detection efficiency studies in sub-3-nm size range. *Aerosol Science and Technology*, 47(5):556–563, 2013. ISSN 1521-7388. doi:10.1080/02786826.2013.773393.
- J. Kangasluoma, A. Samodurov, M. Attoui, A. Franchin, H. Junninen, F. Korhonen, T. Kurtén, H. Vehkamäki, M. Sipilä, K. Lehtipalo, D. R. Worsnop, T. Petäjä, and M. Kulmala. Heterogeneous Nucleation onto Ions and Neutralized Ions: Insights into Sign-Preference. *Journal of Physical Chemistry C*, 120(13):7444–7450, 2016. ISSN 19327455. doi:10.1021/acs.jpcc.6b01779.
- J. Kangasluoma, L. R. Ahonen, T. M. Laurila, R. Cai, J. Enroth, S. B. Mazon, F. Korhonen, P. P. Aalto, M. Kulmala, M. Attoui, and T. Petäjä. Laboratory verification of a new high flow differential mobility particle sizer, and field measurements in Hyytiälä. *Journal of Aerosol Science*, 124(June):1–9, 2018. ISSN 18791964. doi:10.1016/j.jaerosci.2018.06.009.
- L. Krämer, U. Pöschl, and R. Niessner. Microstructural rearrangement of sodium chloride condensation aerosol particles on interaction with water vapor. *Journal of Aerosol Science*, 31(6):673–685, 2000. ISSN 00218502. doi:10.1016/S0021-8502(99)00551-0.
- C. Kuang, I. Riipinen, S. L. Sihto, M. Kulmala, A. V. McCormick, and P. H. McMurry. An improved criterion for new particle formation in diverse atmospheric environments. *Atmospheric Chemistry and Physics*, 10(17):8469–8480, 2010. ISSN 16807316. doi:10.5194/acp-10-8469-2010.
- C. Kuang, M. Chen, J. Zhao, J. Smith, P. H. McMurry, and J. Wang. Size and time-resolved growth rate measurements of 1 to 5 nm freshly formed atmospheric nuclei. *Atmospheric*

-
- Chemistry and Physics*, 12(7):3573–3589, 2012. ISSN 16807316. doi:10.5194/acp-12-3573-2012.
- M. Kulmala, A. Lauri, H. Vehkamäki, A. Laaksonen, D. Petersen, and P. E. Wagner. Strange predictions by binary heterogeneous nucleation theory compared with a quantitative experiment. *Journal of Physical Chemistry B*, 105(47):11800–11808, 2001. ISSN 10895647. doi:10.1021/jp011740c.
- M. Kulmala, L. Laakso, K. E. J. Lehtinen, I. Riipinen, M. Dal Maso, T. Anttila, V.-M. Kerminen, U. Hörrak, M. Vana, and H. Tammet. Initial steps of aerosol growth. *Atmospheric Chemistry and Physics*, 4(11/12):2553–2560, 2004a. doi:10.5194/acpd-4-5433-2004.
- M. Kulmala, H. Vehkamäki, T. Petäjä, M. Dal Maso, A. Lauri, V. M. Kerminen, W. Birmili, and P. H. McMurry. Formation and growth rates of ultrafine atmospheric particles: A review of observations. *Journal of Aerosol Science*, 35(2):143–176, 2004b. ISSN 00218502. doi:10.1016/j.jaerosci.2003.10.003.
- M. Kulmala, T. Petäjä, M. Ehn, J. Thornton, M. Sipilä, D. Worsnop, and V.-M. Kerminen. Chemistry of Atmospheric Nucleation: On the Recent Advances on Precursor Characterization and Atmospheric Cluster Composition in Connection with Atmospheric New Particle Formation. *Annual Review of Physical Chemistry*, 65(1):21–37, 2014. ISSN 0066-426X. doi:10.1146/annurev-physchem-040412-110014.
- A. Kupc, P. M. Winkler, A. Vrtala, and P. Wagner. Unusual temperature dependence of heterogeneous nucleation of water vapor on Ag particles. *Aerosol Science and Technology*, 47(9):i–iv, 2013. ISSN 02786826. doi:10.1080/02786826.2013.810330.
- M. J. Lawler, J. Whitehead, C. O’Dowd, C. Monahan, G. McFiggans, and J. N. Smith. Composition of 15–85 nm particles in marine air. *Atmospheric Chemistry and Physics*, 14(21):11557–11569, 2014. ISSN 16807324. doi:10.5194/acp-14-11557-2014.
- C. Li and C. J. Hogan. Vapor specific extents of uptake by nanometer scale charged particles. *Aerosol Science and Technology*, 51(5):653–664, 2017. ISSN 15217388. doi:10.1039/B904022F.
- M. Loudon. *Organic Chemistry*. Roberts & Company, 5th edition, 2009.
- S. T. Martin. Phase transitions of aqueous atmospheric particles. *Chemical Reviews*, 100(9):3403–3453, 2000. ISSN 00092665. doi:10.1021/cr990034t.
- R. McGraw, J. Wang, and C. Kuang. Kinetics of heterogeneous nucleation in supersaturated vapor: fundamental limits to neutral particle detection revisited. *Aerosol Science and Technology*, 46(9):1053–1064, 2012. ISSN 02786826. doi:10.1080/02786826.2012.687844.

- R. L. McGraw, P. M. Winkler, and P. E. Wagner. Temperature Dependence in Heterogeneous Nucleation with Application to the Direct Determination of Cluster Energy on Nearly Molecular Scale. *Scientific Reports*, 7(1):1–11, 2017. ISSN 20452322. doi:10.1038/s41598-017-16692-9.
- P. H. McMurry. Chapter 17 A review of atmospheric aerosol measurements. *Developments in Environmental Science*, 34:1959–1999, 2000. ISSN 14748177. doi:10.1016/S1474-8177(02)80020-1.
- P. H. McMurry, M. Fink, H. Sakurai, M. R. Stolzenburg, I. L. Mauldin, J. Smith, F. Eisele, K. Moore, S. Sjostedt, D. Tanner, L. G. Huey, J. B. Nowak, E. Edgerton, and D. Voisin. A criterion for new particle formation in the sulfur-rich Atlanta atmosphere. *Journal of Geophysical Research Atmospheres*, 110(22):1–10, 2005. ISSN 01480227. doi:10.1029/2005JD005901.
- J. Merikanto, D. V. Spracklen, G. W. Mann, S. J. Pickering, and K. S. Carslaw. Impact of nucleation on global CCN. *Atmos. Chem. Phys*, 9:8601–8616, 2009. doi:10.5194/acp-9-8601-2009.
- D. Petersen, R. Ortner, A. Vrtala, P. E. Wagner, M. Kulmala, and A. Laaksonen. Soluble-insoluble transition in binary heterogeneous nucleation. *Physical Review Letters*, 87(22):225703–225703–4, 2001. ISSN 10797114. doi:10.1103/PhysRevLett.87.225703.
- C. Reichardt and T. Welton. *Solvents and Solvent Effects in Organic Chemistry*. Wiley-VCH, 4th edition, 2010. doi:10.1002/anie.201105531.
- H. Sakurai, M. A. Fink, P. H. McMurry, L. Mauldin, K. F. Moore, J. N. Smith, and F. L. Eisele. Hygroscopicity and volatility of 4–10 nm particles during summertime atmospheric nucleation events in urban Atlanta. *Journal of Geophysical Research Atmospheres*, 110(22):1–10, 2005. ISSN 01480227. doi:10.1029/2005JD005918.
- H. G. Scheibel and J. Porstendörfer. Generation of monodisperse Ag- and NaCl-aerosols with particle diameters between 2 and 300 nm. *Journal of Aerosol Science*, 14(2):113–126, 1983. ISSN 00218502. doi:10.1016/0021-8502(83)90035-6.
- S. Schobesberger, P. M. Winkler, T. Pinterich, A. Vrtala, M. Kulmala, and P. E. Wagner. Experiments on the temperature dependence of heterogeneous nucleation on nanometer-sized NaCl and Ag particles. *ChemPhysChem*, 11(18):3874–3882, 2010. ISSN 14394235. doi:10.1002/cphc.201000417.
- G. J. Sem. Design and performance characteristics of three continuous-flow condensation particle counters: A summary. *Atmospheric Research*, 62(3-4):267–294, 2002. ISSN 01698095. doi:10.1016/S0169-8095(02)00014-5.

-
- J. N. Smith, K. F. Moore, P. H. McMurry, and F. L. Eisele. Atmospheric Measurements of Sub-20 nm Diameter Particle Chemical Composition by Thermal Desorption Chemical Ionization Mass Spectrometry. *Aerosol Science and Technology*, 38(2):100–110, 2004. ISSN 02786826. doi:10.1080/02786820490249036.
- D. V. Spracklen, K. S. Carslaw, M. Kulmala, V. M. Kerminen, S. L. Sihto, I. Riipinen, J. Merikanto, G. W. Mann, M. P. Chipperfield, A. Wiedensohler, W. Birmili, and H. Lihavainen. Contribution of particle formation to global cloud condensation nuclei concentrations. *Geophysical Research Letters*, 35(6):1–5, 2008. ISSN 00948276. doi:10.1029/2007GL033038.
- R. Strey, P. E. Wagner, and T. Schmeling. Homogeneous nucleation rates for n -alcohol vapors measured in a two-piston expansion chamber. *The Journal of Chemical Physics*, 84(4):2325–2335, 1986. ISSN 0021-9606. doi:10.1063/1.450396.
- C. Tauber, X. Chen, P. E. Wagner, P. M. Winkler, C. J. Hogan, and A. Maißer. Heterogeneous Nucleation onto Monoatomic Ions: Support for the Kelvin-Thomson Theory. *ChemPhysChem*, 19:3144–3149, 2018. ISSN 14397641. doi:10.1002/cphc.201800698.
- C. Tauber, S. Brilke, P. J. Wlasits, P. S. Bauer, G. Köberl, G. Steiner, and P. M. Winkler. Humidity effects on the detection of soluble and insoluble nanoparticles in butanol operated condensation particle counters. *Atmospheric Measurement Techniques*, 12:3659–3671, 2019a. doi:10.5194/amt-12-3659-2019.
- C. Tauber, G. Steiner, and P. M. Winkler. Counting efficiency determination from quantitative intercomparison between expansion and laminar flow type condensation particle counter. *Aerosol Science and Technology*, 53(3):344–354, 2019b. ISSN 15217388. doi:10.1080/02786826.2019.1568382.
- W. Thomson. On the equilibrium of vapour at a curved surface of liquid. *The London, Edinburgh, and Dublin Philosophical Magazine and Journal of Science*, 42(282):448–452, 1871. ISSN 1941-5982. doi:10.1080/14786447108640606.
- P. E. Wagner. A constant-angle mie scattering method (cams) for investigation of particle formation processes. *Journal of Colloid And Interface Science*, 105(2):456–467, 1985. ISSN 00219797. doi:10.1016/0021-9797(85)90319-4.
- P. E. Wagner, D. Kaller, A. Vrtala, A. Lauri, M. Kulmala, and A. Laaksonen. Nucleation probability in binary heterogeneous nucleation of water–n-propanol vapor mixtures on insoluble and soluble nanoparticles. *Physical Review E - Statistical Physics, Plasmas, Fluids, and Related Interdisciplinary Topics*, 67(2):12, 2003. ISSN 1063651X. doi:10.1103/PhysRevE.67.021605.

- J. Wang, R. L. McGraw, and C. Kuang. Growth of atmospheric nano-particles by heterogeneous nucleation of organic vapor. *Atmospheric Chemistry and Physics*, 13(13):6523–6531, 2013. ISSN 16807316. doi:10.5194/acp-13-6523-2013.
- A. Wiedensohler, D. Orsini, D. S. Covert, D. Coffmann, W. Cantrell, M. Havlicek, F. J. Brechtel, L. M. Russell, R. J. Weber, J. Gras, J. G. Hudson, and M. Litchy. Intercomparison study of the size-dependent counting efficiency of 26 condensation particle counters. *Aerosol Science and Technology*, 27(2):224–242, 1997. ISSN 15217388. doi:10.1080/02786829708965469.
- P. M. Winkler, A. Hienola, G. Steiner, G. Hill, A. Vrtala, G. P. Reischl, M. Kulmala, and P. E. Wagner. Effects of seed particle size and composition on heterogeneous nucleation of n-nonane. *Atmospheric Research*, 90(2-4):187–194, 2008a. ISSN 01698095. doi:10.1016/j.atmosres.2008.02.001.
- P. M. Winkler, G. Steiner, A. Vrtala, H. Vehkamäki, M. Noppel, K. E. Lehtinen, G. P. Reischl, P. E. Wagner, and M. Kulmala. Heterogeneous nucleation experiments bridging the scale from molecular ion clusters to nanoparticles. *Science*, 319:1374–1377, 2008b. ISSN 00368075. doi:10.1126/science.1149034.
- P. M. Winkler, R. L. McGraw, P. S. Bauer, C. Rentenberger, and P. E. Wagner. Direct determination of three-phase contact line properties on nearly molecular scale. *Scientific Reports*, 6(2):1–7, 2016. ISSN 20452322. doi:10.1038/srep26111.
- P. J. Wlasits. On the Effect of Relative Humidity on the Activation of Aerosol Particles in Butanol Based Condensation Particle Counters. Master’s thesis, University of Vienna, 2019. URL <http://othes.univie.ac.at/>.
- P. Zieger, O. Väisänen, J. C. Corbin, D. G. Partridge, S. Bastelberger, M. Mousavi-Fard, B. Rosati, M. Gysel, U. K. Krieger, C. Leck, A. Nenes, I. Riipinen, A. Virtanen, and M. E. Salter. Revising the hygroscopicity of inorganic sea salt particles. *Nature Communications*, 8:15883, 2017. ISSN 20411723. doi:10.1038/ncomms15883.

Chapter 4

New particle formation and sub-10 nm size distribution measurements during the A-LIFE field experiment in Paphos, Cyprus

This chapter was submitted by S. Brilke, N. Fölker, T. Müller, K. Kandler, X. Gong, J. Peischl, B. Weinzierl & P.M. Winkler to *Atmospheric Chemistry and Physics* on Dec 4 2019 and has been accepted to *ACP Discussions* on Dec 11 2019.

doi: <https://doi.org/10.5194/acp-2019-1123>.

Abstract. Atmospheric particle size distributions were measured in Paphos, Cyprus, during the A-LIFE (**A**bsorbing aerosol layers in a changing climate: aging, **l**ifetime and dynamics) field experiment from April 3 – 30, 2017. The newly developed DMA-train is deployed for the first time in an atmospheric environment for the direct measurement of the nucleation mode size range between 1.8 – 10 nm diameter. The DMA-train setup consists of seven size channels, of which five are set to fixed particle mobility diameters and two additional diameters are obtained by alternating voltage settings in one DMA every 10 s. In combination with a conventional Mobility Particle Size Spectrometer (MPSS) and an Aerodynamic Particle Sizer (APS) the complete atmospheric aerosol size distribution from 1.8 nm – 10 μ m is covered. The focus of the A-LIFE study is to characterize new particle formation (NPF) in the Eastern Mediterranean region at a measurement site with strong local pollution sources. The nearby Paphos airport was found to be a large emission source for nucleation mode particles and we analysed the size distribution of the airport emission plumes at approximately 500 m from the main runway. The analysis yielded 9 NPF events in 27 measurement days from the combined analysis of the DMA-train, MPSS and trace gas monitors. Growth rate calculations were performed and a size-dependency of the initial growth rate (< 10 nm) is observed for one event case. Fast changes of the sub-10 nm size distribution on the timescale of a few minutes are captured by the DMA-train measurement during early particle growth and are discussed in a second event case. In 2 cases, particle formation and growth were detected in the nucleation mode size range which did not exceed the 10 nm threshold. This finding implies that NPF likely occurs more frequently than estimated from studies where the lower nanometre size regime is not covered by the size distribution measurements.

4.1 Introduction

New particle formation (NPF) is a major source of nucleation mode particles which form from low-volatility vapours in the atmosphere. Freshly formed particles can eventually grow to sizes where they scatter light or become cloud condensation nuclei (CCN). NPF is known to significantly contribute to the global total particle concentration and CCN budget (Merikanto et al., 2009; Spracklen et al., 2006). Understanding the feedback on the global climate of secondary aerosol requires a profound knowledge of the NPF frequency and processes promoting the formation and growth. Global modeling studies need a large set of observation points throughout the atmosphere. The number of sites observing NPF is increasing and includes studies in remote areas (Kecorius et al., 2019; Pikridas et al., 2012; Weber et al., 1995), coastal and continental regions (Hoffmann et al., 2001; Mäkelä et al., 1997; Weber et al., 1997), the free troposphere (Bianchi et al., 2016; Williamson et al., 2019) and polluted environments (Hamed et al., 2007; Stolzenburg et al., 2005; Yao et al., 2018; Yu et al., 2016).

Size-resolved particle measurements down to the diameters of freshly nucleated particles provide insight into the dynamics of the processes of aerosol nucleation and growth. Commonly, measurements are performed by charging particles using a radioactive or x-ray ionization source, classifying them according to their electrical mobility using a Differential Mobility Analyser (DMA) and detecting them in a Condensation Particle Counter (CPC) or Faraday Cup Electrometer (FCE). Measuring size-resolved particle number concentrations in the nucleation mode size range is challenging because the efficiencies for transmission, charging and detection of sub-10 nm particles are low.

Different approaches have been made to access information on the dynamics of nucleation mode particles. The Neutral cluster and Air Ion Spectrometer (NAIS) is a frequently implemented method to measure the size distribution of charged and neutral clusters (< 3 nm) using a DMA coupled to a set of parallel FCEs (Manninen et al., 2009). The advantage of using the FCE as a detector is that it provides a size-independent detection of charged particles whereas the drawback lies in the fact that FCEs have a lower sensitivity compared to CPCs. Therefore, higher particle concentrations must be present to achieve a measurable signal. Mobility Particle Size Spectrometers in scanning mode operation (MPSS) commonly classify particles in a DMA and optically detect them in a CPC. The sensitivity of the CPC to low particle concentrations is higher compared to FCEs but the size-dependent detection of the used CPC results in larger uncertainties, requiring detailed calibration procedures (Kangasluoma and Kontkanen, 2017). By implementing a low cut-off CPC, e.g. a diethylene glycol-based CPC, the complete number size distribution of neutral particles has been measured during nucleation events in the atmosphere (Jiang et al., 2011). In recent efforts, the Caltech nano-Scanning Electrical Mobility Spectrometer (nSEMS) was developed to combine the measurement of neutral particles and particles of both polarities in the lower nanometre

size regime with minimised diffusional losses (Amanatidis et al., 2019). However, scanning the voltage of a DMA over the complete mobility range takes time and the time resolution of a scanning device typically varies between 5 to 10 minutes. Counting statistics become an issue when the signal in the detector is low which is the case for sub-10 nm particles due to large diffusional losses despite high number concentrations during nucleation events.

In this study, we meet the challenge of measuring sub-10 nm particles using the newly-developed DMA-train (Stolzenburg et al., 2017). In contrast to conventional particle sizers with a single scanning classifier, the DMA-train utilizes six DMAs in parallel operated at fixed voltages with each DMA coupled to a CPC. This arrangement allows size distribution measurements of neutral atmospheric particles at a time resolution on the order of a few seconds. The main advancement is that the DMA-train has an increased sensitivity towards low particle counts especially in the lower size channels, due to the permanent monitoring of individual sizes that can be used for statistical analysis. During the A-LIFE field experiment in Cyprus, the DMA-train was, for the first time, implemented in an atmospheric environment. The Mediterranean region is subject of various aerosol types from different sources such as biomass burning, fuel combustion, sea spray aerosol, mineral dust and secondary aerosol. Here, we focus on secondary aerosol in the Paphos region where strong local pollution sources are present, and capture the sub-10 nm particle dynamics during nucleation events. NPF was found to frequently occur in the Eastern Mediterranean atmosphere (Debevec et al., 2018; Kalivitis et al., 2008; Manninen et al., 2010; Pikridas et al., 2012), and the results from this study contribute more detailed information on the nucleation mode particle size range.

4.2 Methods

4.2.1 Sampling site

The island of Cyprus is situated in the Eastern Mediterranean Sea (Figure 4.1) and is a unique location where air masses converge from several distinct origins carrying complex aerosol mixtures. The Sahara Desert and the Arabian Peninsula are sources of mineral dust-rich air masses from the south. Contributions from biomass burning are expected to originate from the Turkish mainland to the northeast. Anthropogenic pollution is transported to the Cyprus region from Southeast Europe and the Middle East. The Paphos ground-based station (34°42'40.5"N 32°28'58.5"E) is close to the Paphos International Airport, which is located approximately 500 m to the northeast from the measurement site. The coastline is 50 m away and extends from the southeast to the northwest. Emissions from ships arriving at and passing by Paphos are expected to contribute to the local urban pollution. The nearest and largest urban center is Paphos, with 36000 inhabitants located 5 km to the northwest. The streets surrounding the measurement station carry a medium-to-high traffic load. The

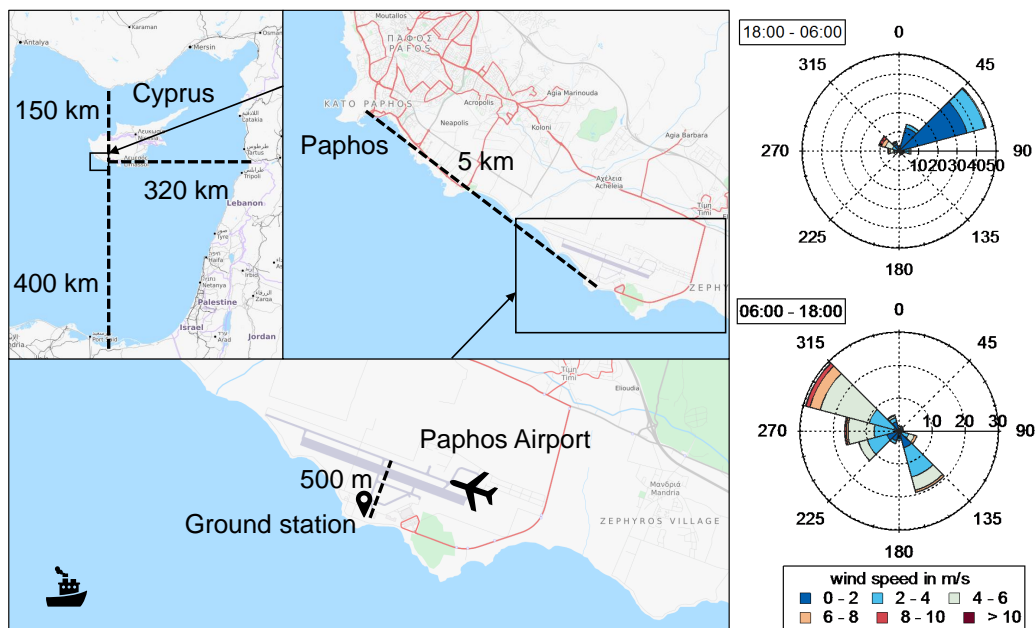


Figure 4.1. The island of Cyprus is located in the Eastern Mediterranean Sea. Paphos is situated 150 km from the Turkish coast, 320 km from Syria and Lebanon and 400 km from Egypt. The measurement station was located at the coastline at the Paphos International Airport which is 5 km southeast from Paphos city center. The runway of the Paphos airport is at approximately 500 m distance northeast to the measurement station. The wind roses in the right panel show the wind frequency distribution during the measurement period, April 1 – 30, 2017. The local land-sea-breeze system dominates the local wind pattern. During night-time (18:00 – 08:00), the wind is primarily northeast at low wind speed between 0.5 – 4 m/s. The sea breeze during daytime (08:00 – 18:00) is mostly southeast or northwest with highest wind speeds. Wind roses were plotted using the Zefir tool (Petit et al., 2017) and the map is from OpenStreetMap (© OpenStreetMap contributors 2019. Distributed under a Creative Commons BY-SA License.).

Troodos mountain range, located about 30 km from the station, contains a large amount of vegetation and reaches up to 2000 m elevation. In summary, the sampling site can be characterized as rural polluted with a marine background and strong local pollution sources. In Figure 4.1, the wind roses in the right panel show the local land-sea-breeze system with the prevailing wind direction from the northeast during night-time (18:00 – 06:00) at low wind speeds, and from the northwest during day-time (06:00 – 18:00) at higher wind speeds.

4.2.2 Ground-based measurements

The A-LIFE intensive measurement campaign was conducted from April 3 – 30, 2017. Measurements of the particle size distribution were performed using a DMA-train in the size range between 1.8 - 10 nm at a time resolution of 1 s. A MPSS (Wiedensohler et al., 2018) in

combination with an Aerodynamic Particle Sizer (APS) covered the size range from 10 nm – 10 μm at 5 min time resolution. An aerosol PM_{10} inlet was installed on top of the measurement container to remove particles larger than 10 μm in aerodynamic diameter (find a more detailed description in Gong et al. (2019)). The total particle concentration was measured at 1 s time resolution using an Airmodus A10 Particle Size Magnifier (PSM) in combination with a TSI UCPC Model 3776 as a detector with a dried total inlet flow rate of 10 L/min using a core sampling probe (RH < 40 %). Complementary trace gas measurements were performed using a NO-NO₂ monitor, O₃ monitor and SO₂ monitor with periodic background measurements performed using synthetic air. The NO-NO₂ monitor was calibrated after the measurement campaign. SO₂ data are available for the last third of the measurement period without calibration; therefore, we use the SO₂ data qualitatively. Meteorological parameters such as temperature, relative humidity, solar irradiance, wind speed and wind direction were measured throughout the measurement period.

4.2.3 The DMA-train experimental setup

The DMA-train measures the particle size distribution starting at 1.8 nm mobility diameter up to 10 nm in seven size channels. The setup is presented schematically in Figure 4.9 in the supplemental information (SI). The sample aerosol is drawn through 1" stainless-steel tubing at a total flow rate of 21 L/min. A core sampling probe extracts a flow of 11 L/min to the DMA-train system consisting of two symmetric layers with an aerosol charger and three DMAs each followed by a CPC. The sample flow is evenly split into two 5.5 L/min flows which are guided to one layer each. The aerosol sample enters a soft x-ray based Advanced Aerosol Neutralizer (TSI 3088, AAN) where particles are charged for the subsequent classification in three DMAs (Grimm S-DMAs) prior to particle detection in the particle counters. The aerosol flow rate in the DMAs is determined by the inlet flow rate of the CPCs. Each DMA is operated at a fixed set voltage and particles of the respective mobility diameter are counted in each size channel. The DMA-train is a modular system where single parts, e.g. the CPCs, can be easily exchanged depending on the requirements of a measurement. Here, an Airmodus A10 Particle Size Magnifier (PSM), a turbulent mixing-type DEG-based growth stage, was implemented at the first and lowest channel for the activation of the smallest particles with a butanol-based TSI CPC Model 3772 for particle detection at a total inlet flow rate of 2.5 L/min. The second channel was equipped with the laminar-flow DEG-based TSI UCPC Model 3777 ("nanoEnhancer") followed by a butanol-based TSI UCPC Model 3772, also at a flow rate of 2.5 L/min. In the third and fourth channels, two TSI UCPC Model 3776 with an inlet flow rate of 1.5 L/min were implemented and operated at modified temperature settings, i.e. the saturator temperature was set to 30.1 °C and the condenser temperature set at 0.1 °C for enhanced particle activation (Barmounis et al., 2018; Tauber et al., 2019). A water-based

TSI CPC Model 3788 was employed in the fifth channel. The last channel was operated with a TSI UCPC Model 3776 at standard temperature settings. Here, the DMA voltage was not entirely fixed but alternated in a 10 s time interval to cover one additional size channel. The DMAs are operated using a closed-loop sheath flow rate of 15 L/min. Silica gel dryers are used in every sheath flow loop to keep the RH of the sheath flow below 10 %.

4.2.4 DMA-train data analysis

DMA-train data considerations

The inversion of the DMA-train data to get information on the number concentration of particles in each size bin at each single DMA is performed as described in Stolzenburg and McMurry (2008). Detailed information on the instrument transmission of the DMA-train setup and transfer function of the DMAs can be found in Stolzenburg et al. (2017). The particle charging efficiency is calculated from Wiedensohler's approximation (Wiedensohler, 1988) for negatively charged particles. However, the counting efficiency of the CPC renders a large uncertainty when the classified diameter lies in the size range where the diameter-dependent counting efficiency is increasing, i.e. in the ascent of the counting efficiency curve. This is especially true for the smallest classified particle sizes of the DMA-train setup. The CPC counting efficiency is dependent on the aerosol composition, seed solubility, the RH of the sample flow and instrument settings. Here, we account for the possible above-mentioned effects on the counting efficiency when the aerosol sample is exposed to humid air. Previous studies have shown that the RH and the seed solubility with respect to the working fluid have an influence on the CPC detection efficiency (Kangasluoma et al., 2013; Tauber et al., 2019). To appropriately account for the seed variability present in the atmosphere, we used the mean counting efficiency at the classified diameter using results of the counting efficiency for silver and sodium chloride particles exposed to 0 % or 10 % RH as a best estimate. The range of RH of the aerosol flow at the CPC inlets between 0 and 10 % is limited by the controlled humidity of the sheath flows of the DMAs. The uncertainty on the counting efficiency from the mentioned factors is estimated to ± 10 %. As an overall estimate we assume ± 20 % uncertainty on the number concentration in each size channel. Background measurements were conducted at least twice a day with the DMA voltage in each channel set to zero. The background values were typically 0 cm^{-3} except for the Airmodus PSM, which varied with the outside RH between 0 and 1 cm^{-3} . The DMA-train's increased sensitivity to a low particle signal is dependent on a stable background signal. The PSM instrument settings have been adjusted accordingly, and the possible effects of this correction were considered during the analysis.

Growth rate analysis

Detailed growth rate measurements using the appearance time method have previously been performed using the DMA-train in chamber studies (Stolzenburg et al., 2018). During ambient measurements, the growth rate measurement is not always as obvious as during laboratory studies. Inhomogeneous atmospheric mixing and changing atmospheric parameters may affect the number concentration measured in each size channel and lead to a less distinct signal used for the growth rate analysis. A method for determining the particle growth rate based on the evolution of the nucleation mode peak was presented by Lehtinen and Kulmala (2003). In this study, the time, t_{mode} , of the maximum of each particle size channel, i.e. $D_{p,mode}$, was determined using a Gaussian fit which is demonstrated to work well in Figure 4.10 (SI). As a best estimate for the uncertainty of the time of the mode peak, the full-width-half-maximum of each fit was used. The uncertainty on the diameter is given by the DMA flow configuration. The growth rate (GR) is calculated from the offset between the mode diameter, $\Delta D_{p,mode}$, and the times of the peak mode, Δt_{mode} :

$$GR = \frac{\Delta D_{p,mode}}{\Delta t_{mode}} \quad (4.1)$$

In this analysis, the mode diameter is plotted versus the time of the mode peak as presented in Figure S3. A linear fit from an orthogonal-distance-regression of the data is used to determine the growth rate directly, and accounts for the error in the time of the mode peak and the mode diameter. This method was applied in two size intervals, i.e. between 1.8 – 3.2 nm and 3.2 – 10 nm, where differences in the growth rate have been observed.

Event classification

One objective of this study is the characterization of the measurement site regarding the occurrence of NPF. An NPF event is determined from the nanoparticle size distribution data. The classification scheme for sorting a measurement day of differential mobility particle sizer (DMPS) data into the three categories, event, non-event and undefined day was first introduced by Dal Maso et al. (2005). In this established classification scheme, a day is classified into an event day if an NPF event takes place based on visually analysing the size distribution data. The criteria for an NPF event to take place are given by the appearance of a new particle mode (< 25 nm), which persists at least for one hour and grows within several hours. Mazon et al. (2009) added classification criteria to categorize undefined days into sub-categories such as pollution-related peaks and ultrafine-mode peaks.

The criteria given by Dal Maso et al. (2005) were applied to the MPSS data and adjusted for categorizing the DMA-train data, i.e. the sub-10 nm nanoparticle population, into event,

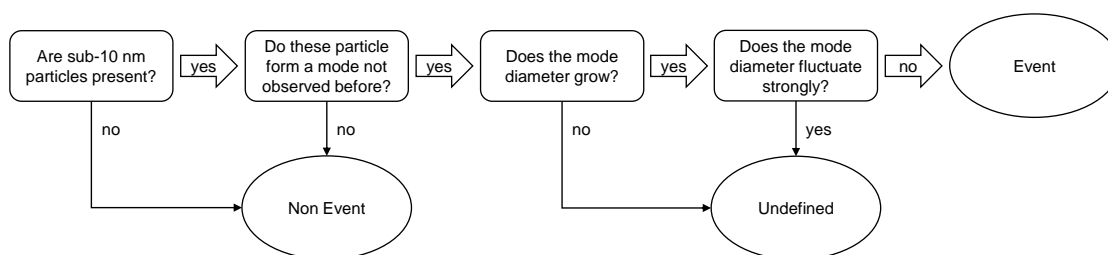


Figure 4.2. Classification scheme modified from Dal Maso et al. (2005) for categorizing the sub-10 nm DMA-train data into event, non-event and undefined days.

non-event and undefined days as displayed in Figure 4.2. The DMA-train data was visually analysed and classified into the three cases. Trace gas data were included in the NPF analysis to further distinguish between pollution-related peaks and NPF events. Accordingly, the MPSS size distribution data were analysed for NPF event days based on the classification scheme of Dal Maso et al. (2005). In the following sections, specific event cases of particle nucleation and growth that were observed during the A-LIFE measurement period are presented and discussed.

4.3 Results and Discussion

4.3.1 New particle formation events during A-LIFE

Several events were classified based on the DMA-train classification scheme depicted in Figure 4.2 in the sub-10 nm size regime. Figure 4.3 shows three typical cases of the resulting DMA-train size distribution illustrating an event, non-event and undefined day. Panel (a) shows a size distribution revealing a new mode of nanoparticle growth which is classified as an event day. Panel (b) demonstrates a non-event case. When a mode of nanoparticles appears but does not continue to grow, it is referred to as an undefined day, which is shown in the third panel (c). Table 4.1 summarizes the days when an event was either observed in the DMA-train or in the MPSS particle size distribution. The remaining days were classified as non-event days. Additionally, results of the condensation sink (CS), which is the rate at which molecules condense onto pre-existing particles, were added (Lehtinen et al., 2003). For the sub-10 nm size distribution, an event was identified in 5 cases whereas 7 event days were found for particles larger than 10 nm during 27 total measurement days. The events were observed during morning hours after sunrise when solar radiation and photochemistry typically trigger the formation of clusters. The combined analysis of the sub-10 nm particle size distribution obtained by the DMA-train and the particle population between 10 – 1000 nm from the MPSS

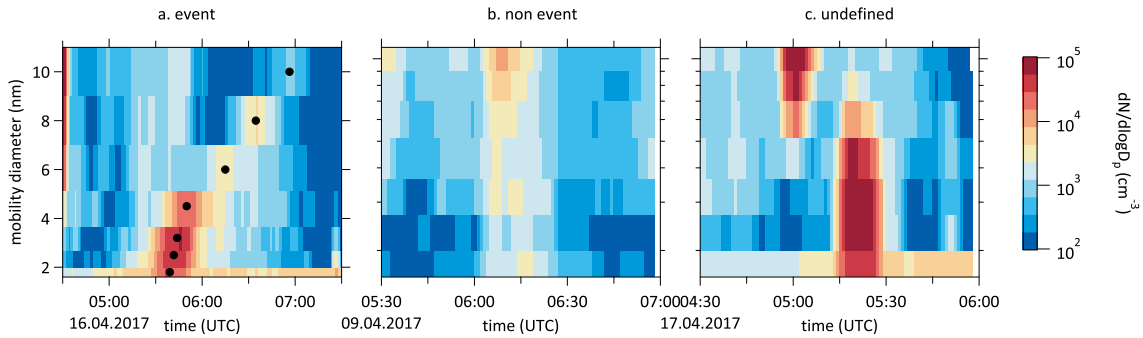


Figure 4.3. Three different patterns of the sub-10 nm particle number size distribution measured with the DMA-train. The left panel (a.) shows the case of an event day exhibiting a growing mode diameter (black markers). A non-event day is illustrated in the middle panel (b.) where no new particle mode is formed. The right panel (c.) shows an undefined day with a new particle mode forming which does not show signs of particle growth.

data shows that an event does not necessarily occur both in the DMA-train and the MPSS. However, the non-coincidence of events can have several reasons: i) an NPF event occurs but particles do not grow to sizes large enough to be detected in the MPSS, e.g. because of a lack of condensable vapours, ii) the particle concentration is below the DMA-train's lower detection limit or an existing particle population is carried to the measurement station with a mode diameter larger than 10 nm or, iii) meteorological conditions change, e.g. a change in air mass or wind direction occurs. We have analysed the particle size distribution data under consideration of the above-mentioned factors. Regarding the first possibility, i), the condensation sink, as listed in Table 4.1, does not give an indication. The reason for a lack of event identification in the DMA-train on April 8 and 9 is likely provided by the explanation given in ii) by an air mass change. On April 8 a night-time NPF event at particle concentrations lower than during the typical day-time event occurs, which suggests that the signal was insufficient for detection in the DMA-train. It is also possible, that the first steps of particle formation happened at another location and the particle population was transported to the measurement station. Interestingly, two days (April 16 and 20) show a growing mode in the sub-10 nm regime which does not continue to grow. The analysis of the meteorological parameters showed that at the stage of early particle growth the wind direction changed. The switch from land breeze to sea breeze typically occurs during morning hours, which here happened just after the start of early particle growth. Evidently, the conditions promoting the growth may change which leads to a disruption of the growing particle mode. Likewise, the particle population may be carried away and evolve at some other location. The important fact here is that NPF might occur more frequently than is assumed from studies that do not include the size distribution below 10 nm. In the following, the event case of April 16 will be discussed in more detail.

Table 4.1. Results of the event classification during the measurement period from April 3 – 30, 2017. Those days of April where an event day was classified either in the DMA-train or in the MPSS are displayed. Growth rates (in nm/h) from the DMA-train data in two size intervals (1.8 – 3.2 nm and 3.2 – 10 nm) and from MPSS data in one size interval (10 – 25 nm) are listed here with the prevailing wind direction during the growth in brackets. On April 5, 2017, the growth rate analysis was impossible due to insufficient DMA-train data availability during the event (N/A*). Strong fluctuations in the number size distribution did not allow to infer the growth rate on April 12 (N/A**). The mean condensation sink (CS in $1 \times 10^{-3} \text{ s}^{-1}$) was averaged over the course of the event period and is added here.

Day	DMA-train	MPSS	GR _{1.8–3.2}	GR _{3.2–10}	GR _{10–25}	CS
4	N/A	event			11.0 ± 0.6 [SE]	7.6
5	event	event	N/A*	N/A*	2.4 ± 0.1 [SE]	7.0
8	non-event	event			5.8 ± 0.7 [NW]	3.8
9	non-event	event			3.5 ± 0.1 [NW]	6.3
12	event	event	N/A** [SE]	N/A** [SE]	N/A** [SE]	3.6
16	event	non-event	18.2 ± 0.5 [NE]	5.5 ± 0.1 [SE]		7.8
20	event	non-event		5.8 ± 0.7 [SE]		3.5
21	undefined	event			2.7 ± 0.1 [SE]	4.5
22	event	event		5.7 ± 0.2 [NE]	3.0 ± 0.1 [NW]	5.8

During the time window of the A-LIFE campaign, nucleation mode particles were found to originate either from NPF or strong pollution sources, such as the nearby airport.

4.3.2 Nucleation mode particles from new particle formation and growth rates

We have presented a scheme to classify events, non-events and undefined sequences of the time series of the number size distribution. Two event cases are discussed here regarding their correlation with trace gases, meteorological parameters and particle growth. The first event, on April 16, shows a clear growing nucleation mode which is suppressed before it is observed by the instrumentation covering particle sizes larger than 10 nm. In the second case, an NPF event is detected with a mode diameter growing from the lowest detectable sizes into the Aitken mode throughout the whole day of April 22.

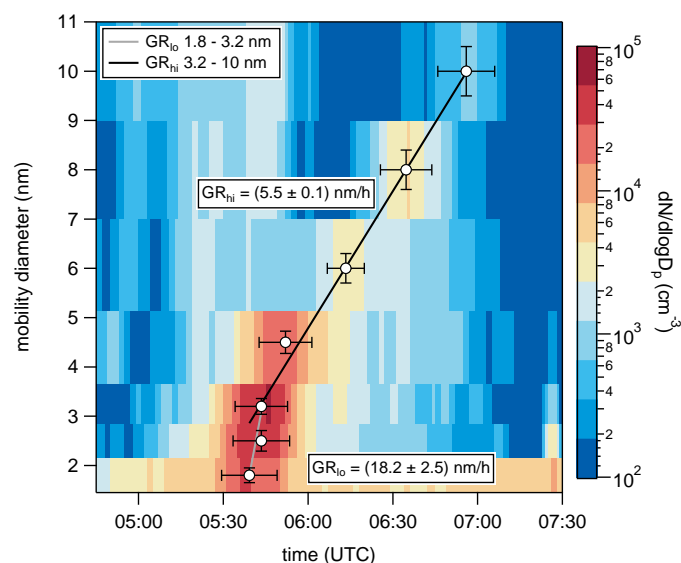


Figure 4.4. Event on April 16, 2017. The set mobility diameter in each size channel is plotted versus the time of the mode peak (white markers) with the time series of the number size distribution in the background. The growth rate can be directly determined from the slope of the fit to the diameter by applying a linear fit using an orthogonal distance regression. DMA-train growth rates are typically divided into two size intervals which also applies to this ambient data set. In this example from April 16, 2017, an initial growth rate of 18.2 nm/h in the lower size interval (1.8 – 3.2 nm) is calculated. The growth rate in the higher size interval (3.2 – 10 nm) is 5.5 nm/h. Note the linear scale on the y-axis.

April 16

On April 16, 2017, a growing nucleation mode was detected in the DMA-train during morning hours and is presented in Figure 4.4. The mode diameter is shown as white markers. The times of the mode maxima were determined from the time series of each size channel (see Figure 4.10 in SI for more details). Note that in Figure 4.4, unconventionally, the y-axis is linear and not logarithmic. Clearly, the initial particle growth below 3.2 nm is faster compared to the larger size intervals. For the smallest particles the growth rate is 18.2 nm/h, which is then reduced to 5.5 nm/h. The meteorological data indicate a wind direction change during the event from northeast to southeast (see Table 1). A new air mass being carried to the measurement station might lead to dilution of the condensable vapours participating in the sub-10 nm growth. From Figure 4.4 it is seen that during this NPF event case the growth of freshly formed particles stops below 10 nm. Kalivitis et al. (2008) found a depletion of young Aitken mode particles and a low overall number of event cases during an NPF study in Finokalia, Crete. The authors conclude that either the production of particles by NPF is insignificant or that particles are scavenged before reaching their observational size limit of 18 nm. From the results of our study, we conclude that a significant number of sub-10 nm particles can be formed by NPF but may not be discovered at larger sizes for various reasons.

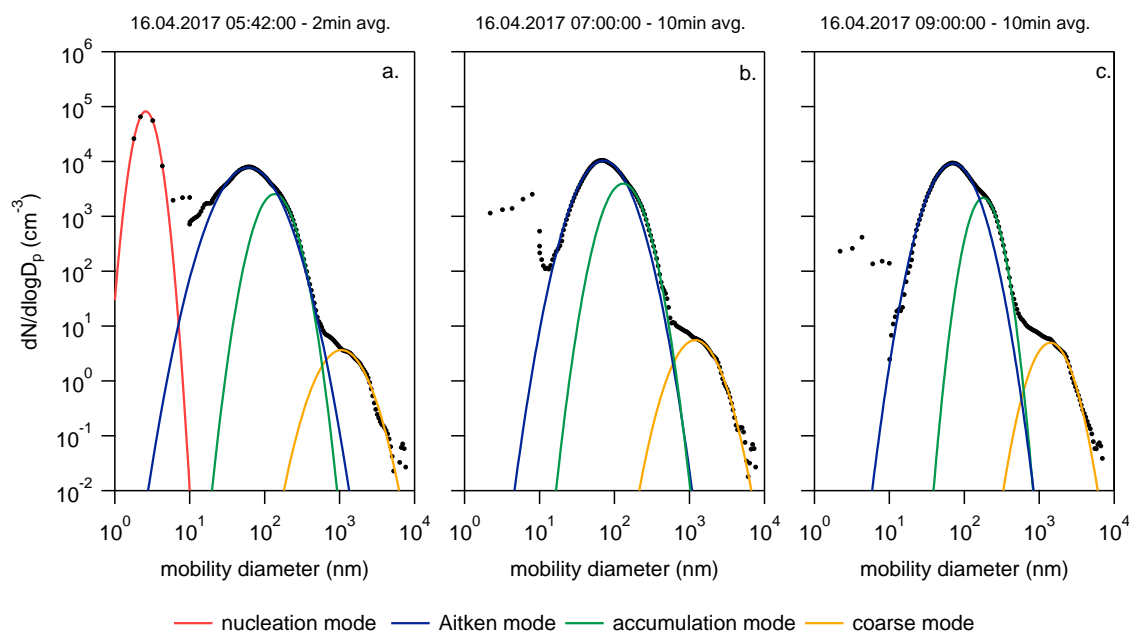


Figure 4.5. Averaged full number size distribution DMA-train data resolving particle diameters < 10 nm, MPSS data (>10 nm) and APS data (>800 nm). Nucleation mode, Aitken mode, accumulation mode and coarse mode were fitted using a log-normal function. Panel a. shows the size distribution during the NPF event on April 16, 2017, with a clear nucleation mode appearing which is reduced at 07:00, as shown in panel b. In panel c., the size distribution after the NPF is demonstrated. Uncertainties on the number concentration are estimated to 20 % for diameters < 10 nm, 30 % between 10 and 20 nm and 10 % for diameters beyond 20 nm.

Thus, the observational size limit for NPF should be lowered to the lowest detectable sizes that can be detected with state-of-the-art instrumentation, i.e. 1 – 2 nm. We suggest that NPF frequency and the production of new particles is underestimated when the nucleation mode size range is not completely covered. The full atmospheric size distribution at the time of the appearance of the nucleation mode averaged during a time interval of 2 minutes is shown in panel (a) of Figure 4.5. The different modes are highlighted with a clear nucleation mode (red) exhibiting the highest number concentrations followed by the Aitken mode (blue), accumulation mode (green) and coarse mode (yellow). Panel (b) of Figure 4.5 shows the nucleation mode has begun fading out, and by panel (c) has completely disappeared, while the Aitken, accumulation and coarse modes remain. This case study demonstrates that the gap in the size distribution of neutral atmospheric nucleation mode particles is well captured by the DMA-train which is oftentimes not the case when conventional instrumentation is deployed. The transition from nucleation to Aitken mode is not fully resolved here (see Figure 4.5). However, the need to combine instrumentation capable of resolving the complete size range becomes evident such that nucleation and Aitken modes are both well-covered.

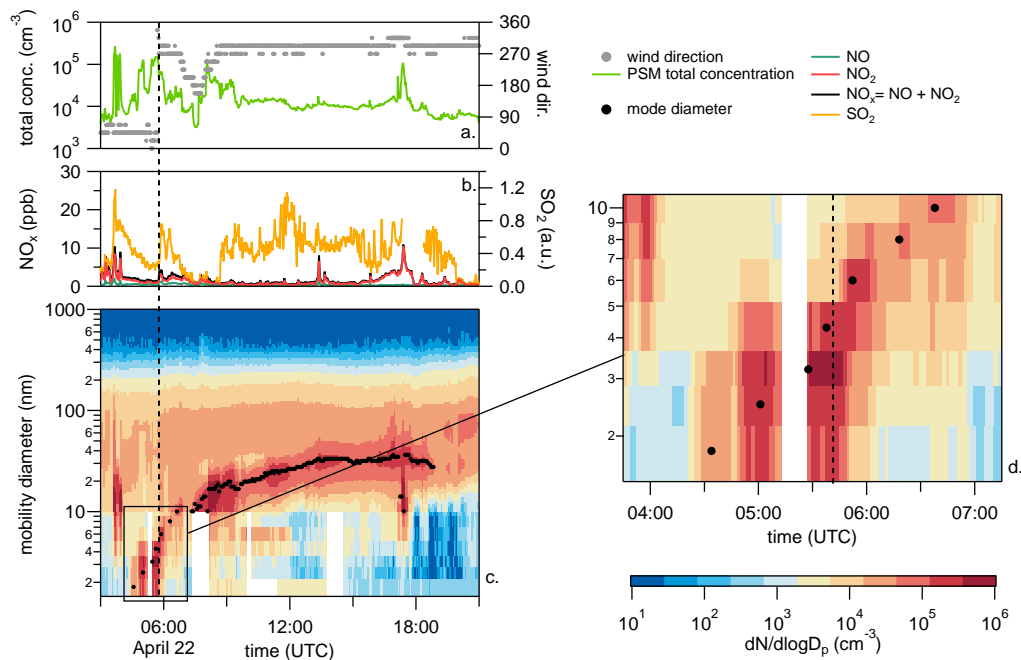


Figure 4.6. NPF event on April 22, 2017. Panel a. shows the 1-min averaged time series of the total particle concentration measured by the PSM on a logarithmic scale and the wind direction (grey markers). Trace gases (NO, NO₂, NO_x=NO+NO₂) are shown in panel b. in blue, red and black. The qualitative SO₂ data was added in orange. In panel c., the size distribution from DMA-train and MPSS data during the complete NPF event is shown. Panel d. depicts the close-up of the start of the NPF event that exhibits bursts of particles in two stages before continuous particle growth takes off. The mode diameter is shown as black markers and the black dashed line indicates the change in wind direction (grey markers in upper panel).

April 22

An NPF event that is characterized by particle growth throughout a whole day is presented in Figure 4.6. Wind direction (grey markers) and total particle concentration (light green), shown in panel (a), correlate well with the trace gas concentrations shown in panel (b). The low NO and NO₂ concentrations (dark green and red traces, respectively) at the start time of the event indicate that the large increase in the number concentration of particles at sizes between 1 – 4 nm is free of plume impact from local sources. Panel (c) shows the time series of the size distribution where the black markers indicate the mode peak diameter. A change in wind direction during the early particle growth from northeast to northwest is marked by the black dashed line. Despite the wind direction change, the mode continues to grow with a slight interruption due to a wind fluctuation at around 08:00. With wind coming from the northwest, i.e. from the Paphos city center and the sea, elevated concentrations of SO₂ are carried to the measurement station, indicating that ship emissions may be a possible source. Panel (d) shows a close-up of the start of the event in the sub-10 nm size

range. It should be noted that a burst-like behaviour is observed in the lowest size channels with an increasing mode diameter in two stages. A new nucleation mode appears for a time length of 10 minutes, disappears and returns for another 15 minutes having a larger mode diameter. The simultaneous increase of the channels during each burst makes the time-offset between the single channels indiscernible. Therefore, we did not determine a growth rate for the time window of the burst-like behaviour. A dynamic process is observed during the early particle growth which, in this case, cannot be explained by peaks in trace gas concentrations or meteorological parameters (clear sky conditions, no change in air mass). However, inhomogeneous mixing of the atmospheric sample volume can disturb the picture during ambient measurements. The growth rate of the higher size interval is 5.8 nm/h and is similar to the growth rate on April 16 and 20 (5.5 and 5.7 nm/h, listed in Table 4.1). On April 22, particles continue growing to sizes where they can potentially act as CCN, which was shown in the A-LIFE study on CCN by Gong et al. (2019).

Nucleation mode particles from airport emission plumes

A significant source contributing to high nanoparticle concentrations was found to be emissions from the nearby airport. Here, all events occurring during evening hours that were correlated with high NO and NO₂ concentrations were averaged over the length of each single emission plume. In total, 17 emission plumes were observed during the A-LIFE measurement period. Two of these plume events, occurring on April 15 and 16 during wind from northeast, are shown in Figure 4.7. Clearly, a substantial fraction of the particle size distribution is distributed in the sub-10 nm size region. The mode diameter of the airport emission plumes was inferred by averaging all 17 airport emission events, for which the size distributions are shown in Figure 4.8 as grey markers. In addition, the events on April 15 and 16 (time series in Figure 4.7) are depicted in red and blue in Figure 4.8. The total particle concentration measured by the PSM (light green line in the upper panel of Figure 4.7) exceeds $1 \times 10^5 \text{ cm}^{-3}$ during plume-impacted time intervals. All airport emission events are accompanied by elevated NO and NO₂ concentrations originating from take-off and taxiway plumes as was e.g. demonstrated by Herndon et al. (2004). The mode diameter of the averaged size distribution of all events (black markers) is at 12.6 nm. Zhu et al. (2011) performed particle size distribution measurements at similar distances to the emission source at the Los Angeles International Airport and found the particle mode diameter at 12 nm which agrees well with our observation.

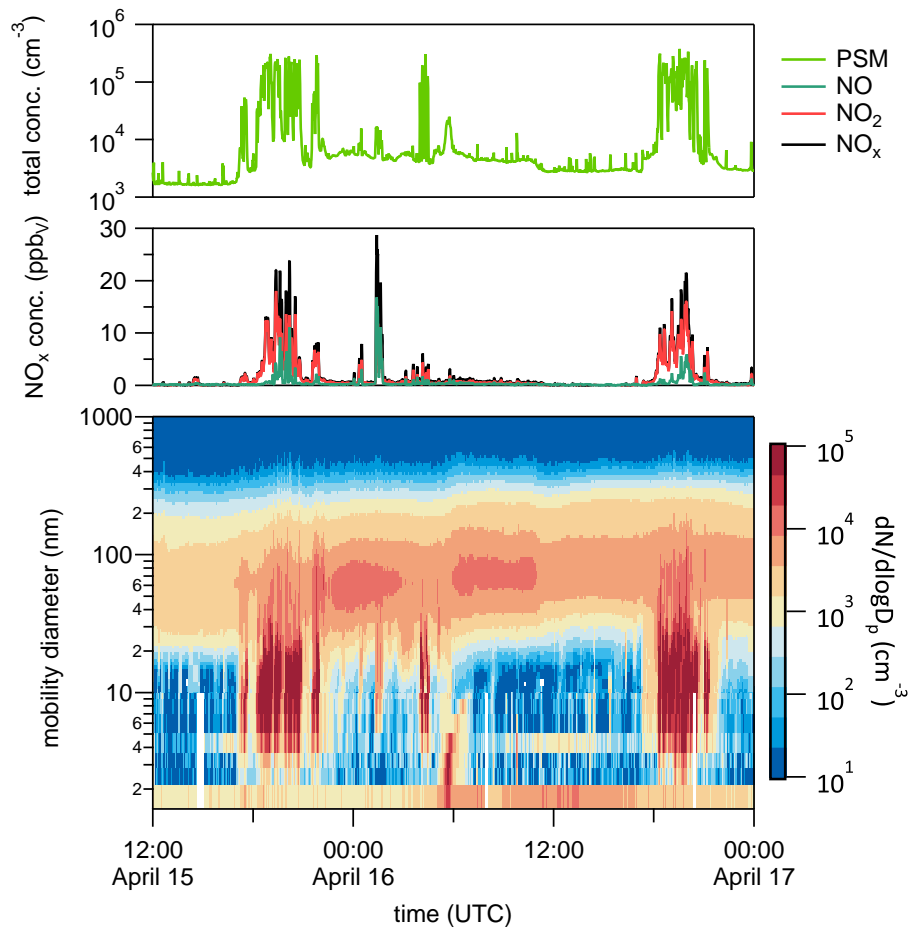


Figure 4.7. Time series of the particle size distribution from 1 – 1000 nm (lower panel) during airport emission plumes. The upper panel shows the 1-min averaged time series of the total particle concentration measured by the Airmodus A10 Particle Size Magnifier (PSM) on a logarithmic scale. Trace gases (NO, NO₂, NO_x = NO + NO₂) are shown in the middle panel. Airport emissions can clearly be assigned to the plumes of nucleation mode particles being carried to the station during N-NW wind situations (wind not shown here). The particle plumes with maximum particle concentrations of $3 \times 10^{-5} \text{ cm}^{-3}$ (upper panel) are accompanied by elevated NO/NO₂ levels (middle panel). On April 16, a new mode appears in the sub-10 nm size range showing well the different behaviour between emission plumes and NPF.

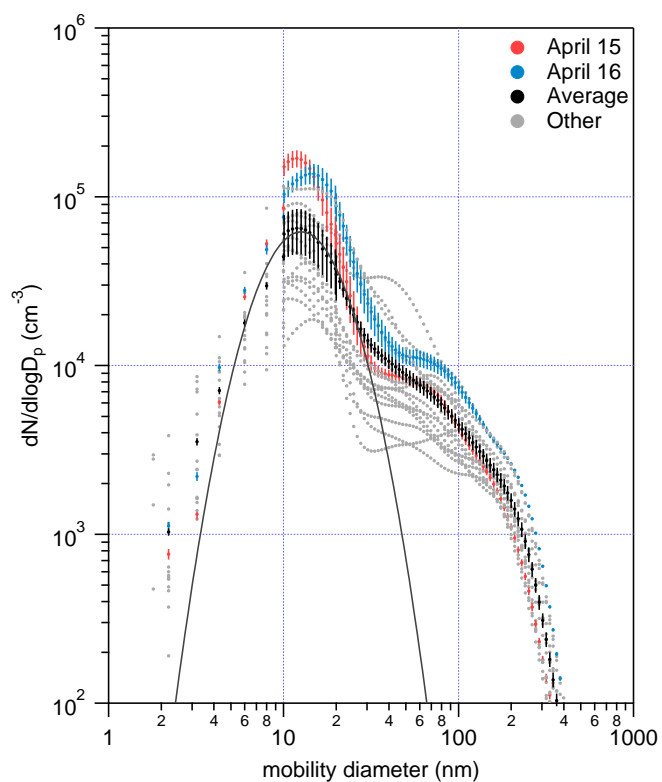


Figure 4.8. Number size distributions during high airport emission loads. The 2h averaged size distributions of the time series presented in Figure 7 shows particle plumes on April 15 (red) and April 16 (blue) yielding high particle number concentrations and elevated NO/NO_2 concentrations. Other airport emission plumes during the measurement period are shown in grey. All number size distributions were averaged (black). The distribution was fitted using a log-normal function (dark grey line) and the resulting mode diameter is at 12.6 nm.

4.4 Conclusion

Atmospheric nanoparticle measurements using the newly developed DMA-train with six fixed size channels in the sub 10 nm size range were conducted for the first time during the intensive A-LIFE measurement campaign in April 2017 with the focus on NPF and early particle growth. The complete atmospheric size distribution between 1.8 nm – 10 μ m was covered by combined measurements of the DMA-train, the MPSS and APS. The nucleation mode, which typically has the highest number concentrations but is not commonly covered by conventional instrumentation, is added to the number size distribution.

Nucleation mode particles were found to originate from NPF and local pollution. With the nearby airport being the largest local pollution source, we analysed the size distribution of airport emission plumes and found a mean mode diameter at 12.6 nm agreeing with similar studies (Zhu et al., 2011).

Strong particle dynamics at relatively short time scales are revealed in the sub-10 nm size range and three early growth events were characterized using the DMA-train data. Early growth rates were determined and a non-linearity of the particle growth in the sub-10 nm size range was found. During 27 total measurement days, 5 and 7 NPF events were observed by the DMA-train and the MPSS, respectively, which contribute to the CCN budget (Gong et al., 2019).

While NPF is not necessarily detected in both systems if particle growth did not exceed the 10 nm threshold, the DMA train revealed firm insight to sub-10 nm particle evolution. The clear appearance of a new mode followed by growth of the particles below 10 nm was found to be interrupted abruptly by changes in the meteorological conditions. Hence, nanoparticle formation may remain undiscovered if using instrumentation with a lower detection limit of 10 nm. Our data suggest that NPF occurs more frequently than is assumed when particle size distribution measurements do not cover the 1 – 10 nm size range. Extended measurements are needed at high time resolution to fully resolve the particle dynamics in the lower nanometre size range in different environments.

4.5 Supplemental Information

Table 4.2. Overview of the CPC settings used during the A-LIFE measurement campaign. Temperature settings were modified from the standard instrument settings for DMA-train channels 0, 2 and 3 to enhance the detection efficiency at the classified mobility diameter, $D_{p,mob}$.

Channel	$D_{p,mob}$ (nm)	Counter	Working fluid	Settings
0	2.2 or 2.5	TSI 3777	DEG	$T_{sat} = 57^{\circ}\text{C}$, $T_{con} = 2^{\circ}\text{C}$
1	1.8	PSM	DEG	$T_{sat} = 81^{\circ}\text{C}$, $T_{gr} = 1^{\circ}\text{C}$, $Q_{sat} = 1 \text{ L min}^{-1}$
2	3.2	TSI 3776	n-butanol	$T_{sat} = 30.1^{\circ}\text{C}$, $T_{con} = 0.1^{\circ}\text{C}$
3	4.3	TSI 3776	n-butanol	$T_{sat} = 30.1^{\circ}\text{C}$, $T_{con} = 0.1^{\circ}\text{C}$
4	6	TSI 3788	water	$T_{sat} = 75^{\circ}\text{C}$, $T_{con} = 15^{\circ}\text{C}$ (standard)
5	8 and 10	TSI 3776	n-butanol	$T_{sat} = 39^{\circ}\text{C}$, $T_{con} = 10^{\circ}\text{C}$

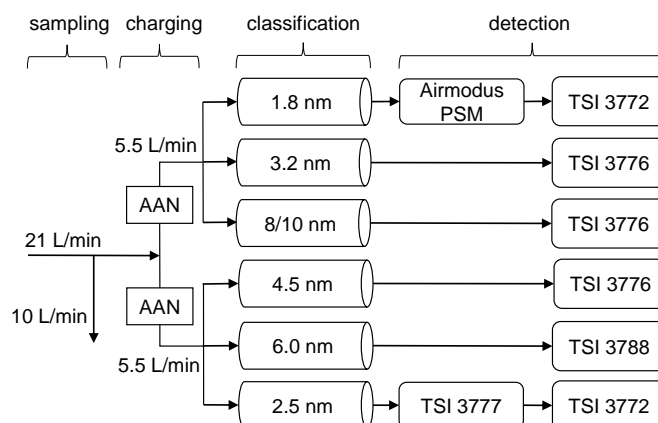


Figure 4.9. Setup of the DMA-train with six DMAs in parallel operated at fixed voltages followed by CPCs tuned for the detection of the classified particle diameter. The instrumentation is operated in two layers with two CPCs at 1.5 L/min inlet flow rate and one at 2.5 L/min inlet flow rate each. The set mobility diameter of each size channel is given in the section “classification” in nm. The largest size channel can be operated in alternating mode, i.e. the set mobility diameter alternates between 8 and 10 nm every 10 seconds.

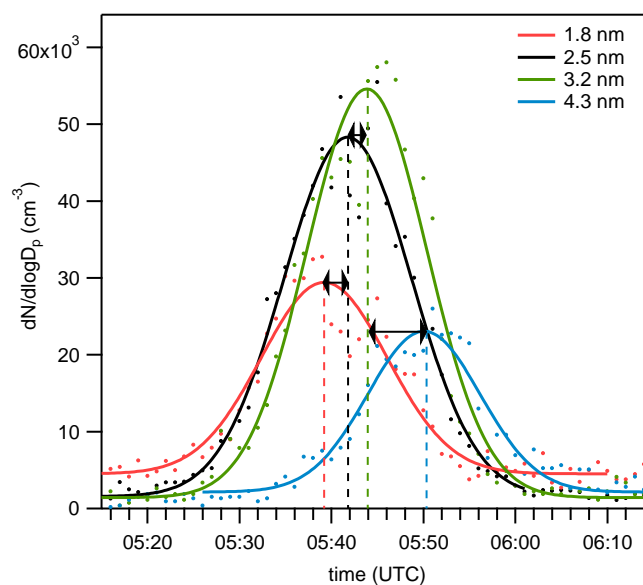


Figure 4.10. Exemplary demonstration of the DMA-train growth rate analysis from the event on April 16, 2017. The coloured markers show the averaged and inverted DMA-train data in channels 1 – 4. A Gaussian fit is applied to the data of each size channel and the position of the peak gives the time of the mode peak. The sequential appearance of the maximum in each size channel starting from the lowest is illustrated by the black arrows.

4.6 Author Contributions

B.W. coordinated the A-LIFE field experiment. S.B., N.F., T.M., K.K., and X.G. performed the measurements. S.B., T.M., K.K. and X.G. analysed the data. S.B. wrote the manuscript. S.B., N.F., T.M., K.K., X.G., J.P., B.W. and P.M.W. commented on the manuscript.

4.6.1 Personal contributions

The measurements of this study took place in Cyprus and I planned the experimental setup of the DMA-train at the measurement site in cooperation with the TROPOS institute. The DMA-train and the PSM were set up by myself and I performed the DMA-train and PSM measurement throughout the A-LIFE campaign. The data analysis of the DMA-train and PSM nanoparticle measurements was performed by me. I took actively part in the scientific discussion of the data during two data workshops where I presented the results of the nanoparticle measurements to the A-LIFE collaboration. I received processed trace gas data and MPSS data from my co-authors and included this into my analysis. I wrote the manuscript.

4.7 References

- S. Amanatidis, W. Kong, H. Mai, Y. Huang, and R. Flagan. The Caltech nano-Scanning Electrical Mobility Spectrometer (nSEMS): Design, Modeling, and Characterization for Size Distribution Measurements in the Low Nanometer Regime. In *Poster presentation at The American Aerosol Research Association 37th Annual Conference, Portland, Oregon, USA*, 2019. URL <https://caltech.app.box.com/s/68juvn6h6jjnud96gmbrq3kpxeufcfgj>.
- K. Barmounis, A. Ranjithkumar, A. Schmidt-Ott, M. Attoui, and G. Biskos. Enhancing the detection efficiency of condensation particle counters for sub-2 nm particles. *Journal of Aerosol Science*, 117:44–53, 2018. ISSN 0021-8502. doi:10.1016/j.jaerosci.2017.12.005.
- F. Bianchi, J. Tröstl, H. Junninen, C. Frege, S. Henne, C. R. Hoyle, U. Molteni, E. Herrmann, A. Adamov, N. Bukowiecki, X. Chen, J. Duplissy, M. Gysel, M. Hutterli, J. Kangasluoma, J. Kontkanen, A. Kürten, H. E. Manninen, S. Münch, O. Peräkylä, T. Petäjä, L. Rondo, C. Williamson, E. Weingartner, J. Curtius, D. R. Worsnop, M. Kulmala, J. Dommen, and U. Baltensperger. New particle formation in the free troposphere: A question of chemistry and timing. *Science*, 352(6289):1109–1112, 2016. ISSN 10959203. doi:10.1126/science.aad5456.
- M. Dal Maso, M. Kulmala, I. Riipinen, R. Wagner, T. Hussein, P. P. Aalto, and K. E. Lehtinen. Formation and growth of fresh atmospheric aerosols: Eight years of aerosol size distribution data from SMEAR II, Hyytiälä, Finland. *Boreal Environment Research*, 10(5):323–336, 2005. ISSN 12396095. URL <http://citeseerx.ist.psu.edu/viewdoc/download?doi=10.1.1.562.3319&rep=rep1&type=pdf>.
- C. Debevec, S. Sauvage, V. Gros, K. Sellegri, J. Sciare, M. Pikridas, I. Stavroulas, T. Leonardis, V. Gaudion, L. Depelchin, I. Fronval, R. Sarda-Esteve, D. Baisnée, B. Bonsang, C. Savvides, M. Vrekoussis, and N. Locoge. Driving parameters of biogenic volatile organic compounds and consequences on new particle formation observed at an eastern Mediterranean background site. *Atmospheric Chemistry and Physics*, 18(19):14297–14325, 2018. ISSN 16807324. doi:10.5194/acp-18-14297-2018.
- X. Gong, H. Wex, T. Müller, A. Wiedensohler, K. Höhler, K. Kandler, N. Ma, B. Dietel, T. Schiebel, O. Möhler, and F. Stratmann. Characterization of aerosol properties at Cyprus, focusing on cloud condensation nuclei and ice nucleating particles. *Atmospheric Chemistry and Physics*, pages 1–34, 2019. doi:10.5194/acp-19-10883-2019.
- A. Hamed, J. Joutsensaari, S. Mikkonen, L. Sogacheva, M. Dal Maso, M. Kulmala, F. Cavalli, S. Fuzzi, M. C. Facchini, S. Decesari, M. Mircea, K. E. Lehtinen, and A. Laaksonen. Nucleation and growth of new particles in Po Valley, Italy. *Atmospheric Chemistry and Physics*, 7(2):355–376, 2007. ISSN 16807324. doi:10.5194/acp-7-355-2007.

- S. C. Herndon, J. H. Shorter, M. S. Zahniser, D. D. Nelson, J. Jayne, R. C. Brown, R. C. Miake-Lye, I. Waitz, P. Silva, T. Lanni, K. Demerjian, and C. E. Kolb. NO and NO₂ emission ratios measured from in-use commercial aircraft during taxi and takeoff. *Environmental Science and Technology*, 38(22):6078–6084, 2004. ISSN 0013936X. doi:10.1021/es049701c.
- T. Hoffmann, C. D. O’Dowd, and J. H. Seinfeld. Iodine oxide homogeneous nucleation: An explanation for coastal new particle production. *Geophysical Research Letters*, 28(10):1949–1952, 2001. doi:10.1029/2000GL012399.
- J. Jiang, J. Zhao, M. Chen, F. L. Eisele, J. Scheckman, B. J. Williams, C. Kuang, and P. H. McMurry. First measurements of neutral atmospheric cluster and 1-2 nm particle number size distributions during nucleation events. *Aerosol Science and Technology*, 45(4):ii–v, 2011. ISSN 02786826. doi:10.1080/02786826.2010.546817.
- N. Kalivitis, W. Birmili, M. Stock, B. Wehner, A. Massling, A. Wiedensohler, E. Gerasopoulos, and N. Mihalopoulos. Particle size distributions in the Eastern Mediterranean troposphere. *Atmospheric Chemistry and Physics*, 8(22):6729–6738, 2008. ISSN 16807324. doi:10.5194/acp-8-6729-2008.
- J. Kangasluoma and J. Kontkanen. On the sources of uncertainty in the sub-3 nm particle concentration measurement. *Journal of Aerosol Science*, 112:34–51, 2017. ISSN 18791964. doi:10.1016/j.jaerosci.2017.07.002.
- J. Kangasluoma, H. Junninen, K. Lehtipalo, J. Mikkilä, J. Vanhanen, M. Attoui, M. Sipilä, D. R. Worsnop, M. Kulmala, and T. Petäjä. Remarks on ion generation for CPC detection efficiency studies in sub-3-nm size range. *Aerosol Science and Technology*, 47(5):556–563, 2013. ISSN 1521-7388. doi:10.1080/02786826.2013.773393.
- S. Kecorius, T. Vogl, P. Paasonen, J. Lampilahti, D. Rothenberg, H. Wex, S. Zeppenfeld, M. van Pinxteren, M. Hartmann, S. Henning, X. Gong, A. Welti, M. Kulmala, F. Stratmann, H. Herrmann, and A. Wiedensohler. New particle formation and its effect on CCN abundance in the summer Arctic: a case study during PS106 cruise. *Atmospheric Chemistry and Physics*, 19:14339–14364, 2019. doi:10.5194/acp-19-14339-2019.
- K. E. Lehtinen and M. Kulmala. A model for particle formation and growth in the atmosphere with molecular resolution in size. *Atmospheric Chemistry and Physics*, 3(1):251–257, 2003. ISSN 16807324. doi:10.5194/acp-3-251-2003.
- K. E. Lehtinen, H. Korhonen, M. Dal Maso, and M. Kulmala. On the concept of condensation sink diameter. *Boreal Environment Research*, 8(4):405–411, 2003. ISSN 12396095.

- J. Mäkelä, P. Aalto, V. Jokinen, T. Pohja, A. Nissinen, S. Palmroth, T. Markkanen, K. Seitsonen, H. Lihavainen, and M. Kulmala. Observations of ultrafine aerosol particle formation and growth in boreal forest. *Geophysical Research Letters*, 24(10):1219–1222, 1997. doi:10.1029/97GL00920.
- H. E. Manninen, T. Petäjä, E. Asmi, N. Riipinen, T. Nieminen, J. Mikkilä, U. Hörrak, A. Mirme, S. Mirme, L. Laakso, V. M. Kerminen, and M. Kulmala. Long-term field measurements of charged and neutral clusters using Neutral cluster and Air Ion Spectrometer (NAIS). *Boreal Environment Research*, 14(4):591–605, 2009. ISSN 12396095. URL <http://www.borenv.net/BER/pdfs/ber14/ber14-591.pdf>.
- H. E. Manninen, T. Nieminen, E. Asmi, S. Gagné, S. Häkkinen, K. Lehtipalo, P. Aalto, M. Vana, A. Mirme, S. Mirme, U. Hörrak, C. Plass-Dülmer, G. Stange, G. Kiss, A. Hoffer, N. Töro, M. Moerman, B. Henzing, G. De Leeuw, M. Brinkenberg, G. N. Kouvarakis, A. Bougiatioti, N. Mihalopoulos, C. O’Dowd, D. Ceburnis, A. Arneth, B. Svenningsson, E. Swietlicki, L. Tarozzi, S. Decesari, M. C. Facchini, W. Birmili, A. Sonntag, A. Wiedensohler, J. Boulon, K. Sellegri, P. Laj, M. Gysel, N. Bukowiecki, E. Weingartner, G. Wehrle, A. Laaksonen, A. Hamed, J. Joutsensaari, T. Petäjä, V. M. Kerminen, and M. Kulmala. EUCAARI ion spectrometer measurements at 12 European sites-analysis of new particle formation events. *Atmospheric Chemistry and Physics*, 10(16):7907–7927, 2010. ISSN 16807316. doi:10.5194/acp-10-7907-2010.
- S. B. Mazon, I. Riipinen, D. M. Schultz, M. Valtanen, M. D. Maso, L. Sogacheva, and H. Junninen. Classifying previously undefined days from eleven years of aerosol-particle-size distribution data from the SMEAR II station, Hyytiälä, Finland. *Atmospheric Chemistry and Physics*, 9:667–676, 2009. doi:10.5194/acp-9-667-2009.
- J. Merikanto, D. V. Spracklen, G. W. Mann, S. J. Pickering, and K. S. Carslaw. Impact of nucleation on global CCN. *Atmos. Chem. Phys.*, 9:8601–8616, 2009. doi:10.5194/acp-9-8601-2009.
- J. E. Petit, O. Favez, A. Albinet, and F. Canonaco. A user-friendly tool for comprehensive evaluation of the geographical origins of atmospheric pollution: Wind and trajectory analyses. *Environmental Modelling and Software*, 88:183–187, 2017. ISSN 13648152. doi:10.1016/j.envsoft.2016.11.022.
- M. Pikridas, I. Riipinen, L. Hildebrandt, E. Kostenidou, H. Manninen, N. Mihalopoulos, N. Kalivitis, J. F. Burkhardt, A. Stohl, M. Kulmala, and S. N. Pandis. New particle formation at a remote site in the eastern Mediterranean. *Journal of Geophysical Research Atmospheres*, 117(12):1–14, 2012. ISSN 01480227. doi:10.1029/2012JD017570.
- D. V. Spracklen, K. S. Carslaw, M. Kulmala, V. M. Kerminen, G. W. Mann, and S. L. Sihto. The contribution of boundary layer nucleation events to total particle concentrations on

- regional and global scales. *Atmospheric Chemistry and Physics*, 6(12):5631–5648, 2006. ISSN 16807324. doi:10.5194/acp-6-5631-2006.
- D. Stolzenburg, G. Steiner, and P. M. Winkler. A DMA-Train for precision measurement of sub-10nm aerosol dynamics. *Atmospheric Measurement Techniques*, 10:1639–1651, 2017. ISSN 18678548. doi:10.5194/amt-10-1639-2017.
- D. Stolzenburg, L. Fischer, A. L. Vogel, M. Heinritzi, M. Schervish, M. Simon, A. C. Wagner, L. Dada, L. R. Ahonen, A. Amorim, A. Baccarini, P. S. Bauer, B. Baumgartner, A. Bergen, F. Bianchi, M. Breitenlechner, S. Brilke, S. B. Mazon, D. Chen, A. Dias, D. C. Draper, J. Duplissy, I. E. Haddad, H. Finkenzeller, C. Frege, C. Fuchs, O. Garmash, H. Gordon, X. He, J. Helm, V. Hofbauer, C. R. Hoyle, C. Kim, J. Kirkby, J. Kontkanen, A. Kürten, J. Lampilahti, M. Lawler, K. Lehtipalo, M. Leiminger, H. Mai, S. Mathot, B. Mentler, U. Molteni, W. Nie, T. Nieminen, J. B. Nowak, A. Ojdanic, A. Onnela, M. Passananti, T. Petäjä, L. L. Quéléver, M. P. Rissanen, N. Sarnela, S. Schallhart, C. Tauber, A. Tomé, R. Wagner, M. Wang, L. Weitz, D. Wimmer, M. Xiao, C. Yan, P. Ye, Q. Zha, U. Baltensperger, J. Curtius, J. Dommen, R. C. Flagan, M. Kulmala, J. N. Smith, D. R. Worsnop, A. Hansel, N. M. Donahue, and P. M. Winkler. Rapid growth of organic aerosol nanoparticles over a wide tropospheric temperature range. *Proceedings of the National Academy of Sciences of the United States of America*, 115(37):9122–9127, 2018. ISSN 10916490. doi:10.1073/pnas.1807604115.
- M. R. Stolzenburg and P. H. McMurry. Equations governing single and tandem DMA configurations and a new lognormal approximation to the transfer function. *Aerosol Science and Technology*, 42(6):421–432, 2008. ISSN 02786826. doi:10.1080/02786820802157823.
- M. R. Stolzenburg, P. H. McMurry, H. Sakurai, J. N. Smith, R. L. Mauldin, F. L. Eisele, and C. F. Clement. Growth rates of freshly nucleated atmospheric particles in Atlanta. *Journal of Geophysical Research Atmospheres*, 110(22):1–10, 2005. ISSN 01480227. doi:10.1029/2005JD005935.
- C. Tauber, S. Brilke, P. J. Wlasits, P. S. Bauer, G. Köberl, G. Steiner, and P. M. Winkler. Humidity effects on the detection of soluble and insoluble nanoparticles in butanol operated condensation particle counters. *Atmospheric Measurement Techniques*, 12:3659–3671, 2019. doi:10.5194/amt-12-3659-2019.
- R. J. Weber, P. H. McMurry, F. L. Eisele, and D. J. Tanner. Measurement of expected nucleation precursor species and 3-500 nm diameter particles at Mauna Loa Observatory, Hawaii. 52(12):2242–2257, 1995. ISSN 00224928. doi:10.1175/1520-0469(1995)052<2242:MOENPS>2.0.CO;2.

-
- R. J. Weber, J. Marti, P. H. McMurry, F. L. Eisele, D. J. Tanner, and A. Jefferson. Measurements of new particle formation and ultrafine particle growth rates at a clean continental site. *Journal of Geophysical Research*, 102:4375–4385, 1997. doi:10.1029/96JD03656.
- A. Wiedensohler. An approximation of the bipolar charge distribution for particles in the submicron size range. *Journal of Aerosol Science*, 19(3):387–389, 1988. ISSN 00218502. doi:10.1016/0021-8502(88)90278-9.
- A. Wiedensohler, A. Wiesner, K. Weinhold, W. Birmili, M. Hermann, M. Merkel, T. Müller, S. Pfeifer, A. Schmidt, T. Tuch, F. Velarde, P. Quincey, S. Seeger, and A. Nowak. Mobility particle size spectrometers: Calibration procedures and measurement uncertainties. *Aerosol Science and Technology*, 52(2):146–164, 2018. ISSN 15217388. doi:10.1080/02786826.2017.1387229.
- C. J. Williamson, A. Kupc, D. Axisa, K. R. Bilsback, T. Bui, P. Campuzano-jost, M. Dollner, K. D. Froyd, A. L. Hodshire, J. L. Jimenez, J. K. Kodros, G. Luo, D. M. Murphy, B. A. Nault, E. A. Ray, B. Weinzierl, J. C. Wilson, F. Yu, P. Yu, J. R. Pierce, and C. A. Brock. A large source of cloud condensation nuclei from new particle formation in the tropics. *Nature*, 574:399–403, 2019. ISSN 1476-4687. doi:10.1038/s41586-019-1638-9.
- L. Yao, O. Garmash, F. Bianchi, J. Zheng, C. Yan, J. Kontkanen, H. Junninen, S. B. Mazon, M. Ehn, P. Paasonen, M. Sipilä, M. Wang, X. Wang, S. Xiao, H. Chen, Y. Lu, B. Zhang, D. Wang, Q. Fu, F. Geng, L. Li, H. Wang, L. Qiao, X. Yang, J. Chen, V. M. Kerminen, T. Petäjä, D. R. Worsnop, M. Kulmala, and L. Wang. Atmospheric new particle formation from sulfuric acid and amines in a Chinese megacity. *Science*, 361(6399):278–281, 2018. ISSN 10959203. doi:10.1126/science.aao4839.
- H. Yu, L. Zhou, L. Dai, W. Shen, W. Dai, J. Zheng, Y. Ma, and M. Chen. Nucleation and growth of sub-3 nm particles in the polluted urban atmosphere of a megacity in China. *Atmospheric Chemistry and Physics*, 16(4):2641–2657, 2016. ISSN 16807324. doi:10.5194/acp-16-2641-2016.
- Y. Zhu, E. Fanning, R. C. Yu, Q. Zhang, and J. R. Froines. Aircraft emissions and local air quality impacts from takeoff activities at a large International Airport. *Atmospheric Environment*, 45(36):6526–6533, 2011. ISSN 13522310. doi:10.1016/j.atmosenv.2011.08.062.

Chapter 5

Conclusion

Secondary aerosol formation from gas-to-particle conversion is a global phenomenon and largely contributes to the aerosol and CCN budget of the atmosphere (Kulmala et al., 2004; Spracklen et al., 2006, 2008). A detailed understanding of the atmospheric processes of particle formation and growth are required to estimate the environmental and health-related consequences. The scientific investigation of aerosol nanoparticles requires state-of-the-art instrumentation. The measurement of nanoparticles in the sub-10 nm size regime is especially challenging as was discussed in Chapter 1. The charging probability is low, diffusional losses in the instruments and lines are high, and the detection efficiency in CPCs is reduced.

In Chapter 2, a new method for the precision characterization CPCs having a lower detection limit in the 1 - 4 nm size range was presented. A newly developed bipolar electrospray source introduced by Fernández de la Mora and Barrios-Collado (2017) in combination with the Vienna-type high-resolution UDMA-4 was demonstrated to be well-suited for the generation of mobility standards between 1 - 4 nm approximated mobility equivalent diameter. Previous studies have used mobility standards but have been limited to 2 - 3 mobility resolved clusters (Attoui et al., 2013; Jiang et al., 2011). The range of available clusters of well-known composition and mobility has been extended and up to 18 peaks were clearly resolved (see Figure 2.2). The advancement of this study is the first mass spectrometric characterization of clusters produced by the bipolar electrospray. High chemical purity of the clusters could be confirmed, which is required to use these as mobility standards (see Figures 2.3 and 2.4). The experimental challenge of the operation of the bipolar electrospray was to produce cluster ions of charge state 1 which is a critical prerequisite when measuring the CPC detection efficiency. The combination of ionAPI-TOF and particle counter measurements enabled the confirmation of the dominant production of singly charged cluster ions.

Studying the activation behavior of particles generated in the laboratory and claiming to perform precision measurements undoubtedly requires exact knowledge of the sample composition. Resuming the experiment presented in Chapter 2, composition measurements of the silver particles produced by the tube furnace would be of general interest also with regard to the experiment presented in Chapter 3. A size-resolved measurement would add information on the characteristics of the classified silver clusters. Preferably, the measurements are conducted using pure nitrogen as carrier gas with a comparison to synthetic air conditions to learn about the oxidation states of the produced silver particles. As discussed in Chapter 2, a general limitation during mass mobility measurements is the transmission of ion clusters

through the DMA. This may become an issue when characterizing particles from the tube furnace, which likely are available at considerably lower number concentration. One possible approach here is the implementation of a parallel-plate high-resolution DMA with a planar geometry having a higher transmission efficiency than the cylindrical Vienna-type UDMA-4. It is also worth mentioning that the experiment presented in Chapter 2 is limited to two types of cluster ions, THABr and TBAI. A tendency of improved detection efficiency of TBAI in the DEG-based TSI 3777 is observed as shown in Figure 2.8, which can be explained by a better solubility of TBAI in the working fluid DEG. Extending the range of test material and working fluid for the generation of clusters using the bipolar electrospray source to further investigate the activation efficiency of different cluster types with regard to supersaturated vapor could form a future study. With respect to ambient measurements, an interesting sample to generate using the electrospray is ammonium sulfate. Performing activation efficiency measurements using ammonium sulfate clusters that are well characterized in the APi-TOF could further improve the information on the CPC's detection efficiency.

The effect on the CPC lower detection limit using soluble and insoluble seed types exposed to changing RH in the carrier gas and at different nucleation temperatures was investigated in the study presented in Chapter 3. The temperature dependent experiments showed enhanced CPC detection efficiencies at reduced nucleation temperature. Furthermore, the findings highlight the importance of molecular interactions between seed and vapor molecules. Hygroscopic sodium chloride particles activate at smaller seed sizes when the aerosol is exposed to a carrier gas at increased RH. Under atmospheric conditions, the RH may affect a CPC's lower detection limit. Further, it confirms the recommendation that the RH of the sample flow must be monitored and controlled for correct data processing (Wiedensohler et al., 2012). For future studies, this study may be extended to investigate the chemical composition of the generated particles of both polarities as already stated above.

Finally, an atmospheric study using a DMA-train with the focus on NPF and early growth of nanoparticles in the sub-10 nm size range is presented in Chapter 4. Here, the results of the ground based size distribution measurement during the one month intensive A-LIFE measurement campaign are shown. The DMA-train uses the CPCs as particle detectors that were subject of the characterization studies in the previous chapters. The combined size distribution covering the complete atmospheric size range (see Figure 4.5) shows that the atmospheric modes are well captured. However, improvements may be made in the overlap size range from 10 - 20 nm. Such improvement may include the setup of an additional MPSS dedicated to measuring the lower nanometer size range and thereby complementing the MPSS and DMA-train measurement. The DMA-train showed to be well-suited for capturing the early particle growth during NPF events. Atmospheric growth rates were calculated and the possible impact of changing trace gas concentrations and meteorological conditions was

considered during the analysis (see Table 4.1). Interestingly, the growth of newly formed particles did not necessarily exceed the 10 nm threshold and consequently was not detected by the MPSS. This finding indicates that NPF may occur more frequently than is estimated from observations that do not cover the sub-10 nm size range.

The question of the composition of the particles remained unanswered in this study. However, a strong recommendation for future atmospheric DMA-train studies is the parallel cluster composition measurement using mass spectrometers.

One approach to overcome the lack of available mass spectrometric measurements is the indirect composition measurement by the composition dependent activation efficiency in different CPCs as was presented as the nano-CPC battery approach in Kangasluoma et al. (2014). The DMA-train may be well-suited for indirect composition measurement of sub-3 nm particles by tuning the CPCs to detect even smaller sizes than at standard settings (see Chapter 2). In addition to the size distribution measurement at different fixed voltages in the DMAs, the voltage may be held fixed to get information on the CPC dependent activation efficiency. Preparing the DMA-train for the indirect composition measurement does, however, require detailed calibration measurements under laboratory conditions and the parallel measurement of the ion composition using mass spectrometers.

In summary, the results of this thesis have provided a deeper insight into the generation of mobility standards in the low nanometer size range. The mobility standards may be used for characterization purposes of aerosol instrumentation and experimental studies on heterogeneous nucleation. The seed-vapor interaction during heterogeneous nucleation in CPCs has been investigated under changing RH conditions. The results showed to be of general relevance for ambient measurements. The results of the temperature and humidity dependent CPC counting efficiency were directly applied in the analysis of the atmospheric measurements. During the A-LIFE campaign, several NPF events were studied in detail. The importance of covering the sub-10 nm size range to correctly determine the NPF frequency in the atmosphere was highlighted.

Undoubtedly, future developments on aerosol instrumentation and methods to investigate aerosol nanoparticles are still needed. Despite large research efforts, it is necessary to expand the worldwide measurement network and to implement new measurement methods to understand the fundamental processes in the atmosphere.

5.1 References

- M. Attoui, M. Paragano, J. Cuevas, and J. Fernández de la Mora. Tandem DMA Generation of Strictly Monomobile 1 - 3.5 nm Particle Standards. *Aerosol Science and Technology*, 47(5):499–511, 2013. doi:10.1080/02786826.2013.764966.
- J. Fernández de la Mora and C. Barrios-Collado. A bipolar electrospray source of singly charged salt clusters of precisely controlled composition. *Aerosol Science and Technology*, 51(6):778–786, 2017. ISSN 0278-6826. doi:10.1080/02786826.2017.1302070.
- J. Jiang, M. Chen, C. Kuang, M. Attoui, and P. H. McMurry. Electrical Mobility Spectrometer Using a Diethylene Glycol Condensation Particle Counter for Measurement of Aerosol Size Distributions Down to 1 nm. *Journal of Aerosol Science*, 45(4):510–251, 2011. doi:10.1080/02786826.2010.547538.
- J. Kangasluoma, C. Kuang, D. Wimmer, M. P. Rissanen, K. Lehtipalo, M. Ehn, D. R. Worsnop, J. Wang, M. Kulmala, and T. Petäjä. Sub-3 nm particle size and composition dependent response of a nano-CPC battery. *Atmospheric Measurement Techniques*, 7(3):689–700, 2014. ISSN 18678548. doi:10.5194/amt-7-689-2014.
- M. Kulmala, H. Vehkamäki, T. Petäjä, M. Dal Maso, A. Lauri, V. M. Kerminen, W. Birmili, and P. H. McMurry. Formation and growth rates of ultrafine atmospheric particles: A review of observations. *Journal of Aerosol Science*, 35(2):143–176, 2004. ISSN 00218502. doi:10.1016/j.jaerosci.2003.10.003.
- D. V. Spracklen, K. S. Carslaw, M. Kulmala, V. M. Kerminen, G. W. Mann, and S. L. Sihto. The contribution of boundary layer nucleation events to total particle concentrations on regional and global scales. *Atmospheric Chemistry and Physics*, 6(12):5631–5648, 2006. ISSN 16807324. doi:10.5194/acp-6-5631-2006.
- D. V. Spracklen, K. S. Carslaw, M. Kulmala, V. M. Kerminen, S. L. Sihto, I. Riipinen, J. Merikanto, G. W. Mann, M. P. Chipperfield, A. Wiedensohler, W. Birmili, and H. Lihavainen. Contribution of particle formation to global cloud condensation nuclei concentrations. *Geophysical Research Letters*, 35(6):1–5, 2008. ISSN 00948276. doi:10.1029/2007GL033038.
- A. Wiedensohler, W. Birmili, A. Nowak, A. Sonntag, K. Weinhold, M. Merkel, B. Wehner, T. Tuch, S. Pfeifer, M. Fiebig, A. M. Fjåraa, E. Asmi, K. Sellegri, R. Depuy, H. Venzac, P. Villani, P. Laj, P. Aalto, J. A. Ogren, E. Swietlicki, P. Williams, P. Roldin, P. Quincey, C. Hüglin, R. Fierz-Schmidhauser, M. Gysel, E. Weingartner, F. Riccobono, S. Santos, C. Grüning, K. Faloon, D. Beddows, R. Harrison, C. Monahan, S. G. Jennings, C. D. O’Dowd, A. Marinoni, H.-G. Horn, L. Keck, J. Jiang, J. Scheckman, P. H. McMurry, Z. Deng, C. S. Zhao, M. Moerman, B. Henzing, G. de Leeuw, G. Löschau, and S. Bastian.

Mobility particle size spectrometers: harmonization of technical standards and data structure to facilitate high quality long-term observations of atmospheric particle number size distributions. *Atmospheric Measurement Techniques*, 5(3):657–685, 2012. doi:10.5194/amt-5-657-2012.

List of Figures

1.1	The atmospheric number size distribution	10
1.2	Overview of experimental methods	13
1.3	The bipolar electrospray chamber	15
1.4	Technical drawing of the high-resolution UDMA-4	19
2.1	The experimental setup	32
2.2	Positive and negative mobility spectra of THABr and TBAI clusters	36
2.3	Positive and negative mass mobility spectra of THABr and TBAI clusters	38
2.4	Negative mobility-resolved mass spectra	39
2.5	Counting efficiency curve for silver particles	42
2.6	Mobility spectrum and counting efficiency curve for positively charged TBAI	43
2.7	Overview of counting efficiency curves of THABr(+/-) and TBAI(+/-) clusters	44
2.8	Overview of resulting cut-off diameters	46
2.9	Demonstration of the current adjustment of the bipolar electrospray	48
2.10	Positive bulk mass spectra of THABr in unipolar and bipolar electrospray mode	49
3.1	The experimental setup	61
3.2	The onset saturation ratio vs. nucleation temperature for Ag(n)/NaCl(n) seeds	64
3.3	The onset saturation ratio versus nucleation temperature for NaCl seeds in different RH regimes	65
3.4	Normalized mean diameter of NaCl seeds as a function of RH	67
3.5	The detection efficiency vs. mobility diameter for NaCl(n) seeds	69
3.6	The cut-off diameter as a function of RH for NaCl(+/-/n) seeds for three temperature settings	71
3.7	The cut-off diameter as a function of RH for Ag(+/-/n) seeds for three temperature settings	72
4.1	Sampling site location	86
4.2	The DMA-train NPF classification criteria	90
4.3	Sub-10 nm size distribution patterns	91
4.4	NPF event on April 16, 2017	93
4.5	Averaged complete atmospheric number size distribution	94
4.6	NPF event on April 22, 2017	95
4.7	Size distributions with airport emission impact	97
4.8	Number size distributions during high airport emission loads	98
4.9	The experimental setup of the DMA-train	101
4.10	DMA-train growth rate analysis example	101

List of Tables

2.1	Overview of inverse mobilities of positive and negative THABr and TBAI . . .	37
2.2	Overview of cut-off diameters for positive and negative Ag, TBAI and THABr	45
3.1	Temperature settings of the TSI 3776	62
3.2	Overview of the SANC experimental results	66
3.3	The calculated maxima of the CPC saturation ratio profiles at three temperature settings	68
4.1	Overview of the NPF event classification, GRs in three size ranges and prevailing wind direction during A-LIFE	92
4.2	Overview of the CPC settings used during the A-LIFE measurement campaign	100

Acknowledgements

There is a number of people I would like to thank for great support throughout my PhD project and I want to acknowledge the European Research Council for funding my work within the project NANODYNAMITE 616075.

First, I want to thank Prof. Dr. Paul Winkler for supervising my thesis and welcoming me in the Nanodynamite team. The Nanodynamite team made the last years fun times and even managed to make me go down a mountain slope on a snowboard. I would also like to thank the whole Vienna aerosol group. Special thanks to Prof. Dr. Bernadett Weinzierl for making me part of the A-LIFE team and to my colleagues during the A-LIFE campaign.

I would like to especially thank my colleagues Paulus Bauer, Carmen Dameto de España, Nikolaus Fölker, Julian Resch, Sebastian Schmitt, David Schmoll, Christian Tauber, Daniela Wimmer and Peter Wlasits for great support in the lab, during field measurements in Cyprus and Schwechat and good times during conferences in Tours, Zurich, St. Louis and Gothenburg.

I would like to thank Dr. Gerhard Steiner for becoming my thesis mentor and always being available for my science questions.

A special thanks goes to Prof. Dr. Andreas Held and Prof. Dr. Jyrki Mäkelä for reviewing my thesis.

In particular, I would like to thank my family, Stefanie, Clara, Jan, Elisabeth and Kurt Brilke, for being great support, joyful visits at CERN and in Cyprus and always being motivating. Thanks to Peter Engel for teaching me the physics basics with full commitment some years ago.

Finally I would like to thank my partner Jonathan Harsanyi for coming with me to Vienna, constant support, love and companionship.